Assessing multi-year-drought vulnerability in dense Mediterranean-climate forests using water-balance-based indicators

Guotao Cui[a,*], Qin Ma[b], Roger Bales[a,c]

[a] Sierra Nevada Research Institute and School of Engineering, University of California Merced, Merced, California, USA. [b] Department of Forestry, Mississippi State University, Starkville, MS, USA. [c] Department of Civil and Environmental Engineering, University of California, Berkeley, Berkeley, California, USA. * Corresponding author: gcui3@ucmerced.edu

Highlights

- Water stress is expressed based on precipitation (*P*) minus evapotranspiration (*ET*).
- Cumulative *P–ET* relates to vulnerability reflected by moisture loss and mortality.
- Dense lower-elevation forests are more vulnerable during multi-year droughts.
- An LSTM model predicts *ET* (testing r^2=0.72) and water availability (r^2=0.99).
- Historical-minimum annual *P–ET* portends water stress in multi-year droughts.

Abstract

Water availability in mountain forests affects vegetation response to drought, which in turn changes evapotranspiration (*ET*). We investigated water-balance indicators based on precipitation (*P*) minus *ET* to assess Mediterranean-climate forest vulnerability to multi-year droughts. We used the drought-vulnerable dense mixed-conifer forests of California's Sierra Nevada, which includes 78 groves of giant sequoia as study area. With long-term Landsat-based *ET* data during 1985-2018, water-stress patterns at 30-m resolution during two historical droughts (1987-92 and 2012-15) were analyzed. Canopy moisture loss and tree mortality were used as indices of drought vulnerability. Using cumulative multi-year *P–ET* as an indicator, groves that were water stressed in 1987-92 were more vulnerable in California's unprecedented 2012-15 drought. Historical-minimum annual *P–ET* is an indicator of water stress, explaining 32% and 29% of the variance of canopy moisture loss and tree mortality, respectively. As an extreme test to explore potential vegetation response, we trained a deep-learning Long Short-Term Memory (LSTM) model to project *ET* during hypothetical extended-drought scenarios. The LSTM model reasonably predicted *ET* with r^2 of 0.72 for the testing period. Annual *P–ET* using LSTM-based *ET* agreed (r^2=0.99) with that using *ET* values from Landsat. Historical water-stress-prone areas were projected to suffer larger *ET* decreases and to experience more-severe stress during a 12-yr drought scenario. Water stress is more severe in lower-elevation forests, versus mid-to-high areas that have higher precipitation and shorter growing season under current climate. Our study provides water-balance-based indicators to project drought vulnerability and assess effects of disturbance in forests in a warming climate.

Keywords: Water balance; Multi-year drought; Evapotranspiration; Giant sequoia; Vulnerability; Water stress

1 Introduction

Droughts are projected to be more widespread and extreme in terms of frequency, intensity, and duration due to anthropogenic climate warming (Mann and Gleick, 2015; Moravec et al., 2021; Williams et al., 2020), which may severely challenge the current resistances of environmental systems (Vicente-Serrano et al., 2020). Drought-induced tree mortality has been observed in many forest biomes, and profoundly affects ecological and societal systems (Allen et al., 2015, 2010; Anderegg et al., 2019, 2016). Droughts can potentially alter forest ecosystems and impact the feedbacks between the biosphere and other Earth systems (Adams et al., 2010, 2009; McDowell and Allen, 2015), including on albedo, water and near-ground energy budgets, wildfire, insect outbreaks, and potential flips between being a carbon sink versus carbon source. Hydraulic failure (Arend et al., 2021; McDowell and Allen, 2015; Olson et al., 2018), beetle attack (Stephenson et al., 2019; Stephenson and Das, 2020), and topography (Stovall et al., 2019) interactively contribute to tree mortality. As water balance substantially influences tree growth (Hember et al., 2017; Williams et al., 2013), water-stressed forest areas during drought can show tree mortality.

Vegetation plays a central role in modulating Earth's water cycle. Plant transpiration is a dominant part of the water-balance component evapotranspiration (*ET*) (Saksa et al., 2017; Schlesinger and Jasechko, 2014; Scott et al., 2021; Zhu et al., 2015). Tree size also plays an important role in plant transpiration, since larger trees in a given forest can use more water (Aparecido et al., 2016; Dawson, 1996). Besides having overstocked mixed-conifer forests that evapotranspiration demand can exceed water availability during multi-year droughts (Goulden and Bales, 2019), the southern Sierra Nevada is home to an especially large and water demanding species, the giant sequoia. The giant sequoia (*Sequoiadendron giganteum* (Lindl.) J.Buchholz) is the largest tree on Earth, with a height of up to 90 m and a life span of over 3000 years (Stephenson, 1996). Giant sequoias naturally live mixed with other tree species in fragmented groves within a narrow mid-elevation range (1400 to 2200 m) on the west slope of California's Sierra Nevada (Stephenson, 1999), which is characterized by a Mediterranean climate with cool wet winter and dry summer. The distribution of giant sequoias appears to favor available water from precipitation (DeSilva and Dodd, 2020) and abundant soil moisture (Rundel, 1972), possibly augmented by subsurface flow from higher elevations (Weatherspoon, 1986). To maintain favorable water status, giant sequoias can make adjustments in hydraulic architecture at leaf, branch, and whole-tree scales, partially compensating

the increasing hydraulic limitations with tree height (Ambrose et al., 2016; 2018). Giant sequoias have high resistance to insects, disease, and fire damage (Hartesveldt et al., 1975; Swetnam, 1993) that may accompany droughts. The prolonged, severe California hot drought from 2012 to 2015 was associated with extensive forest die-off in the Sierra Nevada (Brodrick and Asner, 2017; Goulden and Bales, 2019; Restaino et al., 2019). Since giant sequoias have relatively higher water availability, sequoia groves may act as hydrologic refugia for climate extremes (McLaughlin et al., 2017; Su et al., 2017). However, apparent foliage dieback was also observed in giant-sequoia groves during the unprecedented 2012-15 drought (Stephenson et al., 2018), coincident with lower available water (Nydick et al., 2018; Paz-Kagan et al., 2018).

Vegetation changes during drought affect the water balance in mountain forests, e.g. water-stress-induced tree mortality causes *ET* decreases. Tree mortality during droughts can be measured at leaf and landscape scales (Ambrose et al., 2018; Stephenson et al., 2018); however, on-the-ground measurements are often time consuming, expensive, and limited in space and time. Forest water-stress-relevant data at the landscape or regional scales are often needed for drought assessment and forest management. Remote sensing can provide large-scale data, such as Canopy Water Content (CWC). As a variable that integrates leaf-water content and leaf-area index, CWC was measured by High Fidelity Imaging Spectroscopy (HiFIS) in 2015 and 2016 throughout California, showing its landscape-scale variation and relationship to foliage dieback (Martin et al., 2018; Nydick et al., 2018; Paz-Kagan et al., 2018). Large-scale forest drought resistance mapped based on the 30-m-resolution CWC (Asner et al., 2016; Brodrick et al., 2019) showed significant variability during California's 2012-15 drought. Another indicator of available soil moisture based on landscape surface characteristics is Topographic Wetness Index (TWI) (Western et al., 1999). For example, sequoia groves have higher TWI than other forested areas (Ray, 2016; Su et al., 2017), further suggesting they may receive water subsidies from outside to support their large water demand.

Long-term satellite-based Normalized Difference Vegetation Index (*NDVI*) offers valuable information on vegetation response across the globe. This greenness index has been used as an early warning signal of forest mortality (Liu et al., 2019; Rogers et al., 2018), in mapping mortality (Furniss et al., 2020; Meddens et al., 2013), and in investigating vegetation responses to drought (Warter et al., 2020). Meanwhile, there exists a robust relation between Landsat *NDVI* and annual *ET* measured by flux towers (Goulden et al., 2012; Goulden and Bales, 2019; Ma et al., 2020; Maurer, 2021; Roche et al., 2018), providing a way to estimate *ET* at a resolution of 30 m based on vegetation condition. A spatially mapped water-balance-based water-stress indicator, cumulative multi-year precipitation minus evapotranspiration (*Cum. P–ET*), was found to be closely linked to forest die-off during California's 2012-15 drought, reflecting moisture overdraft and deep soil drying (Goulden and Bales, 2019). One advantage over other water-stress-relevant variables (e.g. climatic water deficit and vapor pressure deficit), the metric based on *P–ET* integrates vegetation response (reflected by *ET)* and water availability at a 30-m scale, making it potentially useful to investigate water stress in high-*ET*-demand forests during prolonged multi-year drought.

Forest actual *ET* can reflect vegetation response to climate variability and other disturbance. For example, forest *ET* decreases during drought due to water-stress-induced tree mortality, and also decreases after wildfire (Ma et al., 2020). However, there exists a time-lag effect (i.e. memory effect) in the complex relationship between vegetation response and climate (Ogle et al., 2015; Zhao et al., 2020), required to be modeled by non-linear approaches (Kraft et al., 2019; Papagiannopoulou et al., 2017). As a type of recurrent neural network with the ability to memorize system internal state, the deep-learning Long Short-Term Memory (LSTM) network has been applied to time-series data in natural systems (Gauch et al., 2021; Kratzert et al., 2019; Reichstein et al., 2019). The state-of-the-art LSTM model has been applied to estimate reference *ET* (Z. Chen et al., 2020; Yin et al., 2020) and actual *ET* (J. Chen et al., 2020; Granata and Di Nunno, 2021). Yet, long-term satellite-based actual *ET* data has not yet been investigated by the LSTM model.

This study focused on the assessment of water availability in mountain forested areas during multi-year droughts. Specifically, we used California's giant-sequoia groves as an example of high-*ET* Mediterranean forests, as the endangered world's largest tree is expected to have high water consumption. We investigated water-balance-based indicators using gridded *P* and *ET* data to assess forest drought vulnerability, which has specific significance for emerging climate change risks for forests around the world. With long-term data during 1985-2018, the water availability during two historical multi-year droughts was assessed and compared between giant-sequoia groves and non-grove control areas. To evaluate the applicability of water-balance-based indicators, we developed an interpretable deep-learning model to project *ET* during hypothetical extreme-drought scenarios, which were also used as a stress test to explore potential vegetation response. We hypothesized that i) giant-sequoia groves have higher *ET* and encounter more-severe water stress than surrounding non-grove forests; ii) water stress during multi-year droughts shows difference along elevation gradients inside high-*ET* areas, and iii) historically water-stressed areas tend to suffer water stress during subsequent multi-year droughts, mimicking their response and vulnerability during historical droughts.

2 Data and methods

Our study domain is located in the Sierra Nevada of California, including all 78 giant-sequoia groves (Figure 1). We used a water-balance-based indicator, water availability (*P–ET*), to investigate water stress and tree die-off in the groves during multi-year droughts (Figure 2). For historical droughts, we determined cumulative water availability (*Cum. P–ET*) and linked it with tree mortality and vegetation moisture loss. To assess grove vulnerability during

hypothetical more-extreme droughts, we used an interpretable deep-learning LSTM model to simulate *ET* and to project the water-stress metric *Cum. P–ET* and moisture loss. The data-driven LSTM model was developed using 34 years of historical data to learn vegetation response to climate variability. Two extended scenarios, i.e. 8-year and 12-year droughts, were designed as stress testing to investigate possible changes of *ET* and water stress in more-extreme droughts.

2.1 Study area

The study domain ranges from the American River basin in the north to the Kern River basin in the southern Sierra Nevada (Figures 1 and S1), including 78 giant-sequoia groves (Willard, 1994). We obtained 70 grove boundaries from the Sequoia and Kings Canyon National Parks (also used in Su et al. (2017) for investigation of vegetation indices), and added the other 8 grove boundaries based on giant-sequoia trails map (http://www.redwoodhikes.com/Sequoias.html) and DeSilva and Dodd (2020). In the groves, giant sequoia grows in a mixed conifer forest with various tree species. Dominant overstory tree species in groves are white fir (*Abies concolor* (Gordon) Lindl. ex Hildebr.) with high stem density, and giant sequoia with relatively high canopy cover and basal area (Christiansen, 1975; Meyer and Safford, 2011; Rundel, 1971). Other common species include sugar pine (*Pinus lambertiana* Douglas), ponderosa pine (*Pinus ponderosa* Douglas ex C. Lawson), incense-cedar (*Calocedrus decurrens* (Torr.) Florin), and California black oak (*Quercus kelloggii* Newb.). According to the Sequoia Tree Inventory (STI) conducted in one-third of all groves in the 1960s and 1970s (USDA, 2013), giant sequoia averages 3% of trees in groves, but 26% of basal area. The density of large sequoia (trunk diameters >1.07 m) is estimated as 2.61 large sequoias/acre (Stephenson and Brigham, 2021). The total area of all groves is 155 km^2 (Table 1). We classified groves based on their size ranking and cumulative areas (Guo et al., 2013). Over half (53%) of the all-grove area was in the largest seven groves, which were classified as large-size grove; 13 groves accounting for 32% were classified as medium-size, and the remaining 58 were small-size, together covering 15% of the all-grove area. Average elevations of groves range from 1120 to 2350 m using 30-m digital elevation data from the Shuttle Radar Topography Mission (SRTM, Farr et al., 2007). Based on the 33rd (1830 m) and 66th (1950 m) percentiles of elevation, groves were also classified as low (25 groves), medium (26), and high (27) elevation.

For comparison to the groves containing giant sequoia, we specifically chose forested areas (>95% of area classified as conifer, hardwood, or mixed forest) surrounding groves within 500-1000 m distance as non-grove controls (199 km^2, Figure 1). We used vegetation data from the USDA Forest Service Region 5 (https://www.fs.usda.gov/detail/r5/landmanagement/resourcemanagement/?cid=stelprdb5365219) and CALFIRE Fire and Resource Assessment Program (FRAP) (https://map.dfg.ca.gov/metadata/ds1327.html). The vector layer data of vegetation cover type and dominant vegetation alliances from the Region 5 dataset were rasterized to a 30-m resolution, the same as that of raster data of tree size and tree canopy cover from the FRAP dataset. Although grove and control areas had a similar composition of vegetation cover type (82% area is conifer, 13% mixed forest, and 2% hardwood, Figure S2a), control areas showed a different forest composition, excluding vegetation alliances of giant sequoia or mixed conifer-giant sequoia (Figure S2b). In terms of forest structure, the portions of medium/large tree size and dense canopy cover were higher in giant-sequoia groves than in the control (Figures S2c,d). As a critical structural characteristic of forests (Chen et al., 1997; Parker, 2020), Leaf Area Index (LAI) represents site occupancy integrating tree size, stand density, and site resource supply (Peduzzi et al., 2012; Vose and Allen, 1988). Thus, annual LAI data from 500-m MODIS MOD15A2H product (Myneni et al., 2002) were bilinearly interpolated to 30-m resolution. Using the median values of 2001-2018 annual LAI, giant-sequoia groves showed a larger mean than did the controls (2.10 versus 1.88, Figure S3a), consistent with their relatively larger tree size and denser canopy.

2.2 Water-balance indicators and linkage to tree die-off

We evaluated cumulative water availability (*Cum. P–ET*) during multi-year drought and historical-minimum annual *P–ET* as water-stress indicators for drought vulnerability assessment, reflecting sustained moisture overdraft and change of subsurface storage (Bales et al., 2018; Roche et al., 2020). Goulden and Bales (2019) found that *Cum. P–ET* can be negative during multi-year droughts, which has a strong statistical relationship to tree die-off in Sierra Nevada.

Annual water-year (October-September) water availability (*P–ET*) at 30-m resolution from 1985 to 2018 was calculated using gridded *P* from the Parameter-elevation Relationships on Independent Slopes Model data (PRISM, http://www.prism.oregostate.edu) and *NDVI*-based *ET*. The widely used PRISM data were developed based on ground measurements at 13,000 sites (Daly et al., 2008, 1994). To match the 30-m resolution in our study, the 800-m PRISM data were downscaled by bilinear interpolation (Goulden and Bales, 2019; Jin et al., 2018; Lany et al., 2020) and summed by water year. Compared to annual precipitation measured by rain gauge at Calaveras Big Trees (CVT) around North Calaveras Grove, the 30-m PRISM data showed good agreement with root-mean-square error (RMSE) of 74 mm and mean absolute percentage error (MAPE) of 3.88%. To spatially and temporally estimate gridded annual *ET*, previous studies (Goulden and Bales, 2019, 2014; Ma et al., 2020; Roche et al., 2020) have developed a non-linear-regression between *ET* measurements and annual *NDVI*. With 77 site-years of annual *ET* data (unit of mm) from 10 eddy-covariance flux towers from Goulden and Bales (2019) and our processed *NDVI* (described below), a non-linear exponential regression (Equations 1 and Figures S4-S5) was fitted by minimizing least squares.

$$ET = 123.385 \times \exp(2.8539 \times NDVI) \qquad (1)$$

Using Google Earth Engine cloud-computing environment (Gorelick et al., 2017) to process *NDVI* time series (Huang et al., 2017; Ma et al., 2020; Roche et al., 2020; Sankey et al., 2021), we collected *NDVI* at a 30-m resolution from US Geological Survey (USGS) Landsat Collection Tier 1 surface reflectance data (https://www.usgs.gov/core-science-systems/nli/landsat/landsat-collection-1-surface-reflectance; Masek et al., 2006; Vermote et al., 2016). Annual *NDVI* was the water-year mean of all Landsat scenes, filtered for shadows, water, and snow (Zhu and Woodcock, 2012). Due to the differences in surface reflectance across Landsat missions (Landsat 5, Landsat 7, and Landsat 8), their derived *NDVI* data (Figure S3c) can show noticeable differences (Claverie et al., 2015; Su et al., 2017). Thus, to obtain consistent *NDVI* data over a long period 1985-2018, we homogenized *NDVI* data from Landsat 5 and Landsat 8 to Landsat 7 (Goulden and Bales, 2019; Su et al., 2017; Sulla-Menashe et al., 2016), using regression equations developed based on common data during overlapping periods across Landsat missions (Figure S5c).

Tree mortality data were obtained from annual U.S. Forest Service (USFS) Aerial Detection Surveys (ADS, https://www.fs.usda.gov/detail/r5/forest-grasslandhealth/?cid=fsbdev3_046696), typically performed in summer when forest damage or mortality are most visible. Trained surveyors visually estimate and record dead Trees Per Acre (TPA) as a polygon attribute of delineated regions with visible mortality (Byer and Jin, 2017). ADS vector layers were rasterized to TPA data across flown areas. We then generated annual TPA at 30-m resolution by averaging TPA data and inserting zero for mortality-free areas inside flown areas (Goulden and Bales, 2019).

Vegetation moisture loss, indicated by *NDMI* change (i.e. Δ*NDMI*), was correlated with tree mortality and widely used for spatial mapping (Goodwin et al., 2008; Goulden and Bales, 2019; Roberts et al., 2019; Van Gunst et al., 2016). Tree mortality inferred from Δ*NDMI* complements originally coarse-scale TPA data from USFS ADS, which depends on surveyors' visual interpretation and can be limited by poor flight conditions (Byer and Jin, 2017). Thus, we used summer Landsat *NDMI* images, coincident with when USFS ADS were generally conducted. Similar to the *NDVI* homogenization procedure, we homogenized mean *NDMI* data in late summer (July-September, Figure S5d).

2.3 Interpretable deep-learning model for water-stress prediction

To predict *ET* and represent vegetation response to climate variability and drought inside densely forested groves, we used a deep-learning LSTM model trained by a 34-year time series (1985-2018). The LSTM model overcomes exploding and vanishing gradient problems in traditional recurrent neural networks (Hochreiter and Schmidhuber, 1997; Shen et al., 2018). An LSTM layer has recurrently connected memory cells to store and process sequential information, allowing the neural network to learn long-term or short-term dependencies in natural systems (Figure S6). The LSTM model has been used to predict watershed runoff (Gauch et al., 2021; Kratzert et al., 2019), water-table depth (Zhang et al., 2018), vegetation state (Kraft et al., 2019), and river water quality (Zhi et al., 2021). Each LSTM memory cell is updated at each time step by a set of activations (e.g. three information gates: input, forget, and output gates) and two states (i.e. cell state and hidden state). The fully connected dense layer and dropout layer were added after the LSTM layer to improve fitting ability and avoid overfitting, respectively (Kraft et al., 2019; Zhang et al., 2018). The forward pass of the LSTM model can be described mathematically by Equations S1-S6. Model settings, including hidden neurons, activation function, and dropout rate, are shown in Table S1. The LSTM model was implemented in the open-source machine-learning frameworks Tensorflow and Keras.

The LSTM model inputs consist of 4 dynamic forcing data at each annual time step, including precipitation and temperature data, previous *ET*, and fire perturbation (Table 2). Additionally, we used 21 static features as inputs, including vegetation condition, meteorological normal, historical-minimum *P–ET*, snowpack storage, topography, soil and subsurface properties (Table 2). In total, there were 25 LSTM input features at each 30-m pixel inside giant-sequoia groves. We preprocessed all 25 input features and target *ET* data with a standard transformation by subtracting their mean across all pixels over our study period, and then dividing the difference by their standard deviation. We used a rolling window approach to prepare standardized input data of shape (batch size=1000, sequence length=5, feature number=25) and standardized target *ET* of shape (batch size, 1). In this study, we chose a sequence length of 5 (i.e. a look-back of 5 years), which may sufficiently reflect recent vegetation change, considering that: a) 5-years-before-fire *ET* was often used to investigate wildfire effects in the Sierra Nevada (Ma et al., 2020; Roche et al., 2020), and b) the short-term (mean value of 5 years) of vegetation-type conversion in forests caused by drought-related mortality (Batllori et al., 2020). Though a larger value of sequence length can be used, the number of available data for training the model would be reduced, and more historical data would be required for *ET* prediction. The LSTM model was trained using the Adam optimization with a loss function of mean squared error. For a total of 21,4126 pixels inside groves, the target *ET* data were split into training period (1990-2000 and 2009-2018), validation period (2001-2004), and testing period (2005-2008), corresponding to 72%, 14%, and 14% of all data, respectively. With an initial learning rate of 0.001, the model learning rate was adjusted by the reduce-learning-rate-on-plateau and early stopping schedulers in Keras.

Although the LSTM model can predict vegetation response reflected by *ET*, the model does not explain how the 25 input features have contributed to *ET* prediction. Here we use a game-theoretic approach, called SHapley Additive exPlanations (SHAP; Lundberg and Lee, 2017), to interpret the LSTM model's output and to analyze relationships hidden in the black-box model (Batunacun et al., 2021; Vega García and Aznarte, 2020). Simply put, an input feature with a larger SHAP value relatively contributes to higher output, allowing us to identify possible drivers for *ET* reduction or tree die-off

during droughts. More descriptions about SHAP can be found in Text S2 and Lundberg and Lee (2017). The SHAP-based attribution analysis was implemented using the python SHAP package (https://shap.readthedocs.io/).

As a stress test to explore potential vegetation response to extended and acute drought conditions, we used the LSTM model to predict *ET* during hypothetical, extreme-drought scenarios. Since the 2012-2015 drought is the unprecedented, worst multi-year drought in the instrumental record in California, we simply designed two scenarios by extending the 2012-15 drought, similar to the approach used in Flint et al. (2018) for evaluating hydrologic results and water supply in extreme drought scenarios. We chose to directly investigate vegetation response reflected by actual *ET* during extreme scenarios, rather than assessing vegetation evolution using long-term projections of climate change. Therefore, we repeated the 2012-15 drought (same precipitation and temperature) after 2015 to generate 8-year and 12-year drought scenarios, respectively. We then applied the LSTM model to predict and analyze the actual *ET* and water-stress patterns.

3 Results

3.1 Water-stress patterns during historical multi-year droughts

During the unprecedented 2012-15 drought, vegetation moisture (*NDMI)* and greenness (*NDVI)* inside our study domain decreased significantly (Figure S5). At our domain scale, *Cum. P–ET* during the drought was correlated to drought vulnerability reflected by vegetation moisture loss and ADS dead trees (Figure 3), as was previously reported for the entire Sierra Nevada (Goulden and Bales, 2019). By developing fitted equations in Figures 3c and 3d, the moisture loss and TPA (dead tree per acre) were linked to water-balance-based *Cum. P–ET*. The variance of TPA (moisture loss) explained by *Cum. P–ET* is 34% (48%) in our domain, smaller than that of 51% (60%) using the significantly larger dataset for the entire Sierra Nevada (Figure 1), which is five times the area of our study domain (Goulden and Bales, 2019). Temperature positively correlated to TPA (Pearson correlation coefficients r of 0.31) and precipitation showed a negative correlation (r=-0.36). Their correlations were weaker than that (r=-0.66) between *Cum. P–ET* and dead tree TPA. Using a significantly lesser amount of data inside 78 giant-sequoia groves (1.4% of domain area) for regression (Figure S7a), *Cum. P–ET* can still explain 35% of the variance of Δ*NDMI* (Figure S7b), but cannot describe ADS dead tree (Figure S7c), apparently due to the coarse resolution of ADS data relative to grove size. Both *ET* and LAI decreased during the 2012-15 drought due to tree mortality (Figures S8a,b). The median LAI for 2001-2018 in our study domain shows a strong postive correlation to *NDVI* (r=0.75), consistent with previous studies (Carlson and Ripley, 1997) and reflecting the fact that high annual LAI can drive high annual *ET* (Goulden and Bales, 2019). The change of LAI correlated to water-stress *Cum. P–ET* (r=0.57, Figure S8c) and ADS dead trees (r=-0.55, Figure S8d). As the water-balance-based *Cum. P–ET* correlates to moisture loss, ADS dead trees, and LAI change, we used *Cum. P–ET* as one indicator of forest vulnerability during multi-year drought.

Using 34-year data (1985-2018, Figure 4), we found that giant-sequoia groves had an average of 64 mm yr^{-1} higher *ET* (statistically significant with p-value <0.001 from a two-tailed Student's t-test) than surrounding non-grove control areas, which is consistent with larger LAI and larger portions of medium/large tree size and dense canopy cover in the groves (Figures S2c,d and S3a). There is no statistically significant difference (p-value=0.83) in precipitation between groves and the control, though the value averaged 18 mm yr^{-1} lower in groves. Put together, water availability (*P–ET*) was 82-mm yr^{-1} lower (insignificant with p-value=0.36) in groves than in the control (Figures 4a,b). The annual vegetation greenness *NDVI* and summer canopy moisture *NDMI* in groves were 0.036 and 0.055 higher (statistically significant with p-values <0.001) than those in control areas, respectively. During the 1987-92 and 2012-15 droughts, *NVDI* in both groves and control areas decreased by 0.047, accounting for 7.5% of the mean 1985-2018 *NDVI* across the two areas (Figure 4c). Meanwhile, canopy moisture noticeably declined during the two droughts, as shown by a mean *NDMI* decrement of 0.050, accounting for 14.3% of mean *NDMI* (Figure 4d). For the groves, the 2012-15 drought had a more-pronounced moisture loss (*NDMI* decrement of 0.082) than did the 1987-92 drought (0.025), consistent with lower water availability (*P–ET*, –290 mm) averaged during the 2012-15 drought than during the 1987-92 drought (–36 mm).

Cumulative *P–ET* in giant-sequoia groves was more negative than in non-grove control areas and the study domain during the two historical droughts (Figure 5). For the 2012-15 drought, the 50th percentile *Cum. P–ET* values in groves were 337 and 1044 mm smaller than the control and domain, respectively. Ninety-five percent of grove areas had some water-stress vulnerability (negative *Cum. P–ET*) during the 2012-15 drought, compared to 65% during the 1987-92 drought. In terms of water-stress severity in groves, *Cum. P–ET* during the 2012-15 drought averaged –1250 mm, which was 4 times that (–295 mm) during the 1987-92 drought. As *Cum. P-ET* is well correlated with moisture loss (Figure 3b), *NDMI* decrement during the 2012-15 drought was expected to be larger than the 1987-92 drought, which was consistent with Landsat *NDMI* observation (Figure 4d).

For the high-*ET* grove areas, *ET* showed variability inside and across groves during the two droughts (Figures S9a,b). The grove-mean *ET* during the 2012-15 drought averaged 67 mm higher than that during the 1987-92 drought due to higher average *NDVI* (Figure 4c). We observed a decreasing trend of *ET* along elevation across groves during the two droughts (Figure S9c), as indicated by negative linear-regression slopes with p-value<0.002 from a two-sided Wald test. In terms of forest composition and structure across groves grouped by elevation (Figure S10), low-elevation groves were associated with slightly smaller portions of conifer vegetation and medium/large trees, but showed a larger portion of dense canopy cover than did the medium- and high-elevation groves, consistent with relatively higher LAI in low-elevation groves

(Figure S3b). Meanwhile, grove-averaged elevation negatively correlated to LAI (r=-0.57, Table 1), indicating that groves in lower elevations tend to have higher LAI, coincident with their greater *ET* and a longer growing season.

Across-grove assessment (Figures 6a,b) shows that 77 out of the 78 giant-sequoia groves suffered water stress (negative grove-averaged *Cum. P–ET*) during the 2012-15 drought, versus 54 stressed groves during the 1987-92 drought. The lowest grove-level *Cum. P–ET* during the 2012-15 drought reached –2049 mm, which was 311 mm lower than that (–1738 mm) during the 1987-92 drought. For the more-severe 2012-15 drought, the only grove associated with water surplus was Placer Big Trees, which is located in the furthest north of our study domain and receives the largest precipitation (Table 1). Some groves (e.g. Giant Forest) were partly water-stressed, showing within-grove variability of available water. The distributions of *Cum. P–ET* during 2012-15 were narrower and shifted to more-negative values than during 1987-92 (Figures 6a,b). The groves with a larger standard deviation of *Cum. P–ET* during 1987-92 tended to show a larger shift to more-negative values during 2012-15 (Spearman rank correlation coefficients ρ=0.35). Cumulative *P–ET* showed a statistically significant increasing trend (a positive linear-regression slope with p-value= 4×10^{-5} from a two-sided Wald test) along groves sorted from the lowest to highest elevation in the 1987-92 drought (Figure 6c), and an increasing trend (a positive regression slope with insignificant p-value=0.16) during the 2012-15 drought. Meanwhile, the Spearman correlations between grove elevation and *Cum. P–ET* were 0.36 and 0.23 for the 1987-92 drought and 2012-15 drought, respectively, indicating that higher-elevation groves suffered relatively less water stress, due to their higher *P*, shorter growing season, and lower *ET*.

Groves experiencing water stress during the 1987-92 drought tended to show more negative *Cum. P–ET* in the later 2012-15 drought (Figure S11a), revealing that historically stressed groves have less drought resistance, i.e. vulnerable groves could encounter much greater water stress under hotter and drier climate conditions. However, in terms of *Cum. P–ET* difference between the two droughts (Figure S11b), groves with larger *Cum. P–ET* during the 1987-92 drought were associated with larger decreases of *Cum. P–ET*, indicating that less-water-stressed and water-surplus groves experienced a more considerable loss of water availability during more-severe drought, due to their relatively larger decrease of *Cum. P* and smaller decrease of *Cum. ET* (Figures S11c,d).

3.2 Predictability and drivers of ET from LSTM model

The deep-learning LSTM showed a good performance for predicting *ET*, with training data covering two historical multi-year droughts (Figure 7). The coefficients of determination (r^2) were 0.91, 0.69, and 0.72, respectively, for model training, validation, and testing. The RMSEs were 43, 71, and 70 mm yr^{-1}, respectively. Although the LSTM model had a slightly larger discrepancy at higher *ET* for testing (Figure 7b) compared to training (Figure 7a), most *ET* predictions (filled by warm colors) were consistent with Landsat *NDVI*-based *ET*. Annual water availability (*P–ET*) estimated using deep-learning-based *ET* showed good agreement (r^2>0.99) with that using Landsat-based *ET* (Figure S12).

For the 4 dynamic forcing inputs, higher precipitation (*P*) and temperature (*T*) values in current year, and *ET* in previous year (ET_p) contributed to a higher *ET* prediction, which is illustrated by red dots having higher feature values being mainly distributed in the positive SHAP zone (Figure 8), with the feature value positively correlated to SHAP values (Figure S15). Higher fire occurrence (Fire) results in lower predicted *ET* due to burned vegetation. The static-feature historical-minimum *P–ET* is the dominant input (Figure 8) for *ET* prediction. There exists a negative relation between *Min. P–ET* and SHAP values (Figure S15a). Lower negative *Min. P–ET* (blue in Figure 8) increases *ET* prediction during the 2012-2015 drought, since most grove areas reached their minimum values of 1985-2018 annual *P–ET* during the severe hotter drought, reflecting higher *ET* demand not being supported by available water. The static-feature historical-normal temperature in 1985-2010 (T_m) ranks in the top five dominating features (Figure S14), with higher values reducing *ET* prediction, partly due to higher T_m often associated with lower precipitation. As higher-latitude areas receive more precipitation in the Sierra Nevada, latitude (Lat) positively contributes to *ET* prediction. A higher level of vegetation cover increases *ET*, as indicated by normal vegetation condition ($NDVI_m$) and tree canopy cover percentage (CanPct). Lower-elevation areas (Ele) are generally warmer with less snow storage (SWE), thus increasing *ET* prediction. Soil-available water-holding capacity (AWC) is characterized by soil texture (i.e. clay, silt, and sand), which did not show apparent driving effects on *ET* prediction. However, a higher subsurface permeability contributes to higher *ET*, indicating that subsurface water may be more easily transported above for supporting *ET* use. Other features show ambagious driver effects and are not dominant factors for *ET* prediction in the LSTM model (Figure S14).

3.3 Water-stress investigation for extreme drought scenarios

ET values in giant-sequoia groves during both 1990-2015 and two extended drought scenarios (Figure 9) were predicted by the LSTM model. *ET* predictions for 1990-2015 agreed with Landsat-*NDVI*-based data (Figure 9c, r^2=0.93, RMSE=14 mm). During the drought scenarios, actual *ET* was projected to decrease, reflecting possible tree die-off. Note that we did not explicitly separate soil evaporation from actual *ET*, and plant transpiration is the dominant part of actual *ET* (Saksa et al., 2017; Scott et al., 2021; Zhu et al., 2015). As soil evaporation may increase after widespread tree mortality (Biederman et al., 2014), the trade-off between soil evaporation and mortality was not investigated in this study. The *ET* decreased 230 mm in 2019 relative to 2015, larger than the 40-mm drop in 2023 relative to 2019, suggesting a dramatic reduction of vegetation or available water in the middle four years of the 12-yr scenario. A non-linear relation between *ET* and *NDMI* at 30-m resolution inside groves was observed. The fitted equation *NDMI*=0.426×ln(*ET*)–2.459

explained 56% of the variance in 1985-2015 (Figure S16). *ET*-based *NDMI* was consistent with that observed 1987-1991 and 1996-2013, with noticeable differences immediately after dry 1992 (Figure 9d). The underperformance of *ET*-based *NDMI* after drought may not significantly affect the interpretation of relative drought vulnerability exhibited by moisture loss (i.e. Δ*NDMI*) during droughts. For drought scenarios, *NDMI* was projected to decrease, following the *ET* pattern.

Four of the 78 groves were projected with water surplus (Figure 10), which was greater during the 12-yr versus 8-yr drought (Figure 10c), due to their relatively large *P* and projected *ET* decrease in 2020-2023 (Figure 9c). Compared to the 8-yr drought, *Cum. P–ET* averaged lower in 42 groves during the 12-yr drought, reaching a minimum of -3520 mm (Figure 10b). Cumulative *P–ET* tended to increase with elevation (Figure 10c, positive linear-regression slopes with insignificant p-values of ~0.26) during two scenarios, and their Spearman rank correlations were ~0.27. Comparison between the historical 2012-15 drought and 8-yr scenarios shows that *Cum. P–ET* decreased in 70 groves (Figures S17a,b). Cumulative *P–ET* exhibited a strong positive correlation across the historical drought and two scenarios (Figures S17a,c), showing that previous seriously water-stressed groves may continuously suffer water stress. Meanwhile, these water-stressed groves tended to have larger drops of *Cum. P–ET* in prolonged droughts (Figures S17b,d). This tendency of *Cum. P–ET* drops during prolonged-drought scenarios is different from the observed larger drops of *Cum. P–ET* in less-water-stressed groves in the two historical droughts (Figures S11b,d). Because the decrease in *P* was more pronounced in less-water-stressed groves between the two historical droughts, however, this spatial variability of *P* decrease was not accounted for in the prolonged-drought scenarios, which were constructed by repeating 2012-15 *P* at each pixel.

Cumulative *P–ET* during the 2012-15 drought showed a positive correlation to projected mean annual *ET* difference (12-yr drought scenario minus 2012-15 drought) and percent of *ET* difference with correlations (r) of 0.68 and 0.58, respectively (Figures 11a,b). This indicates that previous seriously water-stressed groves tend to suffer larger *ET* drops during prolonged-drought scenarios, which is in line with that observed tendency during the two historical droughts (Figure S11d). On average, mean annual *ET* in the 12-yr scenario decreased by 160 mm (19%) compared to 2012-15, while the largest annual *ET* drop was 310 mm (34%). Moisture loss in groves (Figure 11c), i.e. projected *ET*-based *NDMI* in 2023 minus mean Landsat *NDMI* of 2009-2011, was estimated by *ET* (Figure S16), not using the fitted equation with *Cum. P–ET* (Figure 3b). The rationale is that *Cum. P–ET* may increase due to *ET* reduction in some groves. Projected cumulative *P–ET* does not represent the additional *ET* feedback during prolonged droughts, resulting in a complicated relationship between *Cum. P–ET* and Δ*NDMI* (Figure S18). Similarly, we suspected that the strong correction between *Cum. P–ET* and dead tree TPA during historical droughts (Figure 3d) may have limited prediction ability for the extreme scenarios. Thus, the dead TPA for scenarios was not estimated, while we expected larger tree mortality indicated by larger canopy moisture loss and *ET* drop. The Δ*NDMI* in groves enables the assessment of relative vulnerability to extreme droughts. Cumulative *P–ET* during the 2012-15 drought showed a positive correlation (r=0.57) to projected Δ*NDMI*, suggesting that historically water-stressed groves tend to lose more canopy moisture in extreme drought scenarios.

3.4 Indicators for drought vulnerability

Pixel-level correlations between *Cum. P–ET*, Δ*NDMI*, and 21 static features inside groves during historical and simulated droughts were calculated (Figure 12). *Cum. P–ET* values during the three droughts are positively correlated (r>0.5), again indicating that vegetations in historically water-stressed areas might continue to suffer more-severe water stress. Δ*NDMI* during the 12-yr drought scenario correlated (r=0.3) to that during the 2012-15 drought, but was not closely related to that during the 1987-92 drought. Vegetation condition ($NDVI_m$) and tree canopy cover percentage (CanPct) showed negative correlations to *Cum. P–ET* and Δ*NDMI*. As indicated by the strong positive correlation between *NDVI* and *ET* (Figure S4; Goulden et al., 2012; Goulden & Bales, 2014, 2019; Ma et al., 2020; Roche et al., 2020), denser-vegetation areas (indicated by higher *NDVI* or larger canopy cover percentage) are expected to have larger water consumption by plants (larger *ET*). During multi-year droughts, higher *ET* can lead to more negative *Cum. P–ET* (more-severe water deficit) and thus more moisture loss (more negative *ΔNDMI*) in denser-vegetation areas, since *Cum. P–ET* is closely correlated to *ΔNDMI* (Figure 3c; Goulden and Bales, 2019). Elevation, *P*, and SWE were positively correlated to *Cum. P–ET*, since higher-elevation areas have larger precipitation and snowpack storage. *ET* demand increases with temperature and thus is negatively correlated with *Cum. P–ET*. Positive (negative) correlations between latitude (longitude) and *Cum. P–ET* suggest that areas located North and East would have less water stress due to higher *P*. Negative correlations between slope and *Cum. P–ET* and *ΔNDMI* indicate that large-slope areas have less available water. The positive correlation between topographic feature TWI and *ΔNDMI* indicates that forests in higher-TWI areas tend to have smaller moisture loss. Larger soil-water-holding capacity also contributes to smaller moisture loss. For subsurface features, areas with larger subsurface porosity and permeability tended to show less water stress.

Across all 21 static features, the historical *Min. P–ET* is the one feature that showed consistent strong correlations (r>0.7) with *Cum. P–ET* and positive correlations with Δ*NDMI* inside groves during the three droughts (Figure 12). Historical *Min. P–ET* was related (|r|>0.3) to elevation-dependent features (e.g. P_m, T_m, and SWE), and negatively correlated (r<0.7) to vegetation features ($NDVI_m$ and CanPct). Historical *Min. P–ET* correlated best (r=0.91) with the *Cum. P–ET* during the 2012-15 drought, followed by the 12-yr scenario (r=0.81) and 1987-92 drought (r=0.65) (Figure S19). The projected Δ*NDMI* during the 2012-15 drought also showed a good correlation (r=0.53) with the historical *Min. P–ET*. Meanwhile, as noted above, the historical *Min. P–ET*

dominates *ET* prediction in the LSTM model (Figures 8 and S14). Further, at a larger scale e.g. entire study domain (Figure S20), static-feature *Min. P–ET* explained 32% (29%) of the variance of Δ*NDMI* (ADS dead trees) during the 2012-15 drought, suggesting prominent tree-die-off and moisture-loss patterns when *Min. P–ET* ≤–149 mm. Collectively, the historical *Min. P–ET* can serve as a simple but important water-balance-based indicator for water stress that may occur during multi-year droughts, representing drought vulnerability in dense forests with high *ET* like giant-sequoia groves.

The median of historical *Min. P–ET* decreased monotonically along with elevation groups for high to low, with a 100-mm difference between high and low groves (Figure 13a), again indicating that areas in lower groves tend to show more water stress during droughts. Fifty percent of entire grove areas, indicated by the relative width of boxes in Figure 13a, are in medium-elevation groves, showing a median of *Min. P–ET* in between those of high and low elevation. Median values of *Min. P–ET* showed no apparent difference across grove groups classified by size (Figure 13b), consistent with the fact that there were no apparent differences in LAI (Figure S3c) and compositions of tree size and dense tree cover (Figures S21c,d), though small groves consisted of a relatively smaller portion of conifer mixed with giant sequoia (Figures S21a,b). In terms of nine elevation-size groups (Figure 13c), the median of *Min. P–ET* in high-elevation groves decreased monotonically from large (HL) to small (HS) groves. There was no monotonical trend of *Min. P–ET* median along with grove size for medium-elevation groups (ML, MM, and MS) and low-elevation groups (LL, LM, and LS). In general, *Min. P–ET* showed noticeable differences across groves grouped by elevation, but not for groves grouped by area. Also, from an assessment across 78 groves (Figure S22), *Min. P–ET* is positively correlated to elevation (Spearman correlation ρ=0.22), and reveals an increasing trend (a positive regression slope with insignificant p-value=0.058) from lowest to highest groves.

4 Discussion

4.1 Drought indicators

Our findings show that influences of multi-year droughts on Mediterranean-climate high-*ET* forests, including giant-sequoia groves and other forested areas in the Sierra Nevada, can be represented using water-balance-based indicators, e.g. the static-feature historical *Min. P–ET* and drought-dependent *Cum. P–ET*. Both indicators are important for predicting and assessing vegetation response to drought. As *Cum. P–ET* approaches or becomes more negative than *Min. P–ET*, forest dryness increases (decline in *NDMI*), and *NDVI* is more likely to decrease due to factors that include drought-induced die-off, fire, and beetle attack, The resulting feedback, reflected by a reduction in actual annual *ET* (e.g. indicated by Landsat-observed *NDVI*), should limit further declines in *Cum. P–ET* and enable values of the index to more quickly return to positive values when drought conditions give way to wetter conditions.

The indicator *Cum. P–ET* reflects the relative depletion of subsurface root-accessible storage available to support evapotranspiration when annual *P–ET* is negative, which was investigated using direct observations of subsurface moisture in previous studies (Bales et al., 2018; Goulden and Bales, 2019; O'Geen et al., 2018). The indicator *Min. P–ET* is an indicator of the lowest value that can support the expected *ET* of the forest, estimated from previous droughts. Thus *Cum. P–ET* explicitly accounts for vegetation response, which is not represented by other water-stress-relevant metrics calculated with temperature or other climate inputs, e.g. climatic water deficit and vapor pressure deficit (Koontz et al., 2021; Restaino et al., 2016; Young et al., 2017). Both historical *Min. P–ET* and *Cum. P–ET* correlate well with canopy moisture loss (Δ*NDMI*) in growing seasons, providing an additional view to plant water status during multi-year droughts. Since water-stress-prone areas in historical droughts tend to encounter severe reductions of *ET* and water deficit in more-extreme drought scenarios, the static-feature historical *Min. P–ET* at a 30-m resolution is a valuable indicator to map drought vulnerability.

Cumulative *P–ET* thus provides a realistic expression of the relation between water supply and demand during the early stage of a multi-year drought, representing moisture overdraft from subsurface water (Fellows and Goulden, 2017; Goulden and Bales, 2019; Klos et al., 2018), which may be exhaustively depleted, causing tree die-off. However, during the later stages of a prolonged drought (e.g. 8- and 12-year scenarios), tree die-off reduces *ET* and *Cum. P–ET* will recover if annual *P–ET* becomes positive. That is, the additional feedback from vegetation *ET* response is less clearly indicated by *Cum. P–ET* during the later stage of a prolonged drought scenario, after severe die-off in response to depleted subsurface water.

4.2 Potential for water subsidies in high-ET forest

As our analysis does not consider the transfer of water between pixels, or subsurface flow from locally higher and steeper to lower and flatter areas, we discuss the possible role of water subsidies in supporting higher water consumption of bigger and denser trees inside giant-sequoia groves during dry periods, because vegetations shifts their water uptake to deeper soil and groundwater during drought (Brinkmann et al., 2019; Goulden and Bales, 2019; Miguez-Macho and Fan, 2021).

Water-holding-capacity-related topographic and subsurface attributes are important considerations when assessing drought vulnerability within groves, where subsurface water subsidies from outside areas are important for maintaining favorable soil moisture (Rundel, 1972; Weatherspoon, 1986). While subsurface mapping of grove areas would be ideal, lacking those data we consider the relation of topographic features (e.g. TWI and curvature) to potential subsidies of water draining from shallow soil and groundwater (Hoylman et al., 2019; Ray, 2016). Curvature is closely related to surface flow on hillslopes (Bogaart and Troch, 2006; Talebi et al., 2008), soil moisture (Famiglietti et al., 1998), and groundwater level (Rinderer et al., 2014); and

we included the upslope curvature (mean curvature of upslope contribution area; Freeman, 1991; Kadirhodjaev et al., 2018), with a positive value for upwardly convex surface and a negative value for concave surface. Note that TWI closely correlates to upslope curvature (Figure S23c; Rinderer et al., 2014). The groves showed relatively higher TWI and lower upslope curvature values than surrounding control areas (Figures S23a,b), both indicating that groves are located in areas with more available water from soil and saprock. Inside the groves, areas with lower upslope curvature tended to have higher canopy coverage, thus higher *ET* and lower *Cum. P–ET* during drought (Figure S23c). However, these areas tended to lose less canopy moisture during drought, reflecting possible water subsidies from higher elevations supporting their water demand. Though the correlations between the two topographic features and *Cum. P–ET* and moisture loss are not strong (|r| of 0.1-0.2) at the 30-m pixel resolution, these findings do not rule out TWI and curvature being important predictors of additional water sources other than precipitation (Famiglietti et al., 1998; Huang et al., 2016; Rinderer et al., 2014).

Our results also suggested that steeper-slope areas tended to have more water stress, reflecting reduced water availability, as shown by soil-moisture survey data in the Teakettle Experimental Forest within our study domain (Figure S24; Kirchner et al., 2008; North et al., 2005). This is consistent with the high giant-sequoia foliage dieback observed on steep slopes during the 2012-15 drought (Stephenson et al., 2018). However, we also observed that other soil and subsurface properties (e.g. available soil-water holding capacity, subsurface porosity, and permeability) are linked to water stress or moisture loss during multi-year droughts, suggesting that the amount and ease of subsurface flow affect local water availability.

Trees show greater vulnerability when having limited water supply from deep roots (Hember et al., 2017; Hubbert et al., 2001). During the WY2012-15 dry period, measurements over WY2015 showed that root-accessible water was depleted down to a depth of at least 10 m at Providence, a 2100-m elevation mixed-conifer research site (37°3.120’ N, 119°12.196’ W) within the study domain of the giant-sequoia groves (O’Geen et al., 2018). The limited winter precipitation only recharged the upper meter, which was depleted by shallow roots through the growing season (Bales et al., 2018). An important question is whether downslope flow to high-TWI areas could provide subsidies to deeper roots, versus shallower roots. Given the relatively fast recession of the top layer of soil moisture in the southern Sierra Nevada (Oroza et al., 2018), subsidies would need to be in areas where there was either deep recharge or areas with higher *Cum. P–ET* that had deeper surplus water during droughts. Thus, while we cannot rule out upslope subsidies to giant-sequoia trees, current soil and hydrologic data do not support that. Expanding the spatial and vertical coverages of soil-moisture monitoring network across different grove landscapes, such as using the wireless-sensor technology (Oroza et al., 2018; Zhang et al., 2017), could provide more details about the subsurface water flow, and thus help improve the understanding of water availability and distribution across groves. Seismic surveys could also provide insights into wetter versus drier positions on a hillslope (Callahan et al., 2020; Klos et al., 2018).

The proposed water-stress indicator, historical *Min. P–ET*, can also be considered as the dependence on available water from deep soil (Fellows and Goulden, 2017; O’Geen et al., 2018) and subsurface subsidies (Love et al., 2019; Rundel, 1972). It indicates the limit of additional subsurface water that can be extracted to support plant *ET* demand during multi-year dry conditions. Lower historical *Min. P–ET* means that plants rely on a larger water supply from subsurface storage, whereas during the prolonged-year droughts, depleted subsurface water cannot support these plants, leading to more-severe moisture loss and similar water-stress response shown during historical droughts.

4.3 Implication for forest drought management

For drought management in dense Mediterranean forests, it is important to know the location and severity of water stress. With water-balance-based indicators, we specifically investigated water-stress patterns across giant-sequoia groves during multi-year droughts, since the endangered world’s largest trees prefer a moist environment with abundant soil moisture (DeSilva and Dodd, 2020), and their growth is highly sensitive to water availability (York et al., 2003). Lower-elevation groves tend to show larger water stress during multi-year droughts than higher-elevation groves, consistent with field observations of giant-sequoia dieback (Stephenson et al., 2018) and widespread mortality observed in lower elevations of the Sierra Nevada (Brodrick et al., 2019). This is explained by the higher tree density (with larger LAI) in low elevations consuming more water (higher *ET*) along with relatively smaller precipitation than in higher elevations. However, we did not find an apparent difference in water-stress patterns across groves with contrasting sizes, consistent with the fact that there are no apparent differences in LAI and compositions of tree size and tree canopy cover across the groves grouped by size. This implies that vegetation grows well, benefiting from abundant soil moisture inside different-size groves with stable boundaries (Rundel, 1972; Weatherspoon, 1986). Our findings suggest that lower-elevation groves with more-severe water stress response shown in historical droughts should have a high conservation priority, in preparation for more-extreme megadroughts in a warming climate (Williams et al., 2020).

5 Conclusions

Using water-balance indicators this study assessed multi-year-drought vulnerability in mountain forests by taking giant-sequoia groves as a high-*ET* example. Two water-balance indicators, i.e. cumulative *P–ET* during an individual drought and historical minimum *P–ET*, are closely related to canopy moisture loss and tree mortality, reflecting drought vulnerability. The three hypotheses posed in this study are supported with water-balance investigations of long-term records in historical droughts and model projections for extreme-drought scenarios. First, the Earth’s largest tree giant sequoia grows in mixed-conifer groves with relatively higher

tree density and size than surrounding forests, contributing to higher *ET* inside groves and thus more-severe water stress (more-negative cumulative *P–ET*). Second, inside high-*ET*-grove forests, lower elevation areas tend to show more-severe water stress than high elevations, due to lower *P* and higher *ET* from their denser tree canopy. Third, water stress shows historical similarity, that is, water-stress-prone areas in historical droughts tend to again suffer water stress in more-extreme droughts. This is evidenced by comparing water-balance indicators during the historical 1987-92 and 2012-15 droughts, and extreme-drought scenarios. This historical similarity of water stress is also supported by the fact that historical-minimum *P–ET* can indicate water stress during multi-year droughts. Minimum *P–ET* represents relative dependence on additional water sources other than precipitation, including stored subsurface water and melted snow, which may be insufficient during a prolonged multi-year drought, especially in overstocked forests, such as found in California's southern Sierra Nevada. Our study provides water-balance-based indicators as a convenient tool for assessing forest-drought vulnerability in a warming climate. These indicators are particularly relevant for forests that rely heavily on subsurface-stored water to maintain a large fraction of *ET* demand during seasonally and multi-year dry periods found in the Mediterranean climate.

Acknowledgments

This research was supported by the NSF Southern Sierra Critical Zone Observatory (EAR-1331939), the UC Water Security and Sustainability Research Initiative grant No. 13941, the U.S. Bureau of Reclamation WaterSMART Program (Sustain and Manage America's Resources for Tomorrow), and the California Department of Water Resources. The authors acknowledge high-performance computing support from the MERCED cluster.

Supporting Information

The Supporting Information for this article can be found below.

References

Adams, H.D., Guardiola-Claramonte, M., Barron-Gafford, G.A., Villegas, J.C., Breshears, D.D., Zou, C.B., Troch, P.A., Huxman, T.E., 2009. Temperature sensitivity of drought-induced tree mortality portends increased regional die-off under global-change-type drought. Proc. Natl. Acad. Sci. U. S. A. 106, 7063–7066. https://doi.org/10.1073/pnas.0901438106

Adams, H.D., Macalady, A.K., Breshears, D.D., Allen, C.D., Stephenson, N.L., Saleska, S.R., Huxman, T.E., McDowell, N. g., 2010. Climate-Induced Tree Mortality: Earth System Consequences. Eos, Trans. Am. Geophys. Union 91, 153. https://doi.org/10.1029/2010EO170003

Allen, C.D., Breshears, D.D., McDowell, N.G., 2015. On underestimation of global vulnerability to tree mortality and forest die-off from hotter drought in the Anthropocene. Ecosphere 6, 1–55. https://doi.org/10.1890/ES15-00203.1

Allen, C.D., Macalady, A.K., Chenchouni, H., Bachelet, D., McDowell, N., Vennetier, M., Kitzberger, T., Rigling, A., Breshears, D.D., Hogg, E.H., Gonzalez, P., Fensham, R., Zhang, Z., Castro, J., Demidova, N., Lim, J.H., Allard, G., Running, S.W., Semerci, A., Cobb, N., 2010. A global overview of drought and heat-induced tree mortality reveals emerging climate change risks for forests. For. Ecol. Manage. 259, 660–684. https://doi.org/10.1016/j.foreco.2009.09.001

Ambrose, A.R., Baxter, W.L., Martin, R.E., Francis, E., Asner, G.P., Nydick, K.R., Dawson, T.E., 2018. Leaf- and crown-level adjustments help giant sequoias maintain favorable water status during severe drought. For. Ecol. Manage. 419–420, 257–267. https://doi.org/10.1016/j.foreco.2018.01.012

Ambrose, A.R., Baxter, W.L., Wong, C.S., Burgess, S.S.O., Williams, C.B., Næsborg, R.R., Koch, G.W., Dawson, T.E., 2016. Hydraulic constraints modify optimal photosynthetic profiles in giant sequoia trees. Oecologia 182, 713–730. https://doi.org/10.1007/s00442-016-3705-3

Anderegg, W.R.L., Anderegg, L.D.L., Kerr, K.L., Trugman, A.T., 2019. Widespread drought-induced tree mortality at dry range edges indicates that climate stress exceeds species' compensating mechanisms. Glob. Chang. Biol. 25, 3793–3802. https://doi.org/10.1111/gcb.14771

Anderegg, W.R.L., Klein, T., Bartlett, M., Sack, L., Pellegrini, A.F.A., Choat, B., Jansen, S., 2016. Meta-analysis reveals that hydraulic traits explain cross-species patterns of drought-induced tree mortality across the globe. Proc. Natl. Acad. Sci. U. S. A. 113, 5024–5029. https://doi.org/10.1073/pnas.1525678113

Aparecido, L.M.T., Miller, G.R., Cahill, A.T., Moore, G.W., 2016. Comparison of tree transpiration under wet and dry canopy conditions in a Costa Rican premontane tropical forest. Hydrol. Process. 30, 5000–5011. https://doi.org/10.1002/hyp.10960

Arend, M., Link, R.M., Patthey, R., Hoch, G., Schuldt, B., Kahmen, A., 2021. Rapid hydraulic collapse as cause of drought-induced mortality in conifers. Proc. Natl. Acad. Sci. 118, e2025251118. https://doi.org/10.1073/pnas.2025251118

Asner, G.P., Brodrick, P.G., Anderson, C.B., Vaughn, N., Knapp, D.E., Martin, R.E., 2016. Progressive forest canopy water loss during the 2012-2015 California drought. Proc. Natl. Acad. Sci. U. S. A. 113, E249–E255. https://doi.org/10.1073/pnas.1523397113

Bales, R.C., Goulden, M.L., Hunsaker, C.T., Conklin, M.H., Hartsough, P.C., O'Geen, A.T., Hopmans, J.W., Safeeq, M., 2018. Mechanisms controlling the impact of multi-year drought on mountain hydrology. Sci. Rep. 8, 690. https://doi.org/10.1038/s41598-017-19007-0

Batllori, E., Lloret, F., Aakala, T., Anderegg, W.R.L., Aynekulu, E., Bendixsen, D.P., Bentouati, A., Bigler, C., Burk, C.J., Camarero, J.J., Colangelo, M., Coop, J.D., Fensham, R., Floyd, M.L., Galiano, L., Ganey, J.L., Gonzalez, P., Jacobsen, A.L., Kane, J.M., Kitzberger, T., Linares, J.C., Marchetti, S.B., Matusick, G., Michaelia, M., Navarro-Cerrillo, R.M., Pratt, R.B., Redmond, M.D., Rigling, A., Ripullone, F., Sangüesa-Barreda, G., Sasal, Y., Saura-Mas, S., Suarez, M.L., Veblen, T.T., Vilà-Cabrera, A., Vincke, C., Zeeman, B., 2020. Forest and woodland replacement patterns following drought-related mortality. Proc. Natl. Acad. Sci. U. S. A. 117, 29720–29729. https://doi.org/10.1073/pnas.2002314117

Batunacun, Wieland, R., Lakes, T., Nendel, C., 2021. Using Shapley additive explanations to interpret extreme gradient boosting predictions of grassland degradation in Xilingol, China. Geosci. Model Dev. 14, 1493–1510. https://doi.org/10.5194/gmd-14-1493-2021

Biederman, J.A., Harpold, A.A., Gochis, D.J., Ewers, B.E., Reed, D.E., Papuga, S.A., Brooks, P.D., 2014. Increased evaporation

following widespread tree mortality limits streamflow response. Water Resour. Res. 50, 5395–5409. https://doi.org/10.1002/2013WR014994

Bogaart, P.W., Troch, P.A., 2006. Curvature distribution within hillslopes and catchments and its effect on the hydrological response. Hydrol. Earth Syst. Sci. 10, 925–936. https://doi.org/10.5194/hess-10-925-2006

Brinkmann, N., Eugster, W., Buchmann, N., Kahmen, A., 2019. Species-specific differences in water uptake depth of mature temperate trees vary with water availability in the soil. Plant Biol. 21, 71–81. https://doi.org/10.1111/plb.12907

Brodrick, P.G., Anderegg, L.D.L., Asner, G.P., 2019. Forest Drought Resistance at Large Geographic Scales. Geophys. Res. Lett. 46, 2752–2760. https://doi.org/10.1029/2018GL081108

Brodrick, P.G., Asner, G.P., 2017. Remotely sensed predictors of conifer tree mortality during severe drought. Environ. Res. Lett. 12. https://doi.org/10.1088/1748-9326/aa8f55

Byer, S., Jin, Y., 2017. Detecting drought-induced tree mortality in Sierra Nevada forests with time series of satellite data. Remote Sens. 9, 14–17. https://doi.org/10.3390/rs9090929

Callahan, R.P., Riebe, C.S., Pasquet, S., Ferrier, K.L., Grana, D., Sklar, L.S., Taylor, N.J., Flinchum, B.A., Hayes, J.L., Carr, B.J., Hartsough, P.C., O'Geen, A.T., Holbrook, W.S., 2020. Subsurface Weathering Revealed in Hillslope-Integrated Porosity Distributions. Geophys. Res. Lett. 47, 1–10. https://doi.org/10.1029/2020GL088322

Carlson, T.N., Ripley, D.A., 1997. On the relation between NDVI, fractional vegetation cover, and leaf area index. Remote Sens. Environ. 62, 241–252. https://doi.org/10.1016/S0034-4257(97)00104-1

Chen, J., Dafflon, B., Tran, A.P., Falco, N., Hubbard, S., 2020. A Deep-Learning Hybrid-Predictive-Modeling Approach for Estimating Evapotranspiration and Ecosystem Respiration. Hydrol. Earth Syst. Sci. Discuss. 1–38. https://doi.org/10.5194/hess-2020-322

Chen, J.M., Rich, P.M., Gower, S.T., Norman, J.M., Plummer, S., 1997. Leaf area index of boreal forests: Theory, techniques, and measurements. J. Geophys. Res. Atmos. 102, 29429–29443. https://doi.org/10.1029/97jd01107

Chen, Z., Zhu, Z., Jiang, H., Sun, S., 2020. Estimating daily reference evapotranspiration based on limited meteorological data using deep learning and classical machine learning methods. J. Hydrol. 591, 125286. https://doi.org/10.1016/j.jhydrol.2020.125286

Christiansen, E.L., 1975. A comparative study of tree structure and composition of a mixed coniferous forest and sequoia groves in Sequoia National Park, California.

Claverie, M., Vermote, E.F., Franch, B., Masek, J.G., 2015. Evaluation of the Landsat-5 TM and Landsat-7 ETM+ surface reflectance products. Remote Sens. Environ. 169, 390–403. https://doi.org/10.1016/j.rse.2015.08.030

Daly, C., Halbleib, M., Smith, J.I., Gibson, W.P., Doggett, M.K., Taylor, G.H., Curtis, J., Pasteris, P.P., 2008. Physiographically sensitive mapping of climatological temperature and precipitation across the conterminous United States. Int. J. Climatol. 28, 2031–2064. https://doi.org/10.1002/joc.1688

Daly, C., Neilson, R.P., Phillips, D.L., 1994. A Statistical-Topographic Model for Mapping Climatological Precipitation over Mountainous Terrain. J. Appl. Meteorol. 33, 140–158. https://doi.org/10.1175/1520-0450(1994)033<0140:ASTMFM>2.0.CO;2

Dawson, T.E., 1996. Determining water use by trees and forests from isotopic, energy balance and transpiration analyses: The roles of tree size and hydraulic lift. Tree Physiol. 16, 263–272. https://doi.org/10.1093/treephys/16.1-2.263

DeSilva, R., Dodd, R.S., 2020. Association of genetic and climatic variability in giant sequoia, Sequoiadendron giganteum, reveals signatures of local adaptation along moisture-related gradients. Ecol. Evol. 10, 10619–10632. https://doi.org/10.1002/ece3.6716

Famiglietti, J.S., Rudnicki, J.W., Rodell, M., 1998. Variability in surface moisture content along a hillslope transect: Rattlesnake Hill, Texas. J. Hydrol. 210, 259–281. https://doi.org/10.1016/S0022-1694(98)00187-5

Farr, T.G., Rosen, P.A., Caro, E., Crippen, R., Duren, R., Hensley, S., Kobrick, M., Paller, M., Rodriguez, E., Roth, L., Seal, D., Shaffer, S., Shimada, J., Umland, J., Werner, M., Oskin, M., Burbank, D., Alsdorf, D., 2007. The Shuttle Radar Topography Mission. Rev. Geophys. 45, RG2004. https://doi.org/10.1029/2005RG000183

Fellows, A.W., Goulden, M.L., 2017. Mapping and understanding dry season soil water drawdown by California montane vegetation. Ecohydrology 10, 1–12. https://doi.org/10.1002/eco.1772

Flint, L.E., Flint, A.L., Mendoza, J., Kalansky, J., Ralph, F.M., 2018. Characterizing drought in California: new drought indices and scenario-testing in support of resource management. Ecol. Process. 7, 1–13. https://doi.org/10.1186/s13717-017-0112-6

Freeman, T.G., 1991. Calculating catchment area with divergent flow based on a regular grid. Comput. Geosci. 17, 413–422. https://doi.org/10.1016/0098-3004(91)90048-I

Furniss, T.J., Kane, V.R., Larson, A.J., Lutz, J.A., 2020. Detecting tree mortality with Landsat-derived spectral indices: Improving ecological accuracy by examining uncertainty. Remote Sens. Environ. 237, 111497. https://doi.org/10.1016/j.rse.2019.111497

Gauch, M., Kratzert, F., Klotz, D., Nearing, G., Lin, J., Hochreiter, S., 2021. Rainfall–runoff prediction at multiple timescales with a single Long Short-Term Memory network. Hydrol. Earth Syst. Sci. 25, 2045–2062. https://doi.org/10.5194/hess-25-2045-2021

Gleeson, T., Moosdorf, N., Hartmann, J., van Beek, L.P.H., 2014. A glimpse beneath earth's surface: GLobal HYdrogeology MaPS (GLHYMPS) of permeability and porosity. Geophys. Res. Lett. 41, 3891–3898. https://doi.org/10.1002/2014GL059856

Goodwin, N.R., Coops, N.C., Wulder, M.A., Gillanders, S., Schroeder, T.A., Nelson, T., 2008. Estimation of insect infestation dynamics using a temporal sequence of Landsat data. Remote Sens. Environ. 112, 3680–3689. https://doi.org/10.1016/j.rse.2008.05.005

Gorelick, N., Hancher, M., Dixon, M., Ilyushchenko, S., Thau, D., Moore, R., 2017. Google Earth Engine: Planetary-scale geospatial analysis for everyone. Remote Sens. Environ. 202, 18–27. https://doi.org/10.1016/j.rse.2017.06.031

Goulden, M.L., Anderson, R.G., Bales, R.C., Kelly, A.E., Meadows, M., Winston, G.C., 2012. Evapotranspiration along an elevation gradient in California's Sierra Nevada. J. Geophys. Res. Biogeosciences 117, 1–13. https://doi.org/10.1029/2012JG002027

Goulden, M.L., Bales, R.C., 2019. California forest die-off linked to multi-year deep soil drying in 2012–2015 drought. Nat. Geosci. 12, 632–637. https://doi.org/10.1038/s41561-019-0388-5

Goulden, M.L., Bales, R.C., 2014. Mountain runoff vulnerability to increased evapotranspiration with vegetation expansion. Proc.

Natl. Acad. Sci. U. S. A. 111, 14071–14075. https://doi.org/10.1073/pnas.1319316111

Granata, F., Di Nunno, F., 2021. Forecasting evapotranspiration in different climates using ensembles of recurrent neural networks. Agric. Water Manag. 255, 107040. https://doi.org/10.1016/j.agwat.2021.107040

Guo, Q., Zhou, Y., Ray, R., Bales, R., 2013. Vulnerability of Giant Sequoia to Moisture Stress in a Changing Climate: A pilot study of potential moisture proxies. Three Rivers, CA.

Hartesveldt, R.J., Harvey, H.T., Shellhammer, H.S., Stecker, R.E., 1975. The giant sequoia of the Sierra Nevada. Department of the Interior, National Park Service, Washington, DC.

Hember, R.A., Kurz, W.A., Coops, N.C., 2017. Relationships between individual-tree mortality and water-balance variables indicate positive trends in water stress-induced tree mortality across North America. Glob. Chang. Biol. 23, 1691–1710. https://doi.org/10.1111/gcb.13428

Hochreiter, S., Schmidhuber, J., 1997. Long Short-Term Memory. Neural Comput. 9, 1735–1780. https://doi.org/10.1162/neco.1997.9.8.1735

Hoylman, Z.H., Jencso, K.G., Hu, J., Holden, Z.A., Martin, J.T., Gardner, W.P., 2019. The climatic water balance and topography control spatial patterns of atmospheric demand, soil moisture, and shallow subsurface flow. Water Resour. Res. 55, 2370–2389. https://doi.org/10.1029/2018WR023302

Huang, H., Chen, Y., Clinton, N., Wang, J., Wang, X., Liu, C., Gong, P., Yang, J., Bai, Y., Zheng, Y., Zhu, Z., 2017. Mapping major land cover dynamics in Beijing using all Landsat images in Google Earth Engine. Remote Sens. Environ. 202, 166–176. https://doi.org/10.1016/j.rse.2017.02.021

Huang, X., Shi, Z.H., Zhu, H.D., Zhang, H.Y., Ai, L., Yin, W., 2016. Soil moisture dynamics within soil profiles and associated environmental controls. Catena 136, 189–196. https://doi.org/10.1016/j.catena.2015.01.014

Hubbert, K.R., Beyers, J.L., Graham, R.C., 2001. Roles of weathered bedrock and soil in seasonal water relations of Pinus jeffreyi and Arctostaphylos patula. Can. J. For. Res. 31, 1947–1957. https://doi.org/10.1139/cjfr-31-11-1947

Jin, S., Su, Y., Gao, S., Hu, T., Liu, J., Guo, Q., 2018. The transferability of Random Forest in canopy height estimation from multi-source remote sensing data. Remote Sens. 10, 1–21. https://doi.org/10.3390/rs10081183

Kadirhodjaev, A., Kadavi, P.R., Lee, C.W., Lee, S., 2018. Analysis of the relationships between topographic factors and landslide occurrence and their application to landslide susceptibility mapping: a case study of Mingchukur, Uzbekistan. Geosci. J. 22, 1053–1067. https://doi.org/10.1007/s12303-018-0052-x

Kirchner, P.B., Bales, R.C., North, M.P., Small, E.E., 2008. Snowmelt infiltration and evapotranspiration in Red Fir forest ecosystems of the Sierra Nevada, in: AGU Fall Meeting Abstracts. pp. C21C-0572.

Klos, P.Z., Goulden, M.L., Riebe, C.S., Tague, C.L., O'Geen, A.T., Flinchum, B.A., Safeeq, M., Conklin, M.H., Hart, S.C., Berhe, A.A., Hartsough, P.C., Holbrook, W.S., Bales, R.C., 2018. Subsurface plant-accessible water in mountain ecosystems with a Mediterranean climate. Wiley Interdiscip. Rev. Water 5, e1277. https://doi.org/10.1002/wat2.1277

Koontz, M.J., Latimer, A.M., Mortenson, L.A., Fettig, C.J., North, M.P., 2021. Cross-scale interaction of host tree size and climatic water deficit governs bark beetle-induced tree mortality. Nat. Commun. 12, 1–13. https://doi.org/10.1038/s41467-020-20455-y

Kraft, B., Jung, M., Körner, M., Requena Mesa, C., Cortés, J., Reichstein, M., 2019. Identifying dynamic memory effects on vegetation state using Recurrent Neural Networks. Front. Big Data 2. https://doi.org/10.3389/fdata.2019.00031

Kratzert, F., Klotz, D., Herrnegger, M., Sampson, A.K., Hochreiter, S., Nearing, G.S., 2019. Toward improved predictions in ungauged basins: Exploiting the power of machine learning. Water Resour. Res. 55, 11344–11354. https://doi.org/10.1029/2019WR026065

Lany, N.K., Zarnetske, P.L., Finley, A.O., McCullough, D.G., 2020. Complementary strengths of spatially-explicit and multi-species distribution models. Ecography (Cop.). 43, 456–466. https://doi.org/10.1111/ecog.04728

Liu, Y., Kumar, M., Katul, G.G., Porporato, A., 2019. Reduced resilience as an early warning signal of forest mortality. Nat. Clim. Chang. 9, 880–885. https://doi.org/10.1038/s41558-019-0583-9

Love, D.M., Venturas, M.D., Sperry, J.S., Brooks, P.D., Pettit, J.L., Wang, Y., Anderegg, W.R.L., Tai, X., Mackay, D.S., 2019. Dependence of Aspen Stands on a Subsurface Water Subsidy: Implications for Climate Change Impacts. Water Resour. Res. 55, 1833–1848. https://doi.org/10.1029/2018WR023468

Lundberg, S., Lee, S.-I., 2017. A Unified Approach to Interpreting Model Predictions. Adv. Neural Inf. Process. Syst. 4766–4775.

Ma, Q., Bales, R.C., Rungee, J., Conklin, M.H., Collins, B.M., Goulden, M.L., 2020. Wildfire controls on evapotranspiration in California's Sierra Nevada. J. Hydrol. 590, 125364. https://doi.org/10.1016/j.jhydrol.2020.125364

Mann, M.E., Gleick, P.H., 2015. Climate change and California drought in the 21st century. Proc. Natl. Acad. Sci. U. S. A. 112, 3858–3859. https://doi.org/10.1073/pnas.1503667112

Margulis, S.A., Cortés, G., Girotto, M., Durand, M., 2016. A Landsat-era Sierra Nevada snow reanalysis (1985–2015). J. Hydrometeorol. 17, 1203–1221. https://doi.org/10.1175/JHM-D-15-0177.1

Martin, R.E., Asner, G.P., Francis, E., Ambrose, A., Baxter, W., Das, A.J., Vaughn, N.R., Paz-Kagan, T., Dawson, T., Nydick, K., Stephenson, N.L., 2018. Remote measurement of canopy water content in giant sequoias (Sequoiadendron giganteum) during drought. For. Ecol. Manage. 419–420, 279–290. https://doi.org/10.1016/j.foreco.2017.12.002

Masek, J.G., Vermote, E.F., Saleous, N.E., Wolfe, R., Hall, F.G., Huemmrich, K.F., Gao, F., Kutler, J., Lim, T.K., 2006. A landsat surface reflectance dataset for North America, 1990-2000. IEEE Geosci. Remote Sens. Lett. 3, 68–72. https://doi.org/10.1109/LGRS.2005.857030

Maurer, T., 2021. Drivers of drought-induced shifts in the water balance through a Budyko approach. Hydrol. Earth Syst. Sci. Discuss. https://doi.org/10.5194/hess-2021-55

McDowell, N.G., Allen, C.D., 2015. Darcy's law predicts widespread forest mortality under climate warming. Nat. Clim. Chang. 5, 669–672. https://doi.org/10.1038/nclimate2641

McLaughlin, B.C., Ackerly, D.D., Klos, P.Z., Natali, J., Dawson, T.E., Thompson, S.E., 2017. Hydrologic refugia, plants, and climate change. Glob. Chang. Biol. 23, 2941–2961. https://doi.org/10.1111/gcb.13629

Meddens, A.J.H., Hicke, J.A., Vierling, L.A., Hudak, A.T., 2013. Evaluating methods to detect bark beetle-caused tree mortality using single-date and multi-date Landsat imagery. Remote Sens.

Environ. 132, 49–58. https://doi.org/10.1016/j.rse.2013.01.002

Meyer, M.D., Safford, H.D., 2011. Giant sequoia regeneration in groves exposed to wildfire and retention harvest. Fire Ecol. 7, 2–16. https://doi.org/10.4996/fireecology.0702002

Miguez-Macho, G., Fan, Y., 2021. Spatiotemporal origin of soil water taken up by vegetation. Nature 598, 624–628. https://doi.org/10.1038/s41586-021-03958-6

Moravec, V., Markonis, Y., Rakovec, O., Svoboda, M., Trnka, M., Kumar, R., Hanel, M., 2021. Europe under multi-year droughts: How severe was the 2014–2018 drought period? Environ. Res. Lett. 16. https://doi.org/10.1088/1748-9326/abe828

Myneni, R.B., Hoffman, S., Knyazikhin, Y., Privette, J.L., Glassy, J., Tian, Y., Wang, Y., Song, X., Zhang, Y., Smith, G.R., Lotsch, A., Friedl, M., Morisette, J.T., Votava, P., Nemani, R.R., Running, S.W., 2002. Global products of vegetation leaf area and fraction absorbed PAR from year one of MODIS data. Remote Sens. Environ. 83, 214–231. https://doi.org/10.1016/S0034-4257(02)00074-3

North, M., Oakley, B., Fiegener, R., Gray, A., Barbour, M., 2005. Influence of light and soil moisture on Sierran mixed-conifer understory communities. Plant Ecol. 177, 13–24. https://doi.org/10.1007/s11258-005-2270-3

Nydick, K.R., Stephenson, N.L., Ambrose, A.R., Asner, G.P., Baxter, W.L., Das, A.J., Dawson, T., Martin, R.E., Paz-Kagan, T., 2018. Leaf to landscape responses of giant sequoia to hotter drought: An introduction and synthesis for the special section. For. Ecol. Manage. 419–420, 249–256. https://doi.org/10.1016/j.foreco.2018.03.028

O'Geen, A.T., Safeeq, M., Wagenbrenner, J., Stacy, E., Hartsough, P., Devine, S., Tian, Z., Ferrell, R., Goulden, M., Hopmans, J.W., Bales, R., 2018. Southern Sierra Critical Zone Observatory and Kings River Experimental Watersheds: A synthesis of measurements, new insights, and future directions. Vadose Zo. J. 17, 180081. https://doi.org/10.2136/vzj2018.04.0081

Ogle, K., Barber, J.J., Barron-Gafford, G.A., Bentley, L.P., Young, J.M., Huxman, T.E., Loik, M.E., Tissue, D.T., 2015. Quantifying ecological memory in plant and ecosystem processes. Ecol. Lett. 18, 221–235. https://doi.org/10.1111/ele.12399

Olson, M.E., Soriano, D., Rosell, J.A., Anfodillo, T., Donoghue, M.J., Edwards, E.J., León-Gómez, C., Dawson, T., Julio Camarero Martínez, J., Castorena, M., Echeverría, A., Espinosa, C.I., Fajardo, A., Gazol, A., Isnard, S., Lima, R.S., Marcati, C.R., Méndez-Alonzo, R., 2018. Plant height and hydraulic vulnerability to drought and cold. Proc. Natl. Acad. Sci. U. S. A. 115, 7551–7556. https://doi.org/10.1073/pnas.1721728115

Oroza, C.A., Bales, R.C., Stacy, E.M., Zheng, Z., Glaser, S.D., 2018. Long-Term Variability of Soil Moisture in the Southern Sierra: Measurement and Prediction. Vadose Zo. J. 17, 1–9. https://doi.org/10.2136/vzj2017.10.0178

Papagiannopoulou, C., Miralles, Di.G., Decubber, S., Demuzere, M., Verhoest, N.E.C., Dorigo, W.A., Waegeman, W., 2017. A non-linear Granger-causality framework to investigate climate-vegetation dynamics. Geosci. Model Dev. 10, 1945–1960. https://doi.org/10.5194/gmd-10-1945-2017

Parker, G.G., 2020. Tamm review: Leaf Area Index (LAI) is both a determinant and a consequence of important processes in vegetation canopies. For. Ecol. Manage. 477. https://doi.org/10.1016/j.foreco.2020.118496

Paz-Kagan, T., Vaughn, N.R., Martin, R.E., Brodrick, P.G., Stephenson, N.L., Das, A.J., Nydick, K.R., Asner, G.P., 2018. Landscape-scale variation in canopy water content of giant sequoias during drought. For. Ecol. Manage. 419–420, 291–304. https://doi.org/10.1016/j.foreco.2017.11.018

Peduzzi, A., Wynne, R.H., Fox, T.R., Nelson, R.F., Thomas, V.A., 2012. Estimating leaf area index in intensively managed pine plantations using airborne laser scanner data. For. Ecol. Manage. 270, 54–65. https://doi.org/10.1016/j.foreco.2011.12.048

Pelletier, J.D., Broxton, P.D., Hazenberg, P., Zeng, X., Troch, P.A., Niu, G., Williams, Z., Brunke, M.A., Gochis, D., 2016. A gridded global data set of soil, intact regolith, and sedimentary deposit thicknesses for regional and global land surface modeling. J. Adv. Model. Earth Syst. 8, 41–65. https://doi.org/10.1002/2015MS000526

Ray, R.L., 2016. Moisture Stress Indicators in Giant Sequoia Groves in the Southern Sierra Nevada of California, USA. Vadose Zo. J. 15, vzj2016.03.0018. https://doi.org/10.2136/vzj2016.03.0018

Reichstein, M., Camps-Valls, G., Stevens, B., Jung, M., Denzler, J., Carvalhais, N., Prabhat, 2019. Deep learning and process understanding for data-driven Earth system science. Nature 566, 195–204. https://doi.org/10.1038/s41586-019-0912-1

Restaino, C., Peterson, D.L., Littell, J., 2016. Increased water deficit decreases Douglas fir growth throughout western US forests. Proc. Natl. Acad. Sci. U. S. A. 113, 9557–9562. https://doi.org/10.1073/pnas.1602384113

Restaino, C., Young, D.J.N., Estes, B., Gross, S., Wuenschel, A., Meyer, M., Safford, H., 2019. Forest structure and climate mediate drought-induced tree mortality in forests of the Sierra Nevada, USA. Ecol. Appl. 29, 1–14. https://doi.org/10.1002/eap.1902

Rinderer, M., van Meerveld, H.J., Seibert, J., 2014. Topographic controls on shallow groundwater levels in a steep, prealpine catchment: When are the TWI assumptions valid? Water Resour. Res. 50, 6067–6080. https://doi.org/10.1002/2013WR015009

Roberts, L.J., Burnett, R., Tietz, J., Veloz, S., 2019. Recent drought and tree mortality effects on the avian community in southern Sierra Nevada: a glimpse of the future? Ecol. Appl. 29. https://doi.org/10.1002/eap.1848

Roche, J.W., Goulden, M.L., Bales, R.C., 2018. Estimating evapotranspiration change due to forest treatment and fire at the basin scale in the Sierra Nevada, California. Ecohydrology 11, 1–10. https://doi.org/10.1002/eco.1978

Roche, J.W., Ma, Q., Rungee, J., Bales, R.C., 2020. Evapotranspiration Mapping for Forest Management in California's Sierra Nevada. Front. For. Glob. Chang. 3, 69. https://doi.org/10.3389/ffgc.2020.00069

Rogers, B.M., Solvik, K., Hogg, E.H., Ju, J., Masek, J.G., Michaelian, M., Berner, L.T., Goetz, S.J., 2018. Detecting early warning signals of tree mortality in boreal North America using multiscale satellite data. Glob. Chang. Biol. 24, 2284–2304. https://doi.org/10.1111/gcb.14107

Rundel, P.W., 1972. Habitat Restriction in Giant Sequoia: The Environmental Control of Grove Boundaries. Am. Midl. Nat. 87, 81. https://doi.org/10.2307/2423883

Rundel, P.W., 1971. Community Structure and Stability in the Giant Sequoia Groves of the Sierra Nevada, California. Am. Midl. Nat. 85, 478. https://doi.org/10.2307/2423770

Saksa, P.C., Conklin, M.H., Battles, J.J., Tague, C.L., Bales, R.C., 2017. Forest thinning impacts on the water balance of Sierra Nevada mixed-conifer headwater basins. Water Resour. Res. 53, 5364–5381. https://doi.org/10.1002/2016WR019240

Sankey, T., Belmonte, A., Massey, R., Leonard, J., 2021. Regional-scale forest restoration effects on ecosystem resiliency to drought: a synthesis of vegetation and moisture trends on Google Earth Engine. Remote Sens. Ecol. Conserv. 7, 259–274. https://doi.org/10.1002/rse2.186

Schlesinger, W.H., Jasechko, S., 2014. Transpiration in the global water cycle. Agric. For. Meteorol. 189–190, 115–117. https://doi.org/10.1016/j.agrformet.2014.01.011

Scott, R.L., Knowles, J.F., Nelson, J.A., Gentine, P., Li, X., Barron-Gafford, G., Bryant, R., Biederman, J.A., 2021. Water availability impacts on evapotranspiration partitioning. Agric. For. Meteorol. 297, 108251. https://doi.org/10.1016/j.agrformet.2020.108251

Shen, C., Laloy, E., Elshorbagy, A., Albert, A., Bales, J., Chang, F.J., Ganguly, S., Hsu, K.L., Kifer, D., Fang, Z., Fang, K., Li, D., Li, X., Tsai, W.P., 2018. HESS Opinions: Incubating deep-learning-powered hydrologic science advances as a community. Hydrol. Earth Syst. Sci. 22, 5639–5656. https://doi.org/10.5194/hess-22-5639-2018

Simard, M., Pinto, N., Fisher, J.B., Baccini, A., 2011. Mapping forest canopy height globally with spaceborne lidar. J. Geophys. Res. Biogeosciences 116, 1–12. https://doi.org/10.1029/2011JG001708

Stephenson, N.L., 1999. Reference conditions for giant sequoia forest restoration: Structure, process, and precision. Ecol. Appl. 9, 1253–1265. https://doi.org/10.1890/1051-0761(1999)009[1253:RCFGSF]2.0.CO;2

Stephenson, N.L., 1996. Ecology and management of giant sequoia groves, Sierra Nevada Ecosystem Project: Final Report to Congress.

Stephenson, N.L., Brigham, C., 2021. Preliminary estimates of sequoia mortality in the 2020 Castle Fire 2021.

Stephenson, N.L., Das, A.J., Ampersee, N.J., Cahill, K.G., Caprio, A.C., Sanders, J.E., Williams, A.P., 2018. Patterns and correlates of giant sequoia foliage dieback during California's 2012–2016 hotter drought. For. Ecol. Manage. 419–420, 268–278. https://doi.org/10.1016/j.foreco.2017.10.053

Stovall, A.E.L., Shugart, H., Yang, X., 2019. Tree height explains mortality risk during an intense drought. Nat. Commun. 10, 1–6. https://doi.org/10.1038/s41467-019-12380-6

Su, Y., Bales, R.C., Ma, Q., Nydick, K., Ray, R.L., Li, W., Guo, Q., 2017. Emerging stress and relative resiliency of giant sequoia groves experiencing multiyear dry periods in a warming climate. J. Geophys. Res. Biogeosciences 122, 3063–3075. https://doi.org/10.1002/2017JG004005

Sulla-Menashe, D., Friedl, M.A., Woodcock, C.E., 2016. Sources of bias and variability in long-term Landsat time series over Canadian boreal forests. Remote Sens. Environ. 177, 206–219. https://doi.org/10.1016/j.rse.2016.02.041

Swetnam, T.W., 1993. Fire history and climate change in giant sequoia groves. Science (80-.). 262, 885–889. https://doi.org/10.1126/science.262.5135.885

Talebi, A., Troch, P.A., Uijlenhoet, R., 2008. A steady-state analytical slope stability model for complex hillslopes. Hydrol. Process. 22, 546–553. https://doi.org/10.1002/hyp.6881

USDA, 2013. Giant Sequoia National Monument, Final Environmental Impact Statement, Appendices Volume 2: Appendix I — Giant Sequoia Inventory.

Van Gunst, K.J., Weisberg, P.J., Yang, J., Fan, Y., 2016. Do denser forests have greater risk of tree mortality: A remote sensing analysis of density-dependent forest mortality. For. Ecol. Manage. 359, 19–32. https://doi.org/10.1016/j.foreco.2015.09.032

Vega García, M., Aznarte, J.L., 2020. Shapley additive explanations for NO2 forecasting. Ecol. Inform. 56, 101039. https://doi.org/10.1016/j.ecoinf.2019.101039

Vermote, E., Justice, C., Claverie, M., Franch, B., 2016. Preliminary analysis of the performance of the Landsat 8/OLI land surface reflectance product. Remote Sens. Environ. 185, 46–56. https://doi.org/10.1016/j.rse.2016.04.008

Vicente-Serrano, S.M., Quiring, S.M., Peña-Gallardo, M., Yuan, S., Domínguez-Castro, F., 2020. A review of environmental droughts: Increased risk under global warming? Earth-Science Rev. 201, 102953. https://doi.org/10.1016/j.earscirev.2019.102953

Vose, J.M., Allen, H.L., 1988. Leaf Area, Stemwood Growth, and Nutrition Relationships in Loblolly Pine. For. Sci. 34, 547–563. https://doi.org/10.1093/forestscience/34.3.547

Warter, M.M., Singer, M.B., Cuthbert, M., Roberts, D., Caylor, K., Sabathier, R., Stella, J., 2020. Onset and propagation of drought into soil moisture and vegetation responses during the 2012–2019 drought in Southern California. Hydrol. Earth Syst. Sci. Discuss. 1–35. https://doi.org/10.5194/hess-2020-479

Weatherspoon, C.P., 1986. Silvics of Giant Sequoia, in: Proceedings of the Workshop on Management of Giant Sequoia. Gen. Tech. Rep. PSW-95. Pacific Southwest Forest and Range Experiment Station, Forest Service, US Department of Agriculture, Berkeley, CA, pp. 4–10.

Western, A.W., Grayson, R.B., Blöschl, G., Willgoose, G.R., McMahon, T.A., 1999. Observed spatial organization of soil moisture and its relation to terrain indices. Water Resour. Res. 35, 797–810. https://doi.org/10.1029/1998WR900065

Willard, D., 1994. The Natural Giant Sequoia (Sequoiadendron Giganteum) Groves of the Sierra Nevada, California-An Updated Annotated List. Proc. Symp. Giant Sequoias Their place Ecosyst. Soc. Visalia, CA 159–164.

Williams, A.P., Allen, C.D., Macalady, A.K., Griffin, D., Woodhouse, C.A., Meko, D.M., Swetnam, T.W., Rauscher, S.A., Seager, R., Grissino-Mayer, H.D., Dean, J.S., Cook, E.R., Gangodagamage, C., Cai, M., Mcdowell, N.G., 2013. Temperature as a potent driver of regional forest drought stress and tree mortality. Nat. Clim. Chang. 3, 292–297. https://doi.org/10.1038/nclimate1693

Williams, A.P., Cook, E.R., Smerdon, J.E., Cook, B.I., Abatzoglou, J.T., Bolles, K., Baek, S.H., Badger, A.M., Livneh, B., 2020. Large contribution from anthropogenic warming to an emerging North American megadrought. Science (80-.). 368, 314–318. https://doi.org/10.1126/science.aaz9600

Yin, J., Deng, Z., Ines, A.V.M., Wu, J., Rasu, E., 2020. Forecast of short-term daily reference evapotranspiration under limited meteorological variables using a hybrid bi-directional long short-term memory model (Bi-LSTM). Agric. Water Manag. 242, 106386. https://doi.org/10.1016/j.agwat.2020.106386

York, R. a, Battles, J.J., Heald, R.C., 2003. Edge effects in mixed conifer group selection openings: tree height response to resource gradients. For. Ecol. Manage. 179, 107–121. https://doi.org/10.1016/S0378-1127(02)00487-5

Young, D.J.N., Stevens, J.T., Earles, J.M., Moore, J., Ellis, A., Jirka, A.L., Latimer, A.M., 2017. Long-term climate and competition explain forest mortality patterns under extreme drought. Ecol.

Lett. 20, 78–86. https://doi.org/10.1111/ele.12711

Zhang, J., Zhu, Y., Zhang, X., Ye, M., Yang, J., 2018. Developing a Long Short-Term Memory (LSTM) based model for predicting water table depth in agricultural areas. J. Hydrol. 561, 918–929. https://doi.org/10.1016/j.jhydrol.2018.04.065

Zhang, Z., Glaser, S.D., Bales, R.C., Conklin, M., Rice, R., Marks, D.G., 2017. Technical report: The design and evaluation of a basin-scale wireless sensor network for mountain hydrology. Water Resour. Res. 53, 4487–4498. https://doi.org/10.1002/2016WR019619

Zhao, J., Huang, S., Huang, Q., Wang, H., Leng, G., Fang, W., 2020. Time-lagged response of vegetation dynamics to climatic and teleconnection factors. Catena 189, 104474. https://doi.org/10.1016/j.catena.2020.104474

Zhi, W., Feng, D., Tsai, W.P., Sterle, G., Harpold, A., Shen, C., Li, L., 2021. From hydrometeorology to river water quality: Can a deep learning model predict dissolved oxygen at the continental scale? Environ. Sci. Technol. 55, 2357–2368. https://doi.org/10.1021/acs.est.0c06783

Zhu, X.J., Yu, G.R., Hu, Z.M., Wang, Q.F., He, H.L., Yan, J.H., Wang, H.M., Zhang, J.H., 2015. Spatiotemporal variations of T/ET (the ratio of transpiration to evapotranspiration) in three forests of Eastern China. Ecol. Indic. 52, 411–421. https://doi.org/10.1016/j.ecolind.2014.12.030

Zhu, Z., Woodcock, C.E., 2012. Object-based cloud and cloud shadow detection in Landsat imagery. Remote Sens. Environ. 118, 83–94. https://doi.org/10.1016/j.rse.2011.10.028

Tables and Figures

Table 1. Attributes of all 78 giant-sequoia groves in the Sierra Nevada.

ID	Grove name	Lat, °	Lon, °	Area, km^2	Elevation, m	*P*, mm	T, °C	LAI	Class
1	Mt Home	36.232	-118.685	15.576	1943	962	9.8	2.34	ML
2	Redwd Mtn	36.696	-118.917	13.262	1855	941	9.5	2.06	ML
3	Converse	36.805	-118.976	13.168	1936	942	10.3	2.04	ML
4	Evans	36.780	-118.829	12.865	2032	981	8.7	1.82	HL
5	Belknap	36.130	-118.580	9.546	1820	891	10.7	2.55	LL
6	Giant Forest	36.565	-118.757	9.355	2088	1029	8.8	1.64	HL
7	Black Mtn	36.114	-118.668	8.013	1919	844	10.6	2.29	ML
8	Dillonwood	36.306	-118.710	6.799	1921	975	9.6	2.25	MM
9	Garfield	36.335	-118.717	6.236	2023	968	9.3	1.80	HM
10	Freeman	36.140	-118.510	5.775	1899	927	9.7	2.27	MM
11	Nelder	37.432	-119.589	5.475	1695	1051	10.8	2.76	LM
12	Atwell	36.467	-118.683	5.417	2224	969	8.5	2.02	HM
13	East Fork	36.450	-118.661	3.974	2038	895	9.5	1.84	HM
14	Alder Creek	36.189	-118.630	2.911	1954	928	9.6	2.16	HM
15	Eden Creek	36.404	-118.732	2.904	2020	924	9.7	1.73	HM
16	Midl Tule	36.265	-118.663	2.518	2015	1033	8.5	2.05	HM
17	Bigstump	36.720	-118.972	1.972	1905	927	9.3	2.11	MM
18	Redhill	36.078	-118.615	1.882	1867	892	10.2	2.17	MM
19	Castle Creek	36.517	-118.691	1.695	1838	956	10.3	1.96	MM
20	South Fork	36.358	-118.708	1.667	1906	937	9.8	1.79	MM
21	Peyrone	36.049	-118.617	1.614	1812	870	10.5	2.20	LS
22	Mariposa	37.511	-119.604	1.607	1924	1006	9.5	1.99	MS
23	Grant	36.749	-118.982	1.584	1861	928	9.8	2.06	MS
24	Muir	36.632	-118.841	1.541	2018	982	8.4	1.86	HS
25	Redwood Mdw	36.529	-118.639	1.468	1812	927	10.8	2.24	LS
26	Long Mdw	35.982	-118.601	1.248	2024	896	9.5	2.23	HS
27	Packsaddle	35.930	-118.591	1.213	1944	883	10.0	1.99	MS
28	Burrocreek	36.237	-118.626	1.209	1941	1031	9.0	2.37	MS
29	North Calaveras	38.279	-120.304	1.057	1477	1313	10.6	2.48	LS
30	Oriole Lake	36.471	-118.731	0.989	2002	939	9.9	2.06	HS

31	Homers Nose	36.374	-118.726	0.938	2049	937	9.1	1.94	HS
32	Indian	36.805	-118.942	0.828	1831	961	9.9	1.91	MS
33	South Calaveras	38.243	-120.251	0.784	1484	1230	10.8	2.36	LS
34	Silver Crk	36.242	-118.646	0.776	1746	965	10.7	2.46	LS
35	Wishon	36.218	-118.649	0.690	1460	815	13.2	3.04	LS
36	Deer Mdw	36.778	-118.778	0.678	2093	966	7.9	1.57	HS
37	Horse Creek	36.413	-118.690	0.440	1936	910	8.8	1.67	MS
38	Suwanee	36.588	-118.799	0.421	1930	990	8.8	1.58	MS
39	Redwood Crk	36.458	-118.708	0.418	2012	935	9.4	1.46	HS
40	Board Camp	36.367	-118.716	0.403	1994	932	9.0	2.02	HS
41	Skagway	36.617	-118.845	0.353	1977	973	9.2	1.75	HS
42	Cherry Gap	36.773	-118.969	0.348	1839	977	9.5	2.00	MS
43	Landslide	36.754	-118.864	0.334	2122	1068	7.9	1.62	HS
44	Pine Ridge	36.619	-118.861	0.286	1608	896	10.8	2.06	LS
45	Maggie Mnt	36.260	-118.642	0.267	2198	1085	7.9	1.31	HS
46	Bearskin	36.746	-118.912	0.265	1960	975	8.6	1.74	HS
47	Monarch	36.793	-118.779	0.217	1812	913	9.3	1.66	LS
48	Lost	36.651	-118.828	0.214	2068	1028	7.0	1.77	HS
49	Little Redwd mdw	36.518	-118.624	0.190	2203	890	8.6	1.87	HS
50	Agnew	36.785	-118.775	0.175	2204	980	7.5	1.67	HS
51	Deer Creek	35.872	-118.610	0.166	1719	773	11.5	2.47	LS
52	New Oriole Lake	36.452	-118.736	0.152	1788	867	10.4	2.02	LS
53	Big Baldy South	36.661	-118.899	0.152	1843	913	9.6	1.62	MS
54	Surprise	36.378	-118.761	0.151	1881	885	10.3	1.97	MS
55	Sequoia Creek	36.731	-118.977	0.141	1822	943	9.7	1.79	LS
56	South Peyrone	36.027	-118.623	0.135	1881	880	10.2	2.21	MS
57	Cahoon	36.411	-118.702	0.133	1888	912	9.2	1.66	MS
58	Cedar Flat	36.362	-118.731	0.132	1650	909	11.0	2.42	LS
59	Coffeepot Canyon	36.399	-118.749	0.097	1840	933	10.6	1.88	MS
60	Upper Tule	36.277	-118.673	0.091	2351	1040	8.2	1.58	HS
61	Dennison	36.312	-118.765	0.085	1958	955	10.4	1.61	HS
62	Mckinley	37.016	-119.102	0.076	2015	1012	8.6	1.70	HS
63	Devils Canyon	36.321	-118.768	0.064	1991	955	10.5	1.66	HS
64	Starvation	35.937	-118.622	0.038	1757	849	10.3	2.49	LS
65	Lower Horse Crk	36.420	-118.705	0.028	1652	910	11.6	2.24	LS
66	Cunningham	35.982	-118.569	0.023	1892	771	10.8	1.84	MS
67	Forgotten	36.332	-118.766	0.022	1944	861	10.4	1.60	MS
68	Placer Big Trees	39.057	-120.572	0.021	1619	1578	11.4	2.72	LS
69	Abbott	36.759	-118.979	0.019	1822	939	9.6	2.24	LS
70	Big Springs	36.651	-118.907	0.015	1482	853	12.0	2.70	LS
71	Tuolumne	37.769	-119.807	0.013	1778	989	10.5	2.07	LS
72	Granite Creek	36.538	-118.627	0.013	1940	930	9.2	2.10	MS
73	Clough Camp	36.351	-118.769	0.010	1121	744	15.1	1.62	LS
74	Douglass	36.478	-118.721	0.009	2122	961	9.2	1.32	HS
75	W Redwood Mnt	36.655	-118.913	0.006	1543	865	10.6	2.66	LS
76	Merced	37.749	-119.840	0.004	1672	979	11.2	2.95	LS

77	Squirrel Creek	36.465	-118.754	0.003	1570	862	11.3	2.33	LS
78	Putnam-Francis	36.348	-118.751	0.003	1253	803	14.0	2.15	LS

Note: Groves are sorted by area from largest to smallest; the latitude and longitude are for grove centroid; mean annual precipitation (*P*) and temperature (T) are from PRISM dataset for 1985-2018; median annual LAI is from MODIS LAI/FPAR product (MOD15A2H) for 2001-2018; groves are classified based on elevation (High, Medium, Low) and area (Large, Medium, Small), with first letter of the abbreviation denoting the elevation class, and second letter for area class, e.g. HL stands for grove classified as high-large.

Table 2. Inputs for the deep-learning LSTM model.

Inputs[a]	Description	Unit	Source
Dynamic forcing			
P	Annual precipitation in current year t	mm	PRISM; Daly et al. (2008)
T	Mean annual temperature in current year t	°C	PRISM
ET_p	Annual evapotranspiration in previous year t–1	mm	Eq 1 using Landsat NDVI
Fire	Fire occurrence in current year t (binary data: 1 for fire occurrence; 0 for non-fire)	-	CA Fire and Resource Assessment Program (FRAP); https://frap.fire.ca.gov/frap-projects/fire-perimeters/
Static features			
$NDVI_m$	Normal vegetation condition (median of 1985-2010 NDVI)	-	Landsat
P_m	Normal precipitation (mean of 1985-2010)	mm	PRISM
T_m	Normal temperature (mean of 1985-2010)	°C	PRISM
Min. P–ET	Historical-minimum water availability (i.e. minimum value of 1985-2018 annual *P–ET*)	mm	PRISM and Eq 1
SWE	Mean Snow Water Equivalent (SWE) on April 1st (mean of 1985-2016)	mm	Margulis et al. (2016)
Ele	Elevation form Digital Elevation Model (DEM)	m	SRTM; Farr et al. (2007)
Lat	Latitude	°	DEM
Lon	Longitude	°	DEM
TWI	Topographic Wetness Index derived from DEM	-	DEM
Asp	Aspect derived from DEM	°	DEM
Slp	Slope derived from DEM	°	DEM
SoilDP	Soil depth over bedrock	m	Pelletier et al. (2016)
$SoilK_{sat}$	Soil conductivity from USDA-NCSS State Soil Geographic (STATSGO2) Database	μm s^{-1}	STATSGO2; https://casoilresource.lawr.ucdavis.edu/soil-properties/
AWC	Available Water holding Capacity	cm	STATSGO2
Sand	Percent sand	%	STATSGO2
Silt	Percent silt	%	STATSGO2
Clay	Percent clay	%	STATSGO2
SubPor	Subsurface porosity from Global HYdrogeology MaPS (GLHYMPS)	-	GLHYMPS; Gleeson et al. (2014)
SubK	Logarithmic subsurface permeability	m^2	GLHYMPS
CanPct	Tree canopy cover percentage (mean of 2011 and 2016 data)	%	National Land Cover Database (NLCD)
CanHgt	Forest canopy height	m	Simard et al. (2011)

[a] input data used for predicting *ET* data at target year t for each 30-m gridded pixel, i.e. the vector x_t consisting of 25 feature at time step t in equations S1-S6. Note that an input sequence includes 5 vectors, reflecting that the model was trained with data in recent 5 years (from year t–4 to year t). All data were resampled to 30-m resolution by a bilinear method.

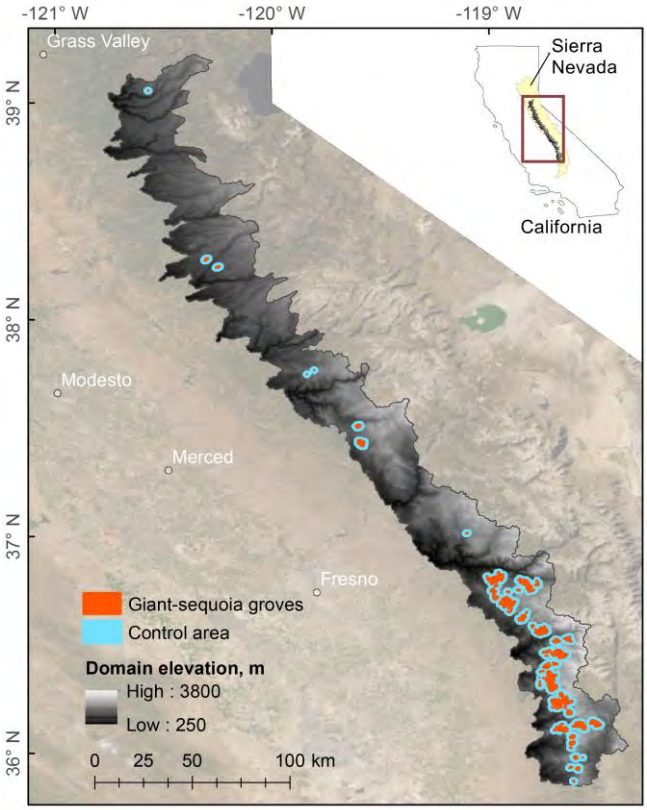

Figure 1. Study domain (color-filled by elevation) in California's Sierra Nevada (yellow zone in the upper-right inset map), including the forested areas in 78 giant-sequoia groves and non-grove control areas. Name, location, and other attributes of each grove are in Table 1 and Figure S1.

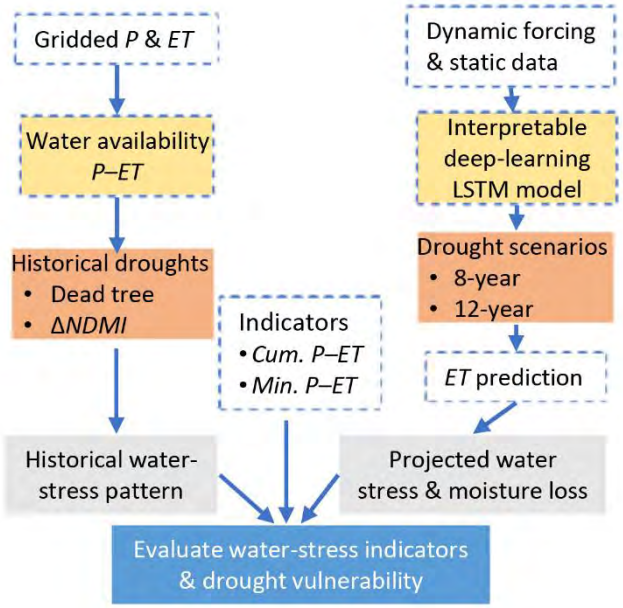

Figure 2. Flowchart of the study to assess water stress in mountain forests during historical droughts and extreme drought scenarios.

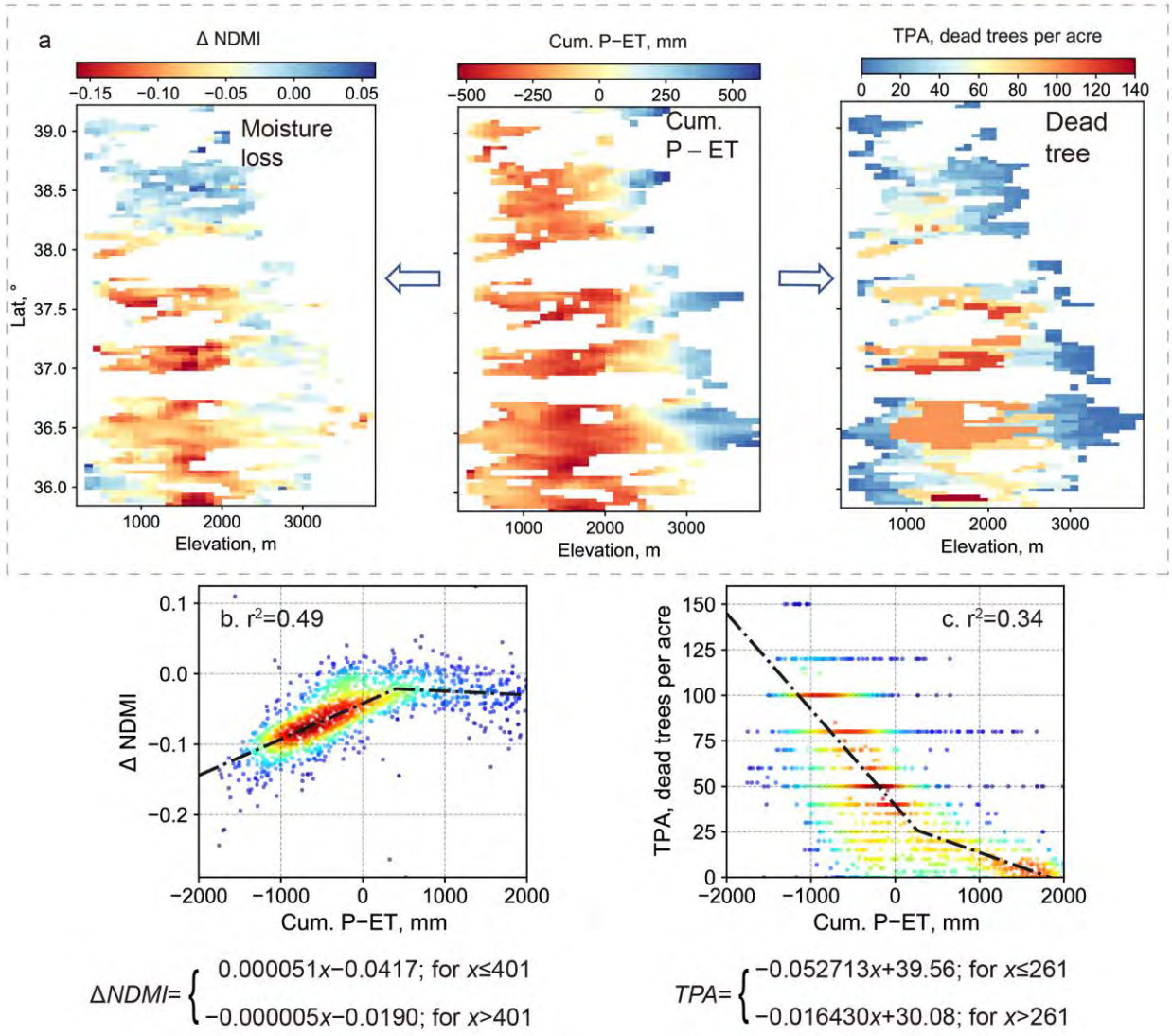

Figure 3. Water-stress metric cumulative *P–ET* as an indicator of tree die-off and moisture loss during the multi-year drought 2012-2015, after Goulden & Bales (2019): (a) patterns of *Cum. P–ET*, moisture loss Δ*NDMI* (2016 minus mean of 2009-2011), and dead tree per area (TPA) for study domain (fire-affected areas were excluded), including giant-sequoia groves and non-grove areas. Two-piece linear regression (black dashed line) using independent variable *Cum. P–ET* (denoted as *x* in fitting equations) to predict moisture loss (b) and dead trees (c). Warm colors toward red indicate denser data points in scatter plots (b-c). Data points were aggregated using 100-m elevation and 0.02695° latitude bins.

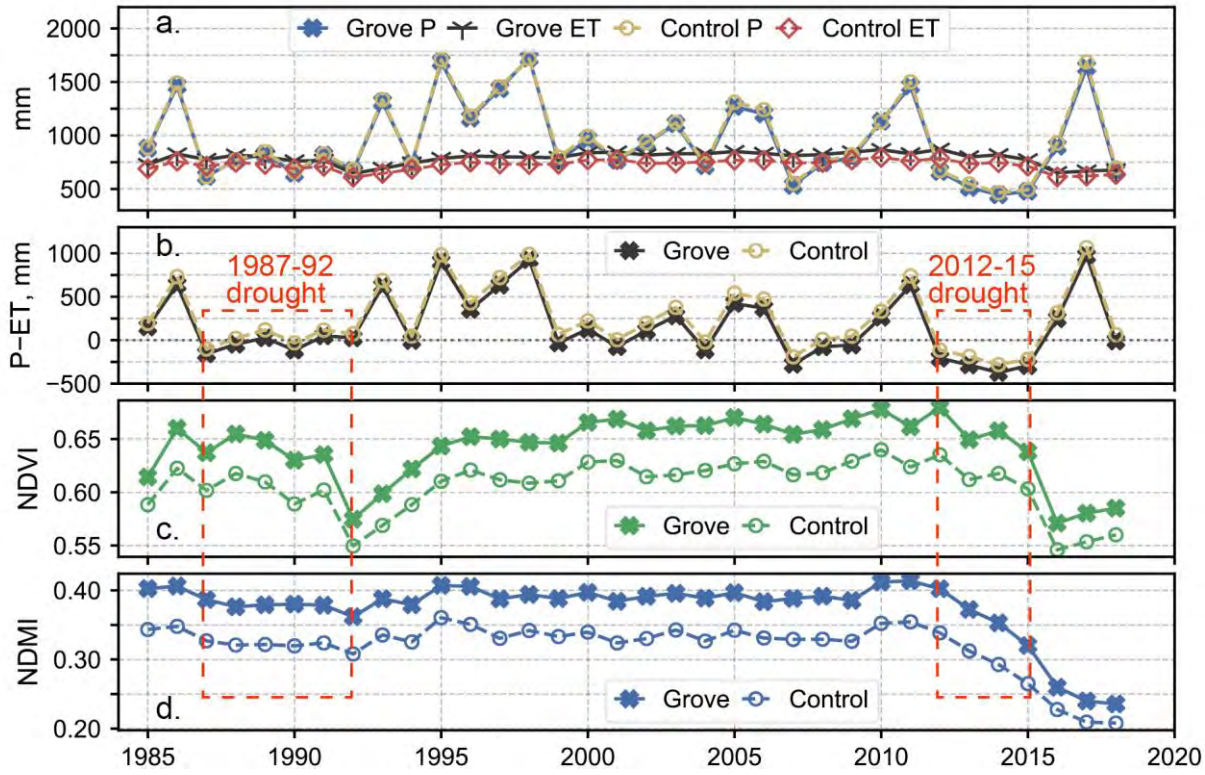

Figure 4. Comparison between giant-sequoia groves and non-grove control areas: a) area-averaged precipitation (*P*) and evapotranspiration (*ET*), b) annual water availability *P–ET* with negative values indicating water stress, c) vegetation greenness denoted by annual *NDVI* from Landsat, and d) canopy moisture represented by summer *NDMI* from Landsat. Two red dashed boxes indicate multi-year droughts of 1987-1992 and 2012-2015.

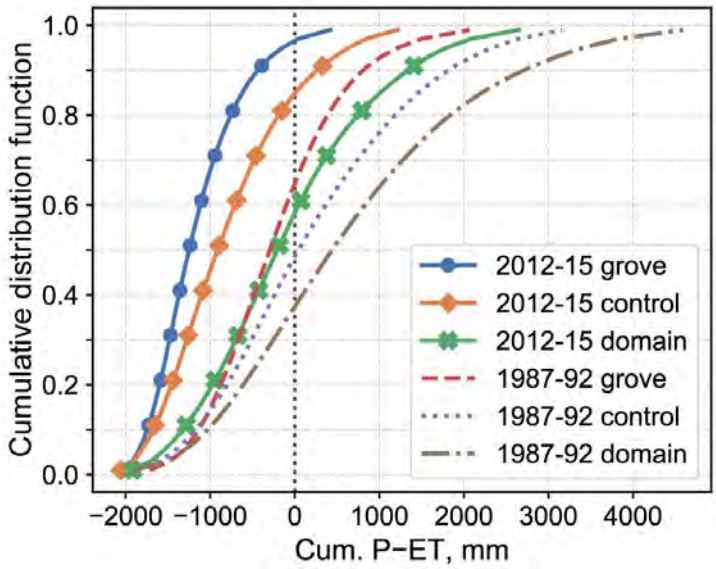

Figure 5. Cumulative distribution function of pixel-level cumulative *P–ET* during two historical droughts, calculated using all 30-m pixels in giant-sequoia groves, non-grove control areas, and study domain, respectively. Negative *Cum. P–ET* indicates water stress.

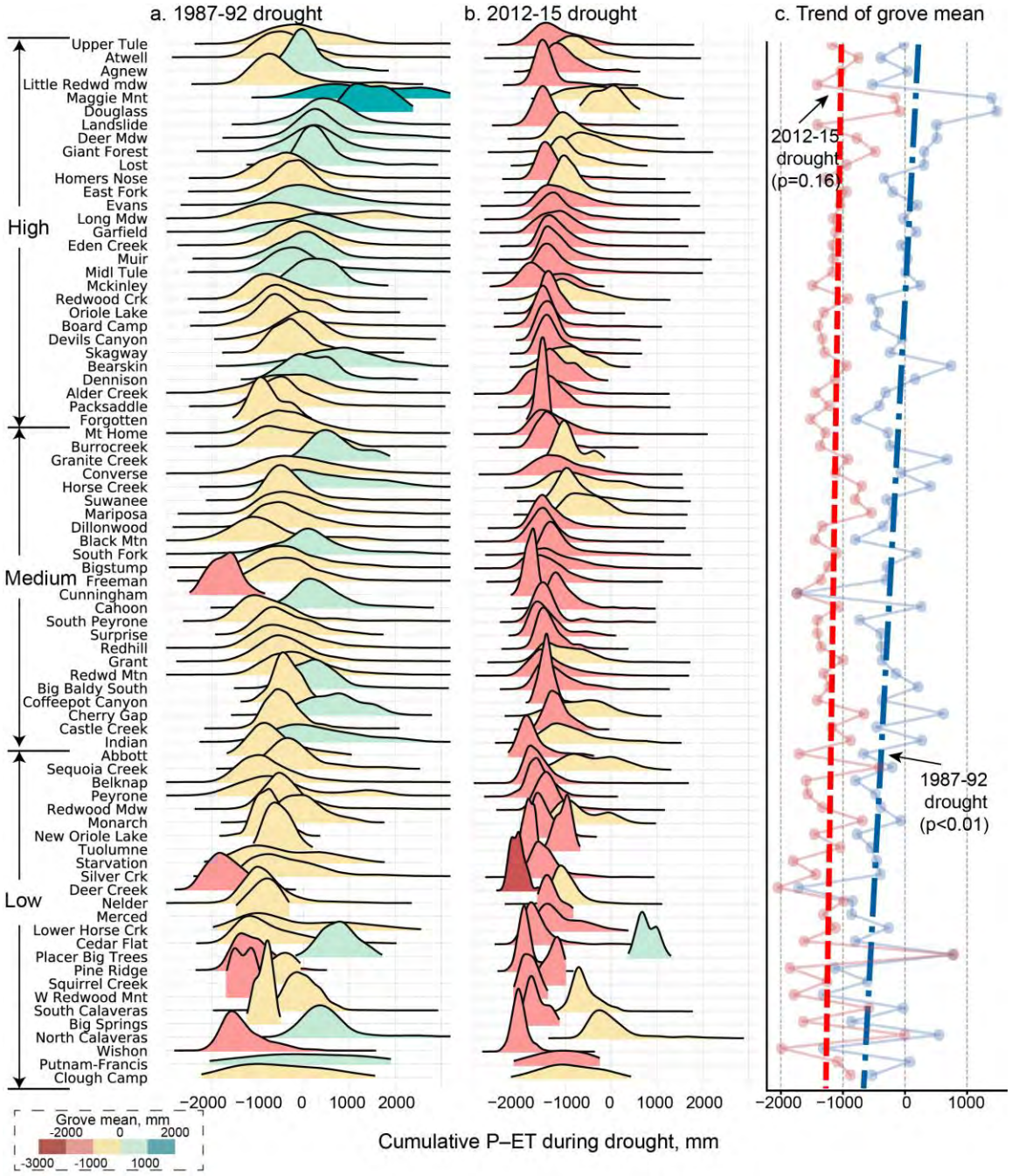

Figure 6. Grove-level cumulative *P–ET* during two historical droughts: a) 1987-1992 and b) 2012-2015. Groves are sorted from high to low elevation. For each grove, the probability-density function of cumulative *P–ET* at all 30-m pixels is plotted and colored by its mean value. c) Trend lines (thick dashed lines from linear regression) of mean cumulative *P–ET* in groves (thin line with circles). P-values of positive linear-regression slopes from the two-sided Wald test are labeled.

https://doi.org/10.1016/j.jhydrol.2022.127431

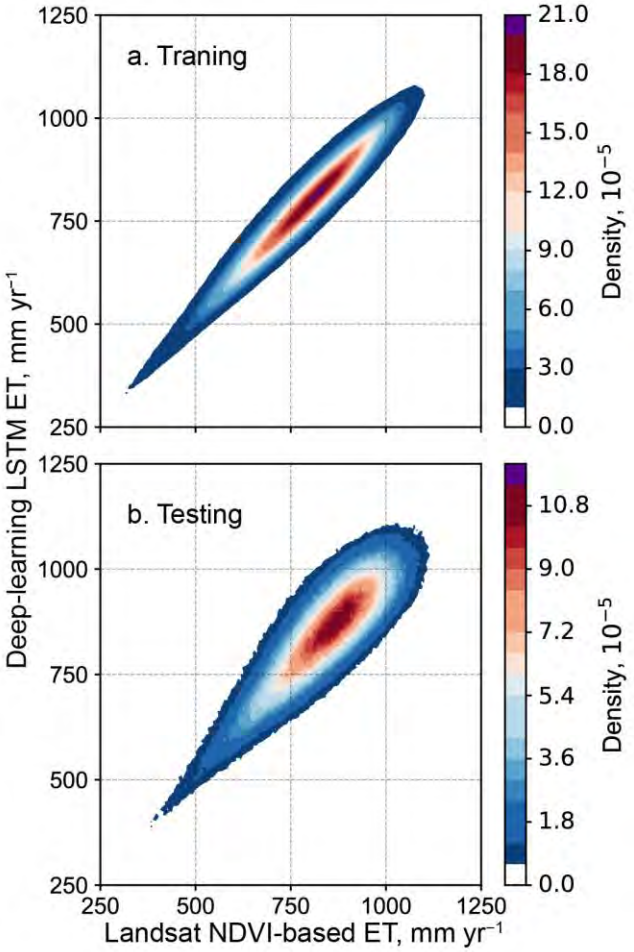

Figure 7. Deep-learning LSTM model performance of *ET* prediction for a) training (1990-2000 & 2009-2018, r^2=0.91) and b) testing (2005-2008, r^2=0.72). Data points are colored by kernel density, with warm colors toward purple indicating more points.

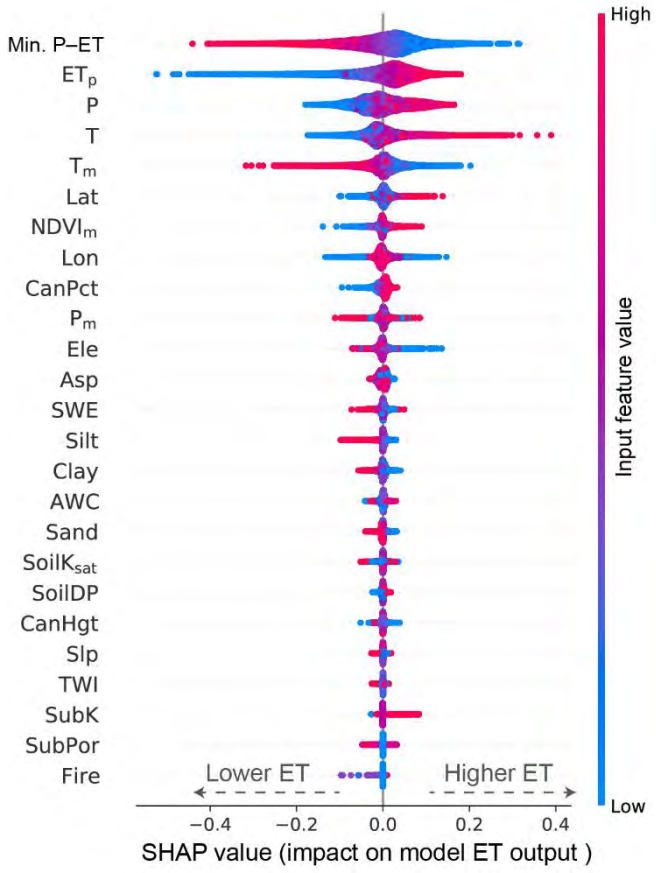

Figure 8. Driver ranking by SHAP values for the LSTM model based on 20,000 data points during the 2012-15 drought. Higher SHAP value of an input feature indicates a contribution to higher *ET* prediction from the LSTM model (see Figure S13 as an example of decomposed SHAP values). Input features (Table 2) from top to bottom are sorted in descending order according to their relative importance (Figure S14).

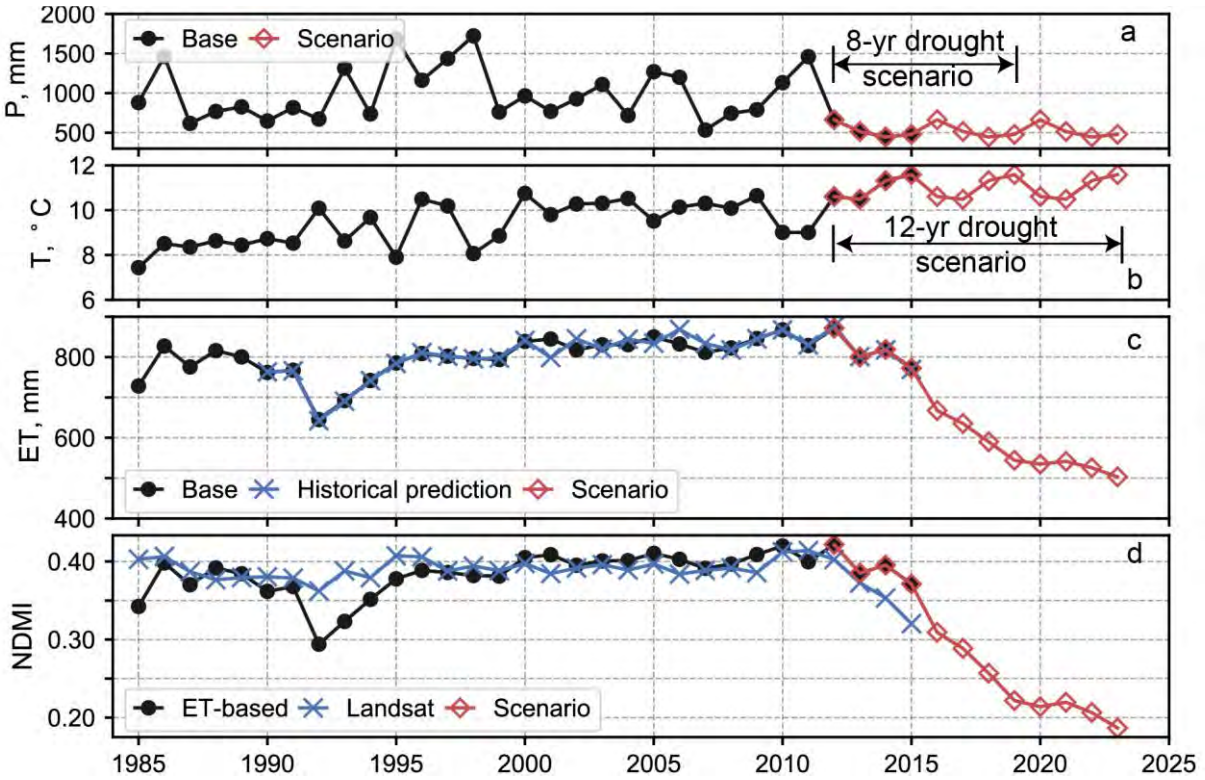

Figure 9. Grove-averaged *ET* and *NDMI* predictions during base period (1985-2015) and two drought scenarios. a) and b) plot precipitation and temperature in groves, respectively. Historical data during the base period are labeled as base, and two hypothetical, extended droughts are marked. c) comparison of *NDVI*-based *ET* during the base-case period, LSTM-model-based historical *ET* prediction, and projected *ET* for drought scenarios by LSTM model. d) comparison of historical Landsat-observed summer *NDMI*, *ET*-based *NDMI* estimates during base-case period, and projected *NDMI* for drought scenarios using the fitted equation in Figure S16.

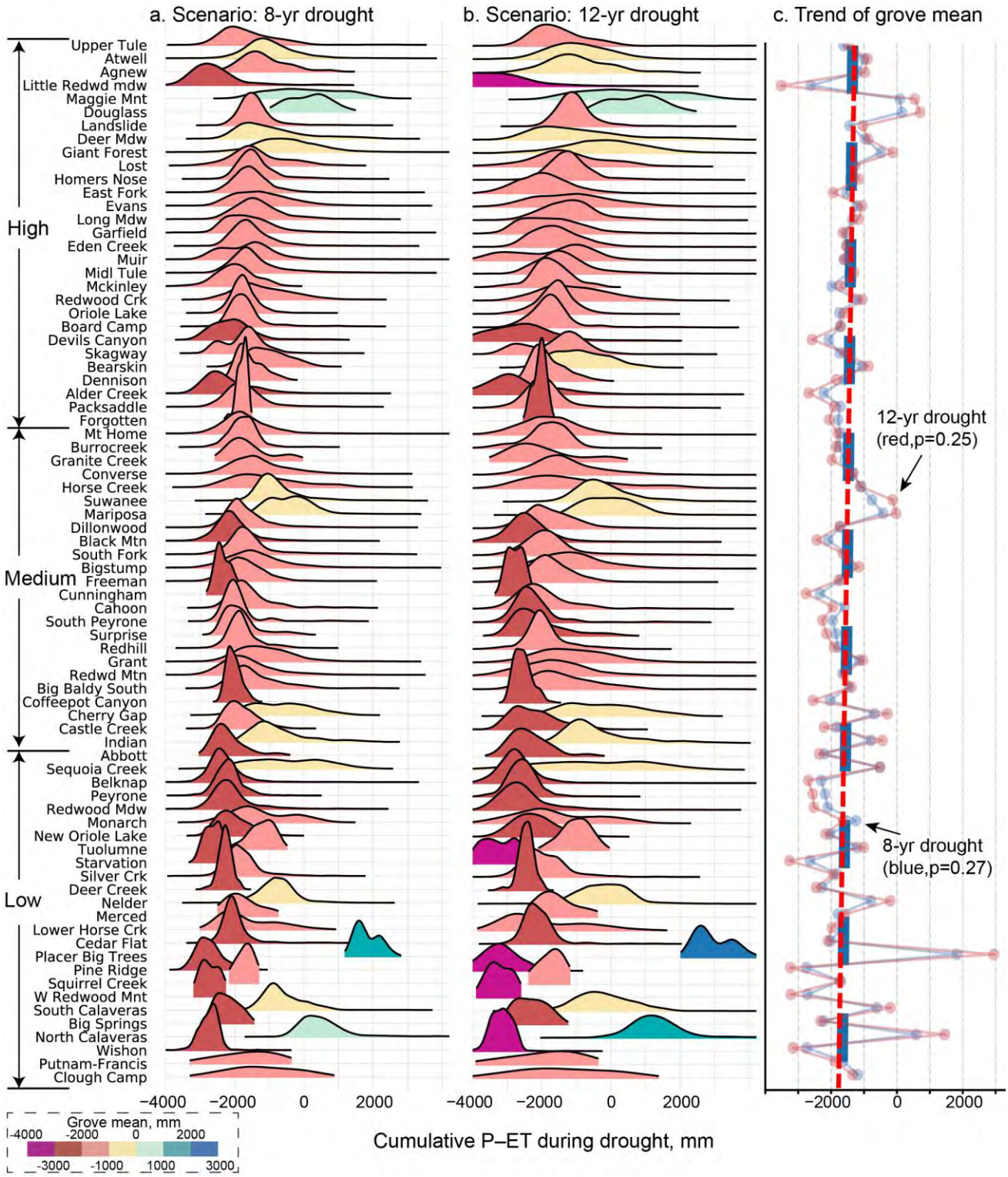

Figure 10. Same as Figure 6, but for LSTM-model-projected cumulative *P–ET* during two scenarios: a) 8-year drought in 2012-19 and b) 12-year drought in 2012-23. Panel (c) plots linear-regression trend lines of mean cumulative *P–ET* in groves, with a thick blue line for 8-year drought and a thin red for 12-year drought. P-values of positive linear-regression slopes are labeled.

https://doi.org/10.1016/j.jhydrol.2022.127431

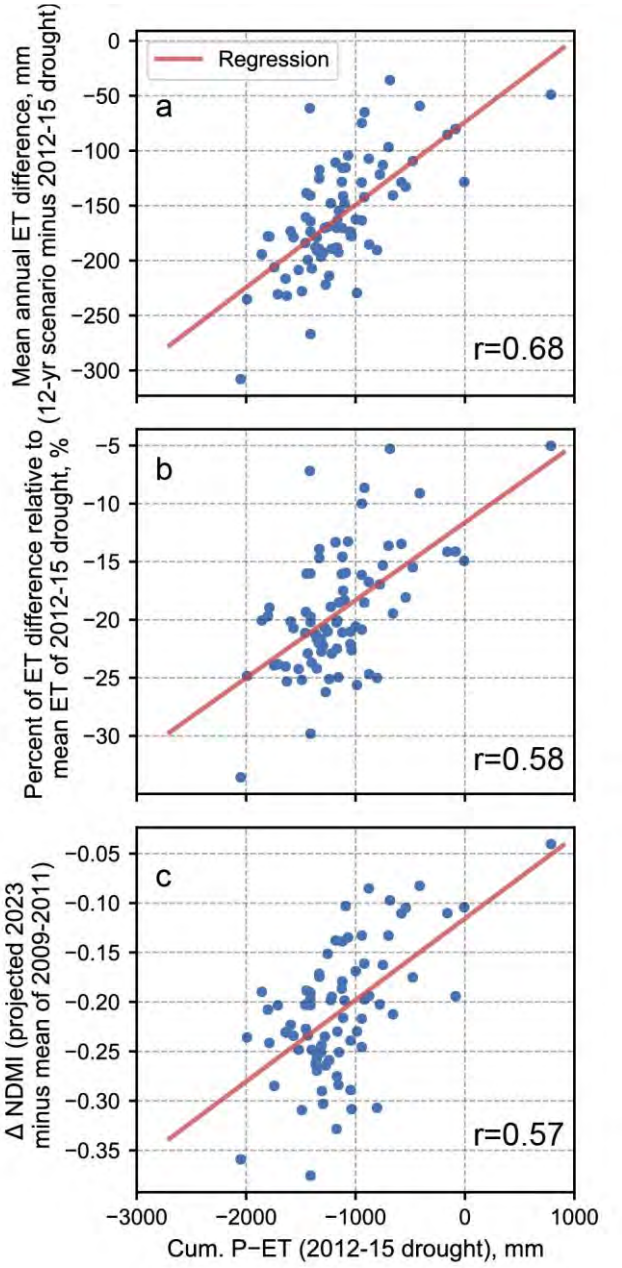

Figure 11. Grove-level changes of *ET* and *NDMI* versus cumulative *P–ET* during the 2012-15 drought. a) mean annual *ET* difference between 12-yr drought scenario and 2012-15 drought. Negative values indicate *ET* drops in 12-yr scenario. b) percent of *ET* difference relative to mean annual *ET* in 2012-15. c) Δ*NDMI* calculated as projected *NDMI* in 2023 minus mean of 2009-2011. Each point represents one giant-sequoia grove, and linear regressions are plotted as red lines. Pearson correlation (r) is labeled in each panel.

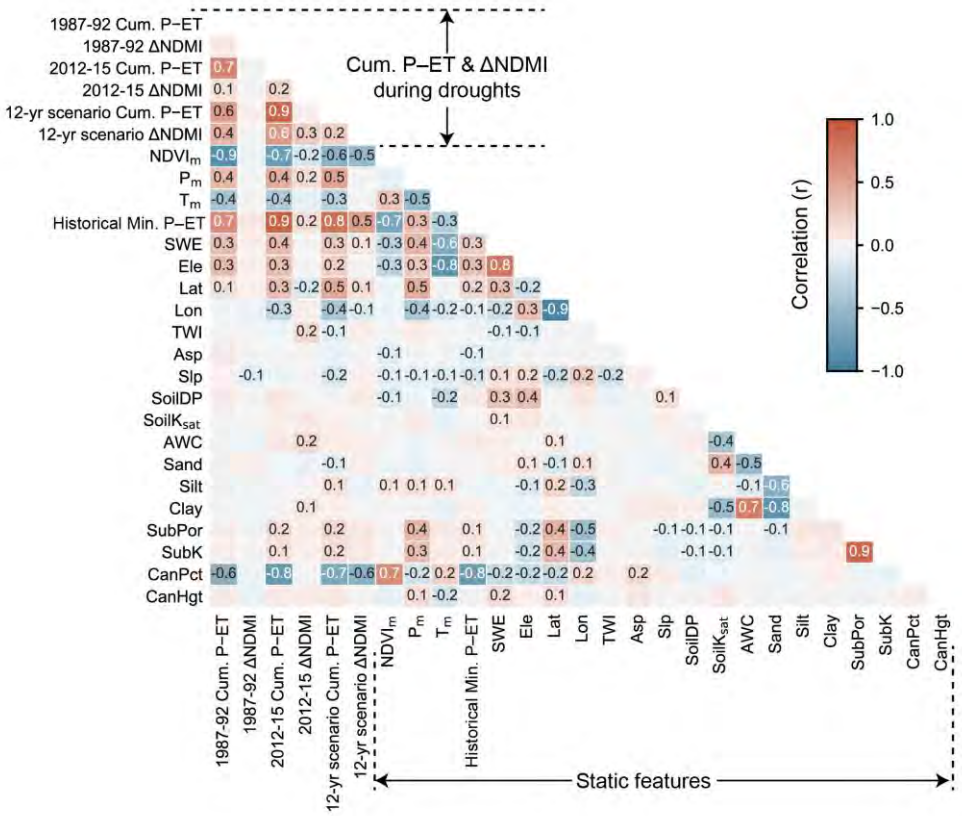

Figure 12. The matrix of Pearson correlations between cumulative *P–ET* and moisture loss (Δ*NDMI*) during two historical and 12-yr hypothetical droughts, and 21 static features. Correlation (r) is calculated using all 30-m pixel data inside groves and labeled for |r| > 0.1.

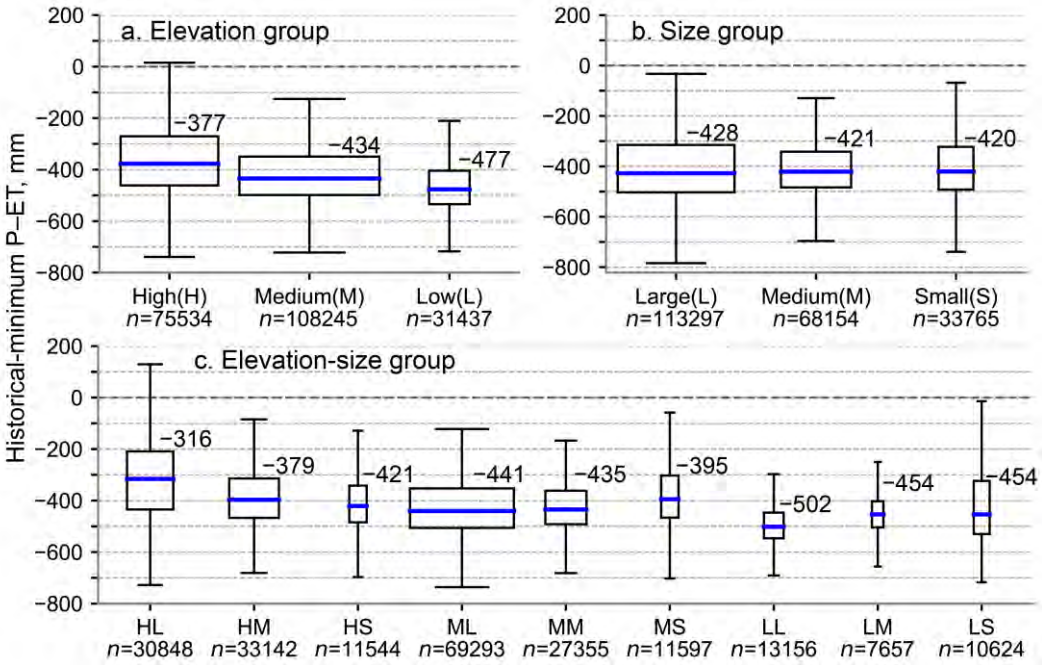

Figure 13. Historical-minimum *P–ET* for different grove groups classified by: a) elevation, b) size, and c) elevation and size. The box denotes interquartile range with lower and upper boundaries of 25th and 75th percentiles of the 30-m pixel-level data inside grove group, respectively; blue line shows median value, which is also labeled; whiskers indicate 1.5 times the interquartile range beyond the boundaries; and box width is proportional to the number (n) of pixel data in each panel. Elevation-area groups are labeled with first letter of the abbreviation denoting elevation group, and second letter for area group, e.g. HL stands for grove classified as High-Large.

Supporting Information

This supporting information includes the supporting texts, tables, and figures referenced in the main text.

Text S1. Equations for Long Short-Term Memory (LSTM) layer

For LSTM layer fed by an input sequence $x = [x_1, \dots, x_T]$ with total T_s time steps (T_s =5 years for this study), the forward pass at time step t ($1 \le t \le T_s$) of the LSTM model is described by the following equations:

$$Input\ gate: \quad i_t = \sigma\left(W^i x_t + U^i h_{t-1} + b^i\right) \tag{S1}$$

$$Forget\ gate: \quad f_t = \sigma\left(W^f x_t + U^f h_{t-1} + b^f\right) \tag{S2}$$

$$Cell\ update: \quad g_t = tanh(W^g x_t + U^g h_{t-1} + b^g) \tag{S3}$$

$$Output\ gate: \quad o_t = \sigma(W^o x_t + U^o h_{t-1} + b^o) \tag{S4}$$

$$Cell\ state: \quad c_t = f_t \otimes c_{t-1} + i_t \otimes g_t \tag{S5}$$

$$Hidden\ state: \quad h_t = o_t \otimes tanh(c_t) \tag{S6}$$

where subscript represents time step t, x_t is input vector of all features (total 25 features for this study) to the LSTM layer, i_t, f_t, and o_t are input, forget, and output gates, respectively, g_t is cell update, c_t and h_t are the memory cell state and hidden state, respectively. Cell state and hidden state at the previous time step are denoted as c_{t-1} and h_{t-1}, respectively. W, U, and b are learnable model weights and bias parameters for different gates/states, which are denoted by different superscripts. $\sigma()$ and $tanh()$ are the sigmoid and hyperbolic tangent functions, respectively. $\otimes$ is the element-wise multiplication operator. h_t represents the LSTM output, which is then fed to dense layer for *ET* prediction.

Text S2. SHapley Additive exPlanations (SHAP)

The SHAP framework proposed by Lundberg & Lee (2017) is used to interpret predictions from deep-learning models. As a member of the class of additive feature attribution methods, SHAP is developed upon other explanation methods, such as the DeepLIFT algorithm (Shrikumar et al., 2017). Based on Shapley values from game theory, the framework explains a specific model output by calculating a real value (i.e. SHAP value) for each input feature. The framework uses an explanation model ($G(z)$) with a linear function of simplified binary variables ($z=\{0,1\}^N$) to approximate orignial model, as in $F(x) = G(z) = \varphi_0 + \sum_{j=1}^{N} \varphi_j z_j$, where $F(x)$ is the original model (i.e. the LSTM model with inputs x in our case), N is the number of input features, $\varphi_0 = F(H_x(0))$ is the model output with all binary variables setting to 0, and $x = H_x(z)$ maps simplified variables to orignial inputs. The SHAP value φ_j for each feature is calculated by finding the single unique solution that satisfies three properties — local accuracy, missingness, and consistency. In this study, we used an enhanced DeepLIFT algorithm in the python SHAP package, where SHAP values are calculated with an explanation model built on a selection of background samples. For more details of the SHAP framework, we refer to orignial papers (Lundberg and Lee, 2017; Lundberg et al., 2018) and other documentations (https://shap.readthedocs.io and https://christophm.github.io/interpretable-ml-book/shap.html).

For our case, decomposed SHAP values in Figure S13 are used as an example to explain the relationship between input features and *ET* prediction. Base value represents the predicted value without any feature knowledge, i.e. mean value obtained over background samples. Features with positive SHAP values are colored in red and increase output value (push the base value toward the right) and contribute to a higher *ET* prediction, such as a relatively smaller value of historical-minimum *P–ET*. Features with negative SHAP values are colored in blue and decrease output value (push the base value toward left) and lower ET prediction, e.g. a relatively lower value of precipitation. As a combination of all feature SHAP values, the output value for this pixel is larger than the base value, meaning that *ET* is predicted higher than the background average.

Table S1. Summary of the settings in the LSTM model.

Name	Description	Setting
Layer 1: LSTM	Hidden neurons	200
Layer 2: Dense	Hidden neurons	200
	Activation	ReLU
Layer 3: Dropout	Dropout rate	0.25
Final layer 4: Dense	Hidden neurons	200
Optimizer	Algorithm	Adam
	Loss function	Mean squared error
Learning rate scheduler	Initial learning rate	0.001
	Scheduler	ReduceLROnPlateau; EarlyStopping
	Training epoch	50
Batch size	Samples in one minibatch	1000

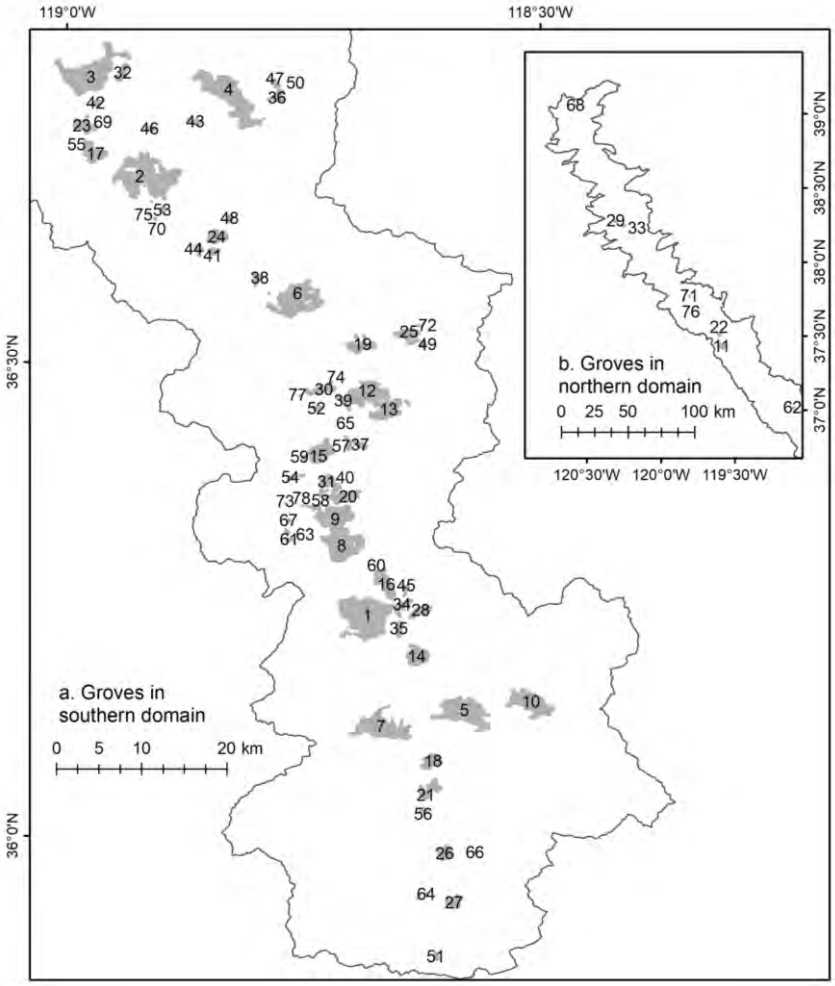

Figure S1. Locations of 78 giant-sequoia groves corresponding to their IDs in Table 1 in a) the southern study domain and b) the northern domain.

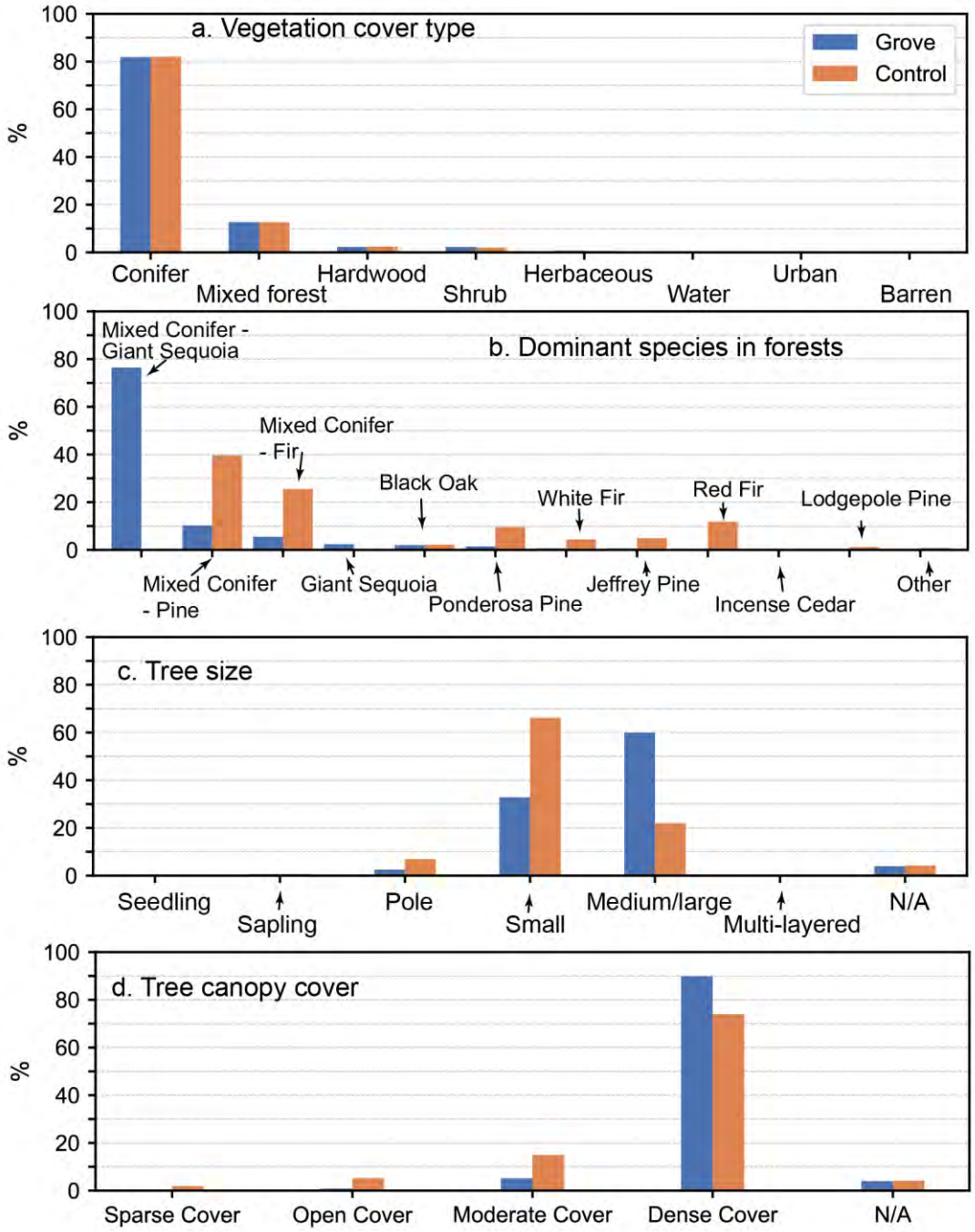

Figure S2. Comparison of forest composition and structure between giant-sequoia groves and non-grove control areas. a) vegetation cover type from USDA Forest Service Region 5 data, see https://www.fs.usda.gov/detail/r5/landmanagement/resourcemanagement/?cid=fsbdev3_048020 for details; b) dominant species in forests from vegetation alliances data in Region 5 dataset; https://www.fs.usda.gov/detail/r5/landmanagement/resourcemanagement/?cid=fsbdev3_048029; c) tree size based on diameter at breast height (DBH) from CALFIRE FRAP dataset. DBH standards for Seedling, Sapling, Pole, Small, and Medium/large trees are <1.0, 1.0-5.9, 6.0-10.9, 11.0-23.9, and ≥24.0 inch, respectively. Multi-layered tree means a distinct layer of Medium/large tree over a distinct layer of Pole or Small tree. N/A means not determined or not applicable for areas with canopy closure <10%, https://www.fs.usda.gov/detail/r5/landmanagement/resourcemanagement/?cid=fsbdev3_047980; and d) tree canopy cover from FRAP dataset. Canopy closure for Sparse, Open, Moderate, Dense Cover are 10.0~24.9%, 25.0-39.9%, 40.0 - 59.9%, and ≥ 60%, respectively; https://www.fs.usda.gov/detail/r5/landmanagement/resourcemanagement/?cid=fsbdev3_048104.

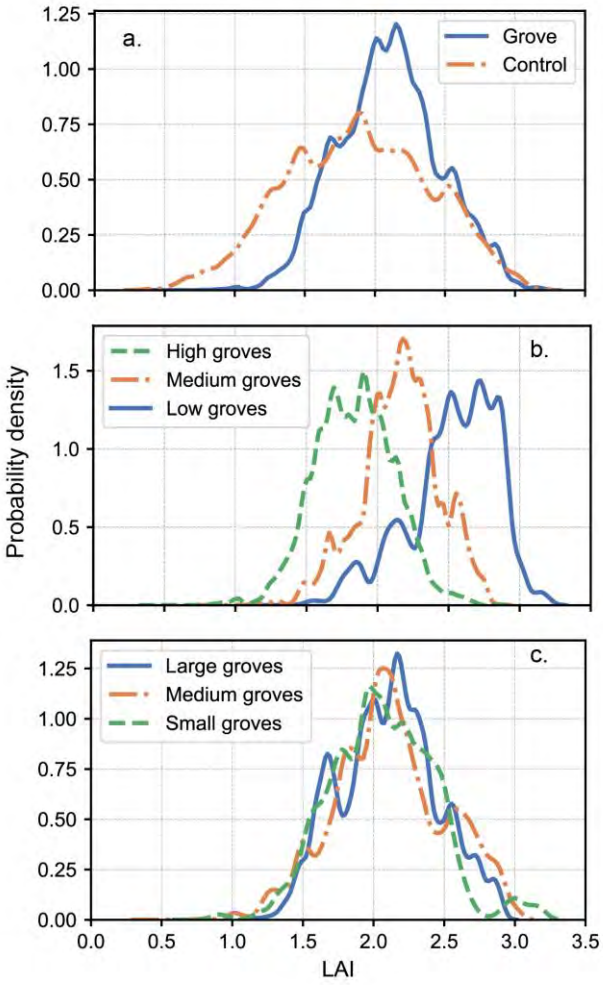

Figure S3. Comparison of the probability density function of Leaf Area Index (LAI), a) between giant-sequoia groves and non-grove control areas; b) across the groves grouped by elevation; c) across the groves grouped by size. LAI is the median of annual values for water year 2001-2018 from MODIS LAI/FPAR product (MOD15A2H, https://lpdaac.usgs.gov/products/mod15a2hv006/).

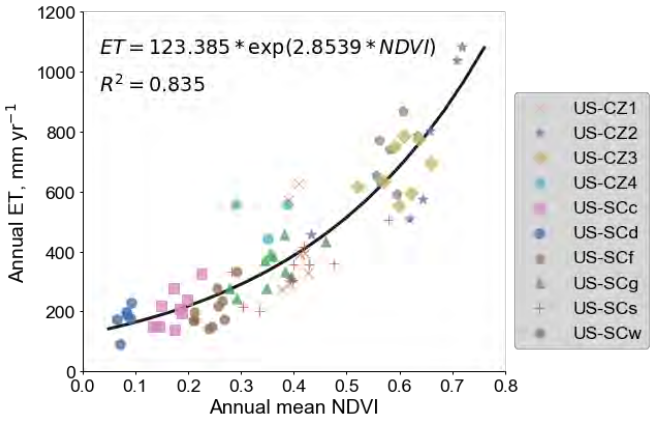

Figure S4. Gridded *ET* (30-m resolution) as a function of Landsat-based annual *NDVI* (homogenized *NDVI* in Figure S5), developed by using flux-tower *ET* measurements and methods from Goulden and Bales (2019). Our fitted equation agrees with that ($ET = 117.16 \times \exp(2.8025 \times NDVI)$, $R^2 = 0.8386$) from Goulden and Bales (2019), in which Landsat *NDVI* data were processed in a slightly different way.

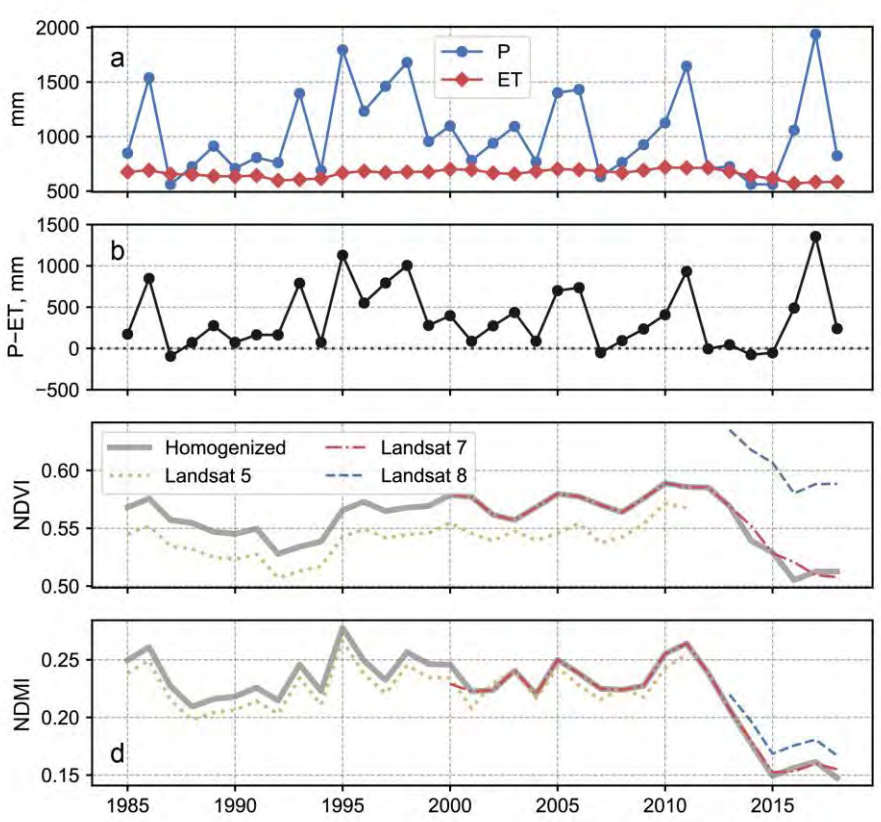

Figure S5. Time-series plots for study domain: a) domain-averaged precipitation (*P*) and evapotranspiration (*ET*), b) annual water availability *P–ET*, c) annual *NDVI* homogenized to Landsat 7, using $NDVI_{L7}$=1.0679× $NDVI_{L5}$–0.0137 for Landsat 5; $NDVI_{L7}$=0.9087× $NDVI_{L8}$–0.0220 for Landsat 8; and d) summer *NDMI* (July-September) from Landsat instruments and after homogenization to Landsat 7 using equations $NDMI_{L7}$=0.9933× $NDMI_{L5}$+0.0131 for Landsat 5; $NDMI_{L7}$=1.0044× $NDMI_{L8}$–0.0201 for Landsat 8. These linear homogenization equations were fitted using common data in 50 1 × 1 km reference sites during overlapping periods (1999-2013 for Landsat 5 and 7; 2013-2018 for Landsat 7 and 8), following the approach used in Su et al. (2017).

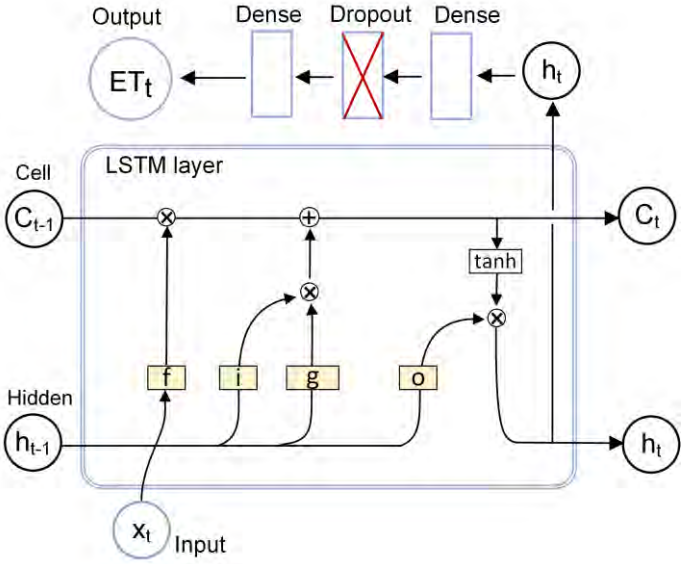

Figure S6. Schematic architecture of LSTM model. Through a series of information control (i.e. input gate (*i*), forget gate (*f*), cell update (*g*), output gate (*o*), and hyperbolic tangent function tanh) of input *x* (a vector containing 25 features shown in Table 2) at time step *t*, cell state C and hidden state h of last time step *t–1*, LSTM layer outputs hidden state h at time step *t* to fully-connected dense layer, dropout layer, and the model finally predicts *ET* at time step *t* by a dense layer. Markers + and × denote pointwise addition and multiplication, respectively.

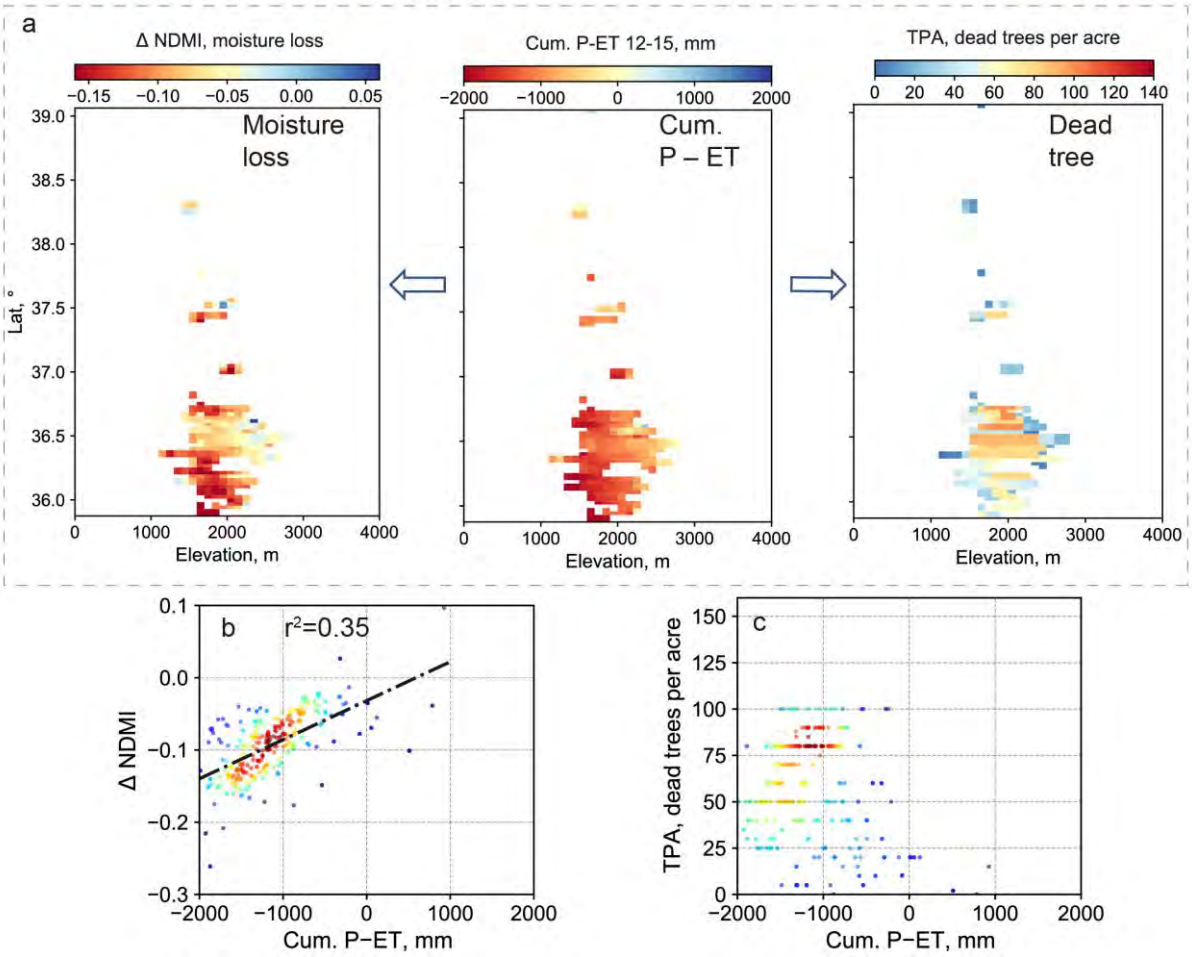

Figure S7. Relationships between cumulative *P–ET* to tree die-off and moisture loss during drought 2012-2015 using aggregated data inside all 78 giant-sequoia groves. (a) patterns of cumulative *P–ET*, moisture loss Δ*NDMI* (2016 minus mean of 2009-2011), and dead tree per area (TPA) for groves. Linear regression (black dashed line) using independent variable cumulative *P–ET* to predict moisture loss (b) and dead tree (c). Warm colors toward red indicate denser data points in scatter plots (b-c). Data points were aggregated using 100-m elevation and 0.02695° latitude bins. Fitted regression in panel b is Δ*NDMI* = –0.03183 + 0.00005395*x*, where x denotes cumulative *P–ET*.

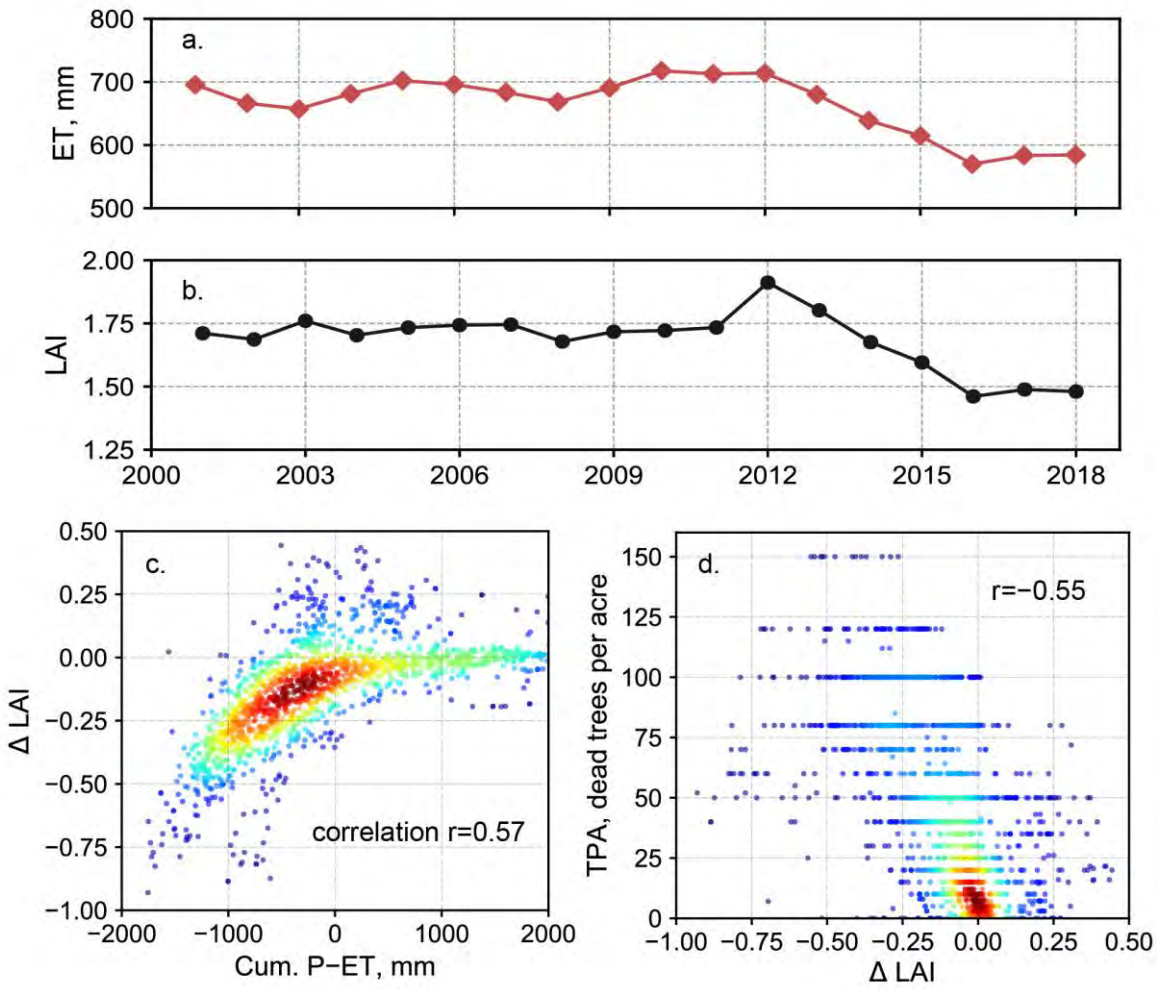

Figure S8. Time-series plots of a) annual Landsat-*ET* and b) annual MODIS LAI for the study domain during 2001-2018. c) Scatter plot of cumulative *P–ET* and LAI change (ΔLAI, 2016 minus mean of 2009-2011) for the 2012-2015 drought. Warm colors toward red indicate denser data points, and Pearson correlation r is labeled. d) Scatter plot of LAI change and dead tree (TPA) for the 2012-2015 drought.

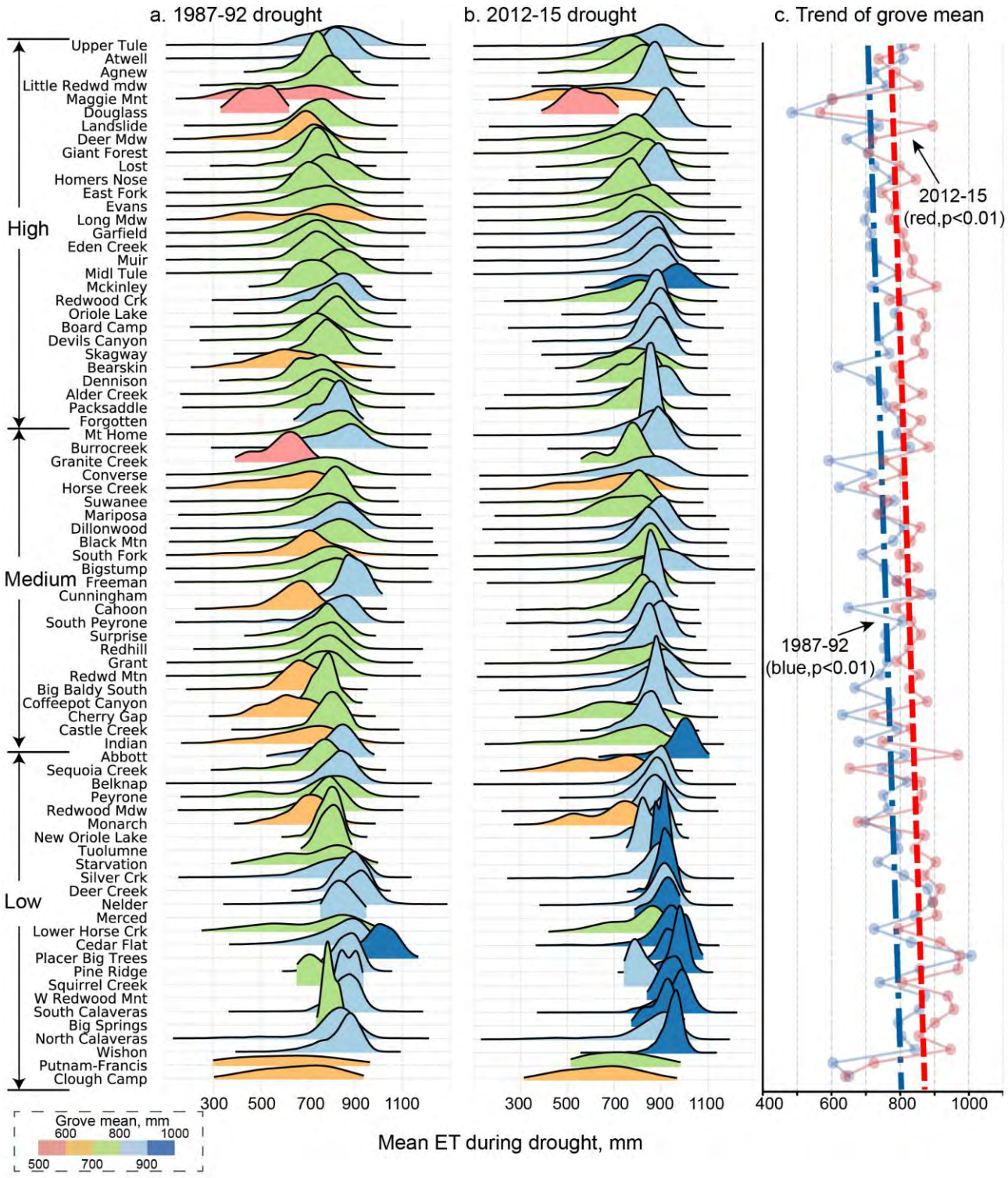

Figure S9. Grove-level mean *ET* during two historical droughts: a) 1987-1992 and b) 2012-2015. Groves are sorted from highest to lowest elevation. For each grove, the probability-density function of *ET* at all 30-m pixels is plotted and colored by its mean value. c) Trend lines (thick dashed lines from linear regression) of groves-mean ET (thin line with circles). P-values of negative linear-regression slopes from the two-sided Wald test are labeled.

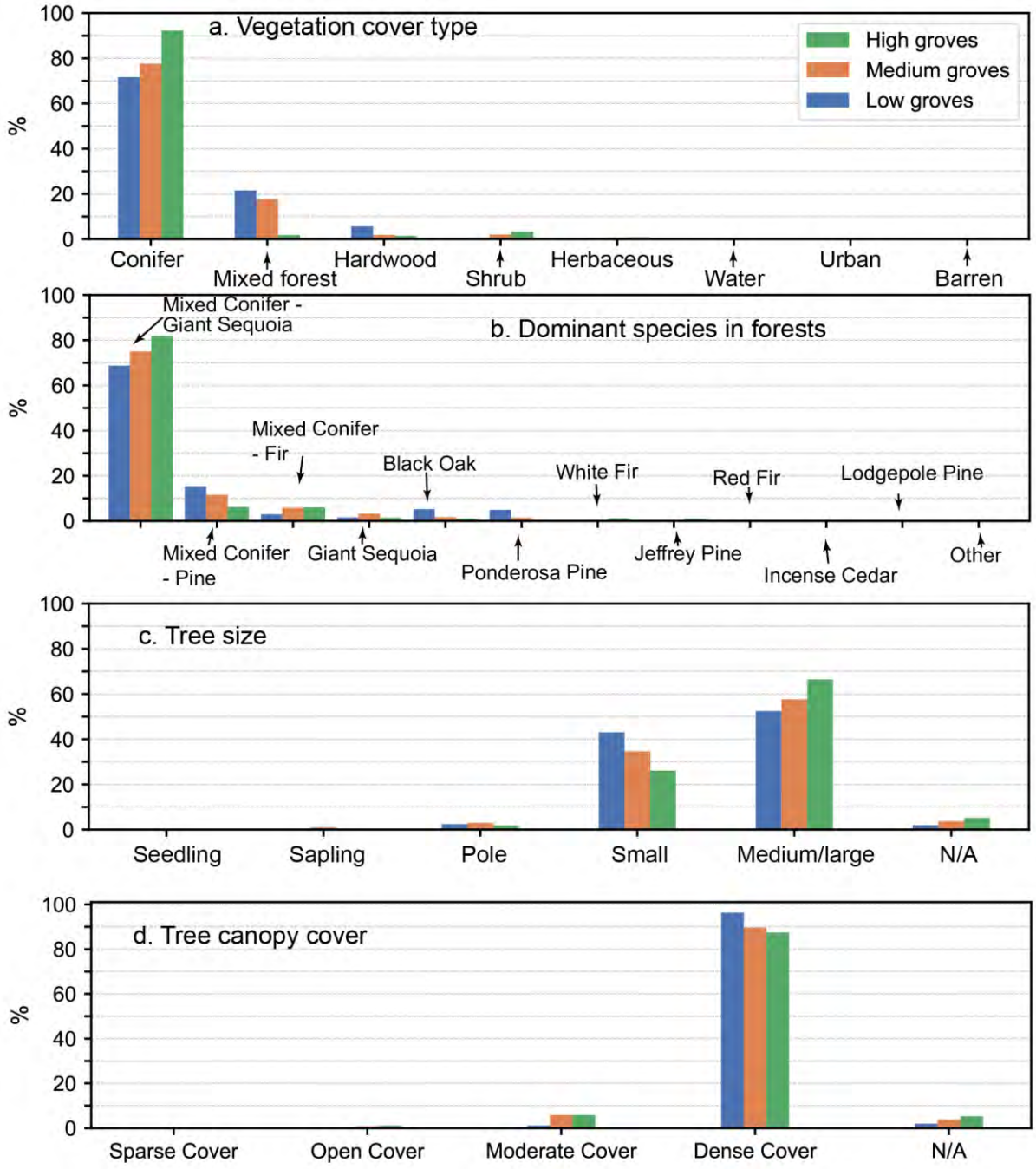

Figure S10. Same as Figure S2, but for comparison of forest composition and structure across giant-sequoia groves grouped by elevation.

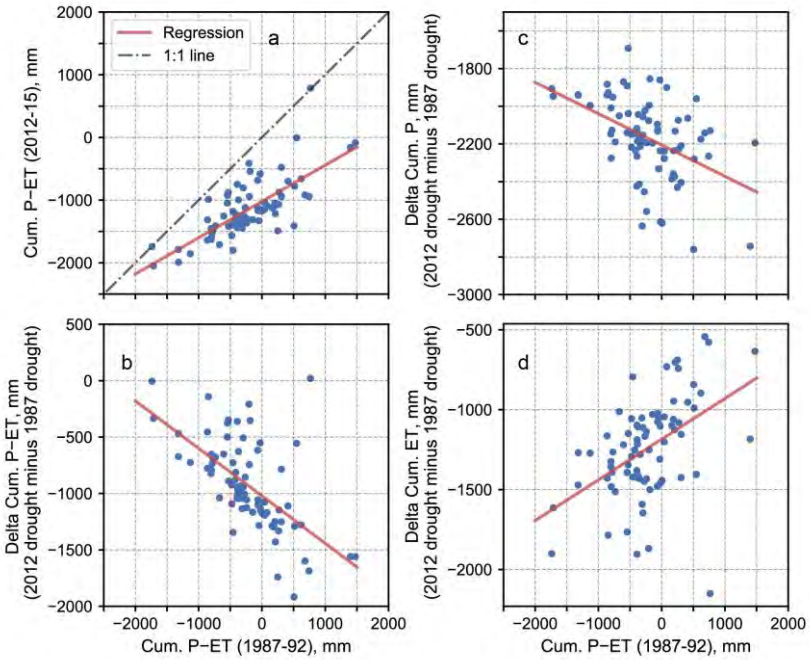

Figure S11. a) Comparison of grove-level cumulative *P–ET* during two historical droughts and b) difference of cumulative *P–ET* (i.e. water-stress changes) between the two droughts. Panels (c) and (d) are similar to (b), but show the difference of cumulative *P* and cumulative *ET*, respectively. Each point represents one giant-sequoia grove, and linear regressions are plotted as red lines. Note that scales on y-axes are different.

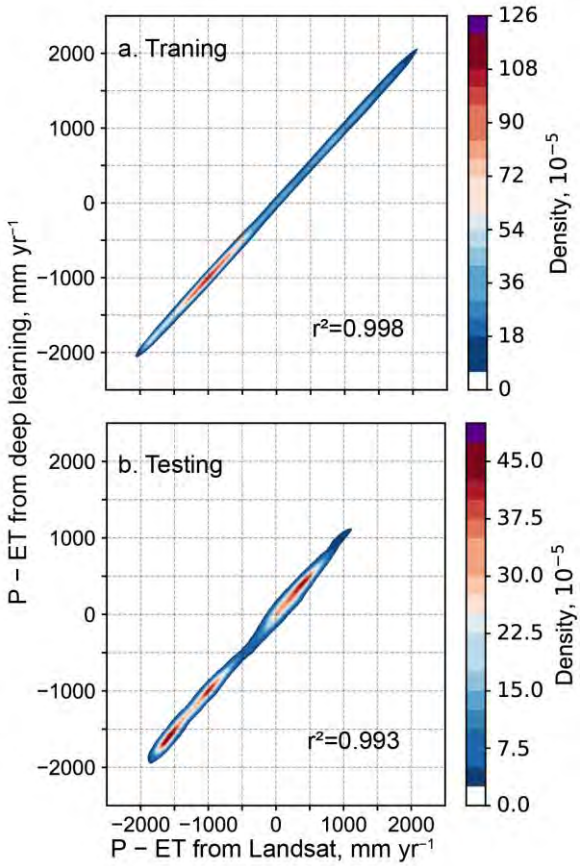

Figure S12. Comparison of water availability (*P–ET*) estimated using Landsat-based *ET* and deep-learning-based *ET* for a) training (1990-2000 & 2009-2018) and b) testing (2005-2008). Data points are contoured and colored by kernel density, with warm colors toward purple indicating more points.

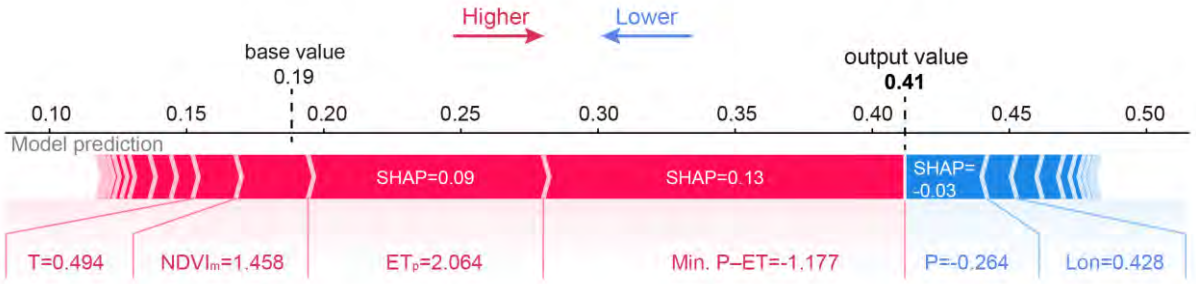

Figure S13. Explanation of an individual *ET* prediction at a 30-m pixel using SHAP. Red features (with positive SHAP values) push the *ET* output higher than the base value (i.e. toward the right), and blue features (with negative SHAP values) push the output lower. Base value represents the predicted *ET* without any feature knowledge, i.e. mean value obtained over 20,000 data points during the 2012-2015 drought. Input feature values are scaled and shown by z-score. In this case, historical-minimum *P–ET* is the primary driver of *ET* prediction.

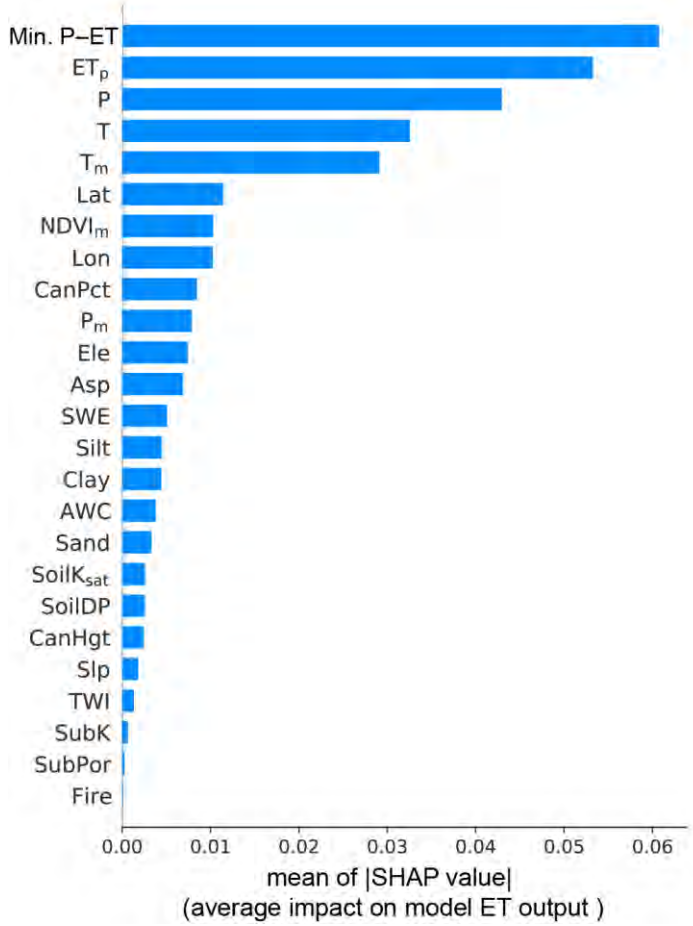

Figure S14. Relative importance of all input features for the deep-learning LSTM model, determined by the average absolute value of the SHAP values.

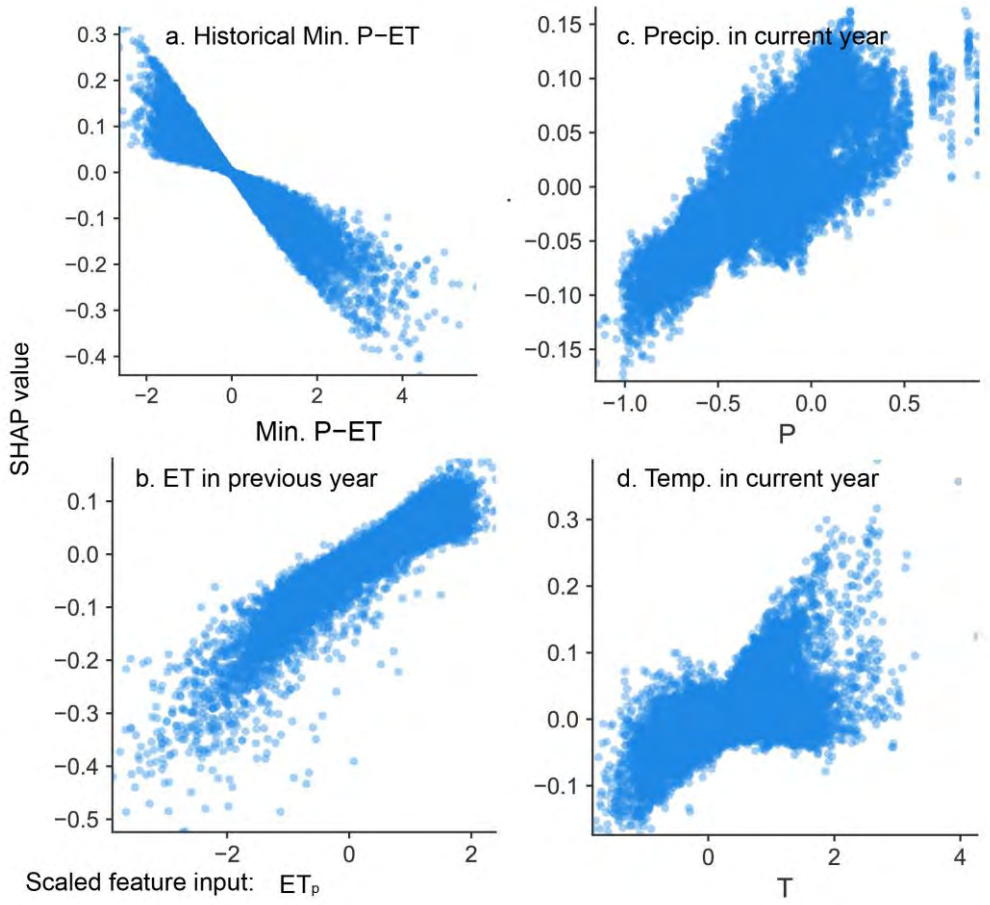

Figure S15. SHAP values for the four most dominant input features: a) historical-minimum *P–ET* with lower negative values indicate historically more-severe water deficit, b) annual evapotranspiration in previous year, c) annual precipitation in current year, and d) mean annual temperature in current year. All feature inputs are scaled using z-score with 0 denoting mean value.

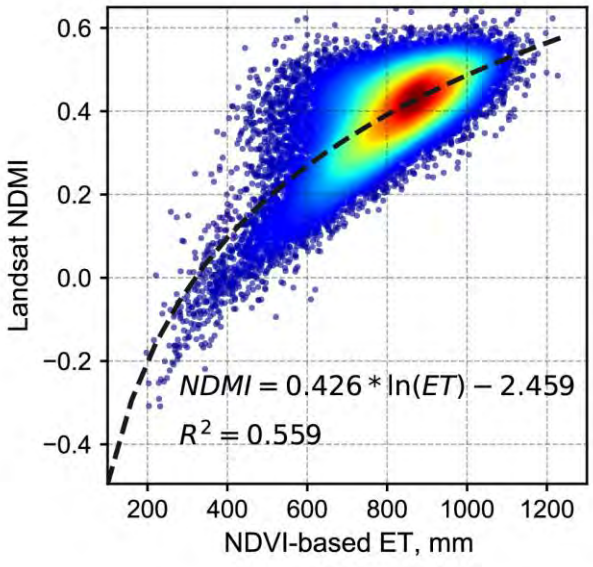

Figure S16. Fitted equation *NDMI*=0.426×ln(*ET*)–2.459 for converting *NDVI*-based *ET* to Landsat summer *NDMI*. Dashed line is fitted line using all 30-m pixel data inside groves during 1985-2018. Randomly selected 20,000 data points are plotted and colored by point density, with red indicating more points.

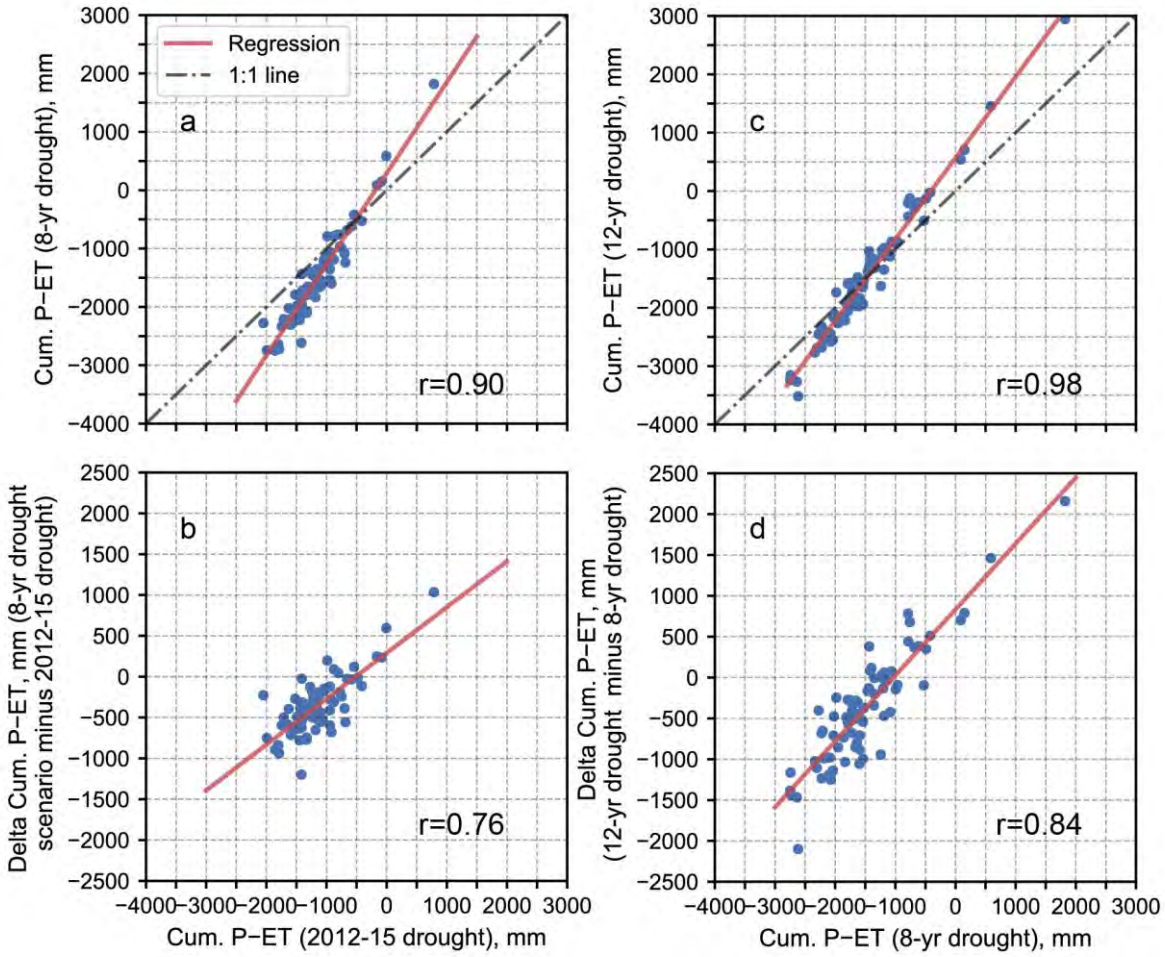

Figure S17. Comparisons of a) grove-level cumulative *P–ET* and b) difference of cumulative *P–ET* between historical 2012-15 and 8-year drought scenarios. Panels (c-d) are similar to (a-b), but for comparisons between 8-year drought scenario and 12-year drought scenario. Pearson correlation (r) is labeled in each panel.

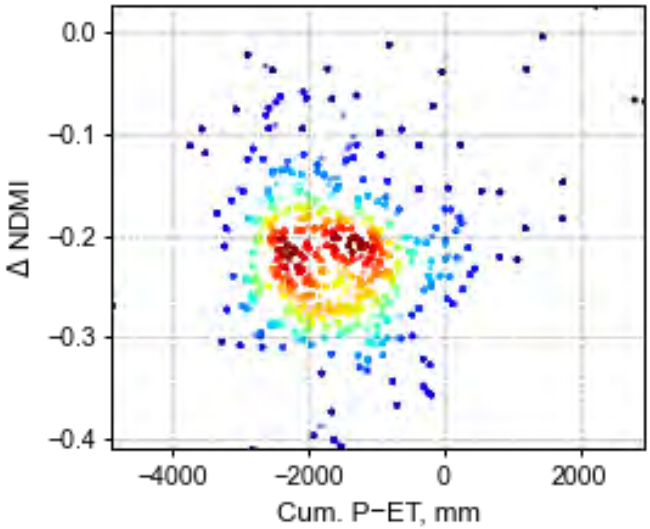

Figure S18. Same as Figure S7b, scatter plot of Cum *P–ET* versus *NDMI* change during the 12-yr drought scenario. *NDMI* change is calculated as the projected value in 2023 minus the mean of 2009-2011.

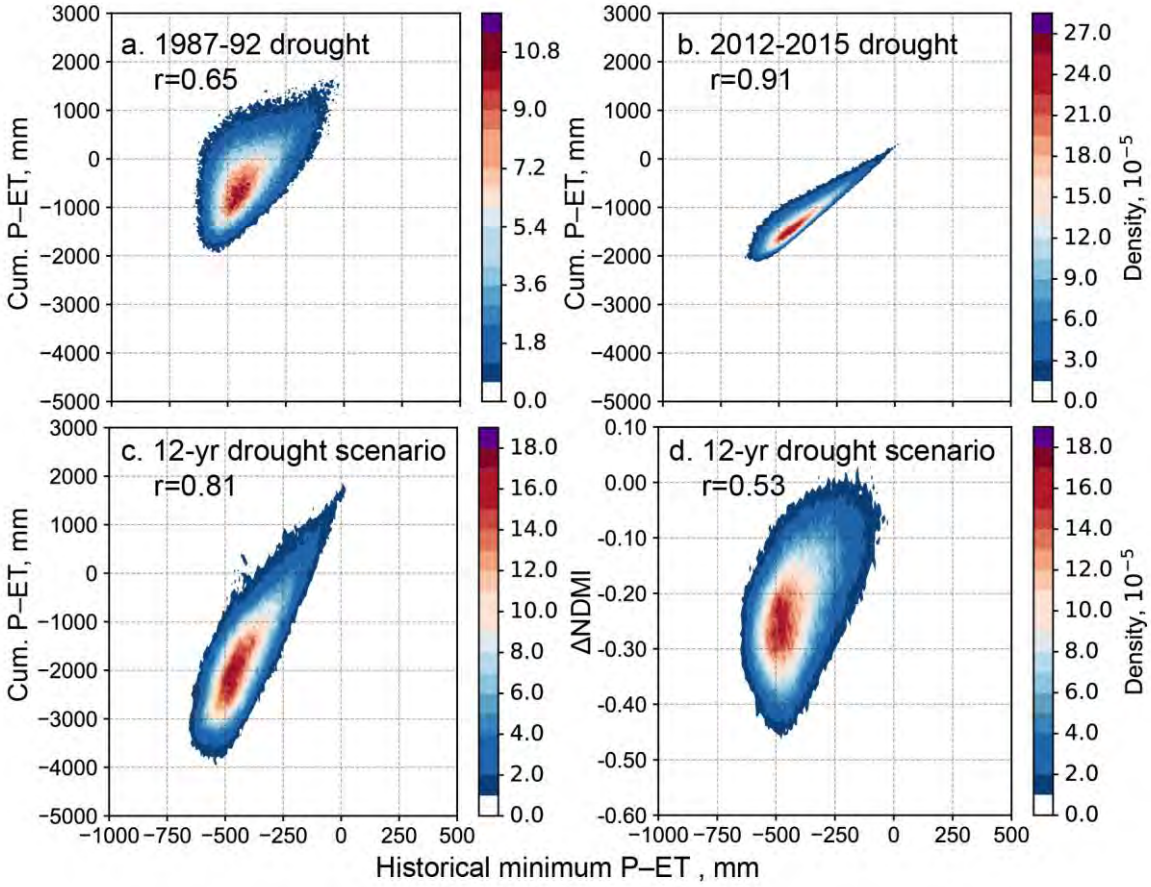

Figure S19. Correlation (r) between historical-minimum *P–ET* and a) cumulative *P–ET* during historical 1987-92 drought, b) cumulative *P–ET* during historical 2012-15 drought, c) projected cumulative *P–ET* during 12-yr drought scenario, and d) projected moisture loss (Δ*NDMI*) during 12-yr drought scenario. Pixel-level data inside all 78 groves are contoured and colored by kernel density, with warm colors toward purple indicating more points.

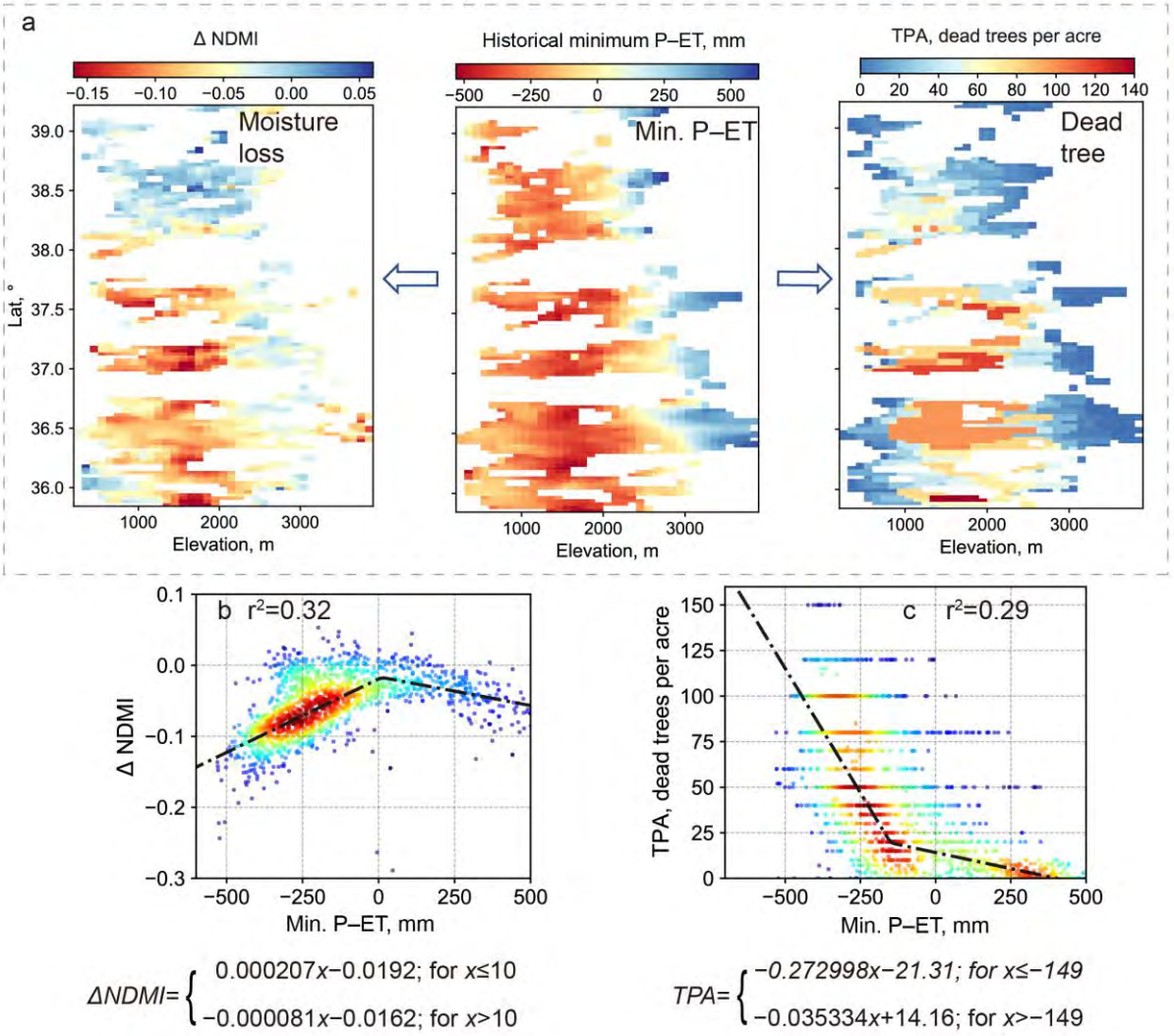

Figure S20. Same as Figure 3, but showing static feature historical-minimum *P–ET* as an indicator of tree die-off and moisture loss during the multi-year drought 2012-2015. (a) patterns of Min. *P–ET*, moisture loss Δ*NDMI* (2016 minus mean of 2009-2011), and dead tree per area (TPA) for study domain (fire-affected areas were excluded), including giant-sequoia groves and non-grove areas. Two-piece linear regression (black dashed line) using independent variable historical-minimum *P–ET* (denoted as x in fitting equations) to predict moisture loss (b) and dead tree (c). Warm colors toward red indicate denser data points in scatter plots (b-c). Data points were aggregated using 100-m elevation and 0.02695° latitude bins.

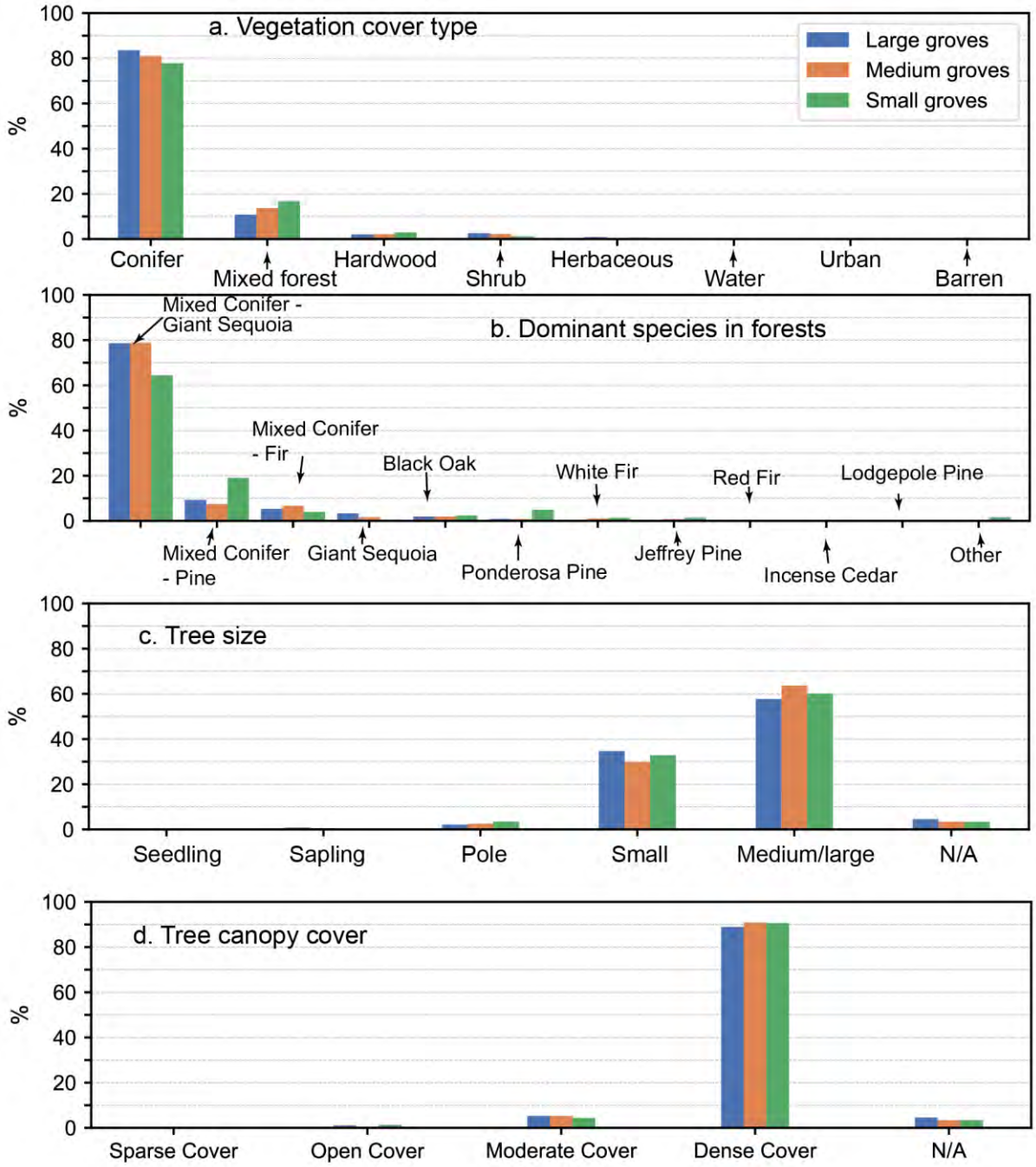

Figure S21. Same as Figure S2, but for comparison of forest composition and structure across giant-sequoia groves grouped by size.

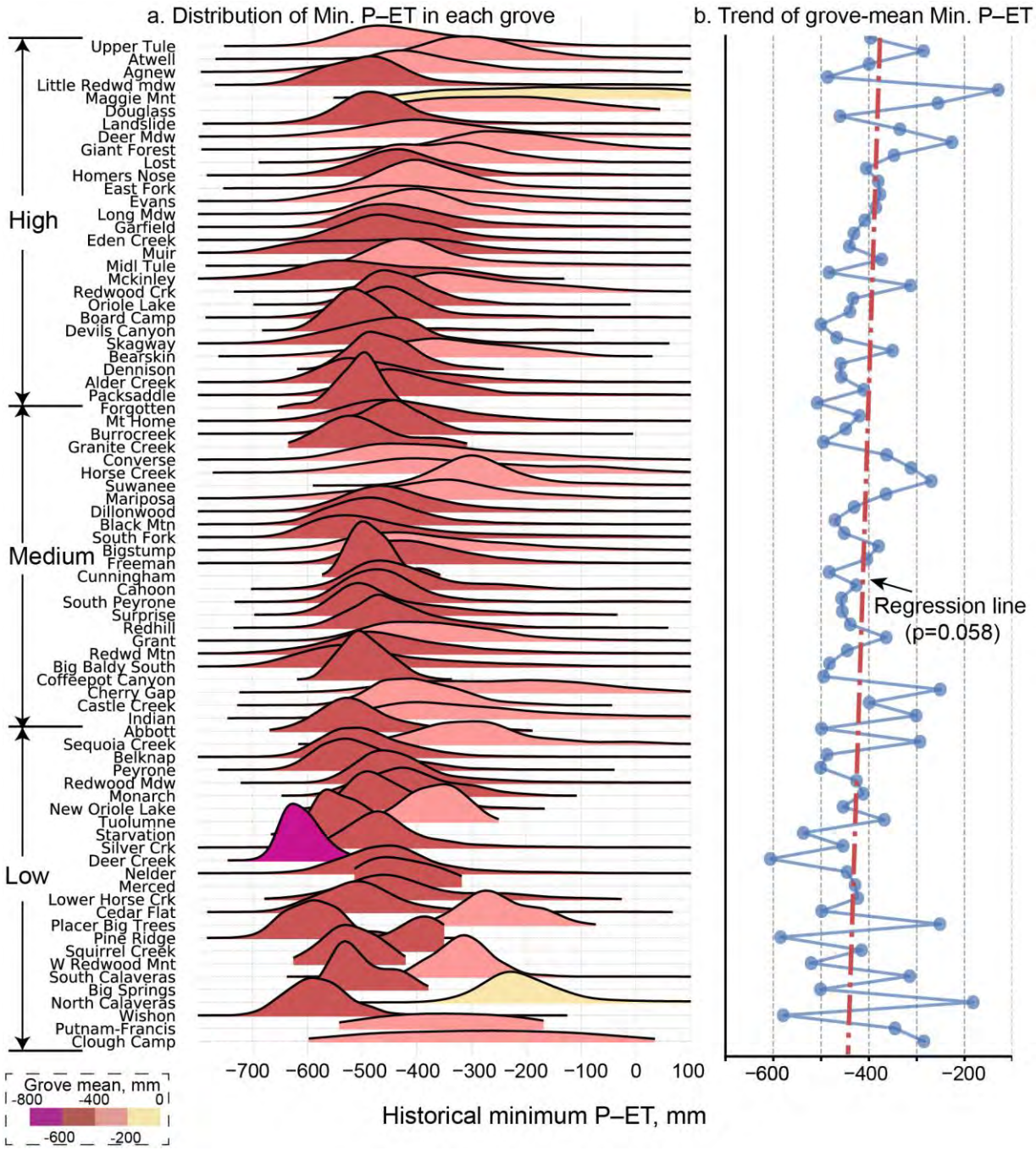

Figure S22. a) Distribution of grove-level historical-minimum *P–ET*. For each grove, the probability-density function of *Min. P–ET* at all 30-m pixels is plotted and colored by its mean value. On the y-axis, groves are sorted by elevation from highest to lowest. b) linear-regression trend line of mean *Min. P–ET* in groves. The statistically insignificant p-value of 0.058 is for the positive regression slope from a two-sided Wald test.

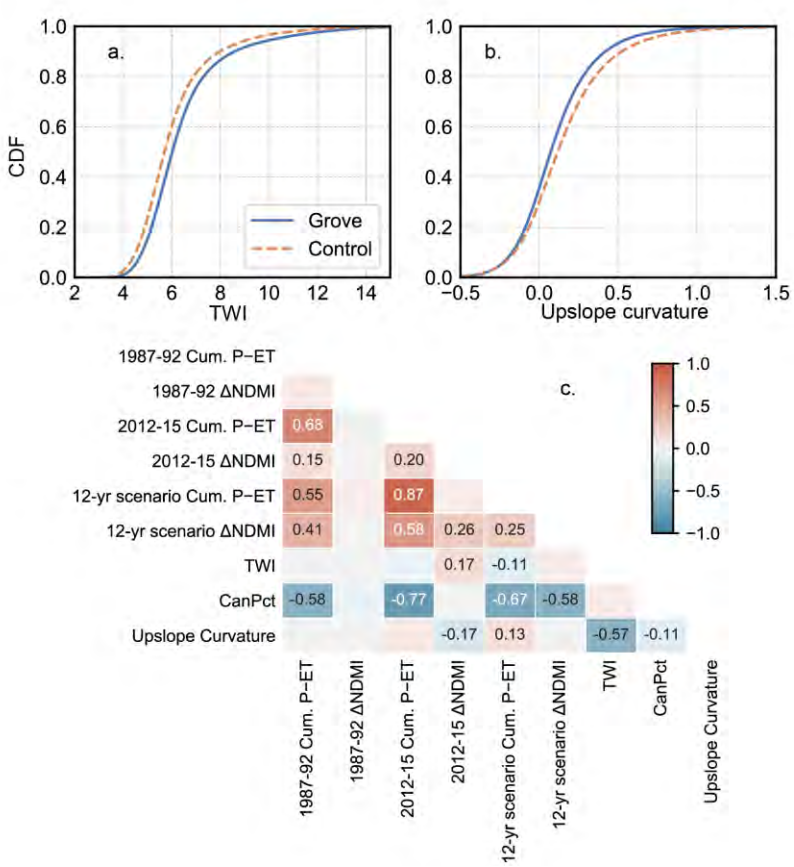

Figure S23. Comparison of cumulative distribution function (CDF) of a) Topographic Wetness Index (TWI) and b) upslope curvature between giant-sequoia groves and non-grove control areas. Upslope curvature at 30-m resolution is calculated using the open-source software SAGA-GIS, the approach used in Rinderer et al. (2014). Panel c shows the matrix of Pearson correlations between cumulative *P–ET* and moisture loss (Δ*NDMI*) during two historical droughts and TWI, Tree canopy cover percentage, and upslope curvature. Correlation (r) is calculated using all 30-m pixel data inside groves, and is labeled only for |r| > 0.1.

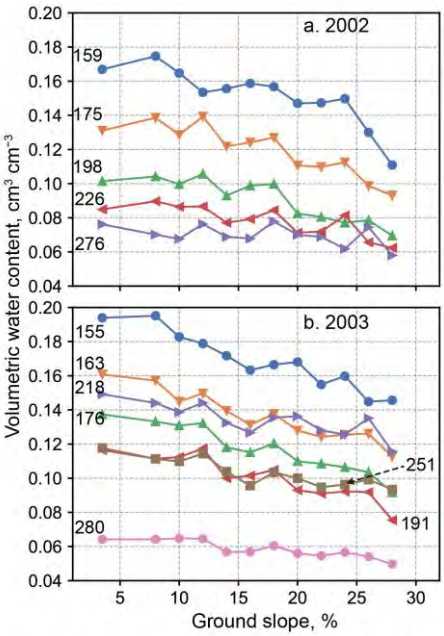

Figure S24. Declined volumetric water content at 0–15 cm layer with a steeper slope in a) 2002 and b) 2003, using survey data across 400 points in the Teakettle Experimental Forest of the Kings River basin. Details of study site and data are referred to North et al. (2005). Survey dates are labeled by the day of year (DOY).

References

Goulden, M.L., Bales, R.C., 2019. California forest die-off linked to multi-year deep soil drying in 2012–2015 drought. Nat. Geosci. 12, 632–637. https://doi.org/10.1038/s41561-019-0388-5

Lundberg, S., Lee, S.-I., 2017. A Unified Approach to Interpreting Model Predictions. Adv. Neural Inf. Process. Syst. 4766–4775.

Lundberg, S.M., Erion, G.G., Lee, S.-I., 2018. Consistent Individualized Feature Attribution for Tree Ensembles. arXiv preprint arXiv:1802.03888.

North, M., Oakley, B., Fiegener, R., Gray, A., Barbour, M., 2005. Influence of light and soil moisture on Sierran mixed-conifer understory communities. Plant Ecol. 177, 13–24. https://doi.org/10.1007/s11258-005-2270-3

Rinderer, M., van Meerveld, H.J., Seibert, J., 2014. Topographic controls on shallow groundwater levels in a steep, prealpine catchment: When are the TWI assumptions valid? Water Resour. Res. 50, 6067–6080. https://doi.org/10.1002/2013WR015009

Shrikumar, A., Greenside, P., Kundaje, A., 2017. Learning important features through propagating activation differences. 34th Int. Conf. Mach. Learn. ICML 2017 7, 4844–4866.

Su, Y., Bales, R.C., Ma, Q., Nydick, K., Ray, R.L., Li, W., Guo, Q., 2017. Emerging stress and relative resiliency of giant sequoia groves experiencing multiyear dry periods in a warming climate. J. Geophys. Res. Biogeosciences 122, 3063–3075. https://doi.org/10.1002/2017JG004005